Structural chemistry at solid-liquid interfaces investigated by atomic force microscopy

Hiasa, Takumi

(Degree)
博士（理学）

(Date of Degree)
2012-09-25

(Date of Publication)
2013-03-26

(Resource Type)
doctoral thesis

(Report Number)
甲5642

(URL)
https://hdl.handle.net/20.500.14094/D1005642

Doctoral Dissertation

Structural chemistry at solid-liquid interfaces investigated by atomic force microscopy

（原子間力顕微鏡による固液界面の構造化学に関する研究）

July, 2012

Graduate School of Science, Kobe University

Takumi Hiasa

Contents

Chapter 1: General Introduction

1.1. Background

Liquid molecules facing solid substrates play an important role in a broad range of chemistry, biology and material sciences.[1] They are thought to determine numerous phenomena such as wetting properties, solubility, chemical reactivity or stability.[2-7] It is thus reasonable that the study of interfacial liquids has received great interest and numerous studies have been devoted to it.

Such interfacial liquids usually exhibit different properties from the bulk ones. The presence of boundary breaks the translational invariance of a bulk and introduces an anisotropy. Consequently, the properties of interfacial liquids become local. The liquid molecules facing to solid are ordering to form a certain structure different from that of a bulk. Even in the liquid state, the molecules are restricted in their motions and in the way they take a position of themselves with respect to one another. Because of the limitation of space available for molecular translation, the nearest neighbors and often second or third nearest neighbors of a liquid molecule tend to group around it not in a random way. This short-range order extends over a few molecular diameters and characterizes the liquid state. In a bulk, due to the translational invariance, there remains no correlation with respect to the reference molecule as a whole. However at the interface, this short-range order remains due to the presence of boundary breaks, which takes solid-like state. The liquid density profile is typically oscillating with the period of molecular diameter, and approaches to the density of the bulk liquid at large distances from the reference.

The magnitude and range of molecular ordering in interfacial liquids are depending on the size of the molecules and on the nature of liquid-liquid, solid-liquid interactions. Thus the liquid ordering depends on chemical and physical properties of solid surface, for example, whether they are amorphous or crystalline, atomically smooth or rough, hydrophilic or hydrophobic, homogeneous or heterogeneous. Those properties can often drastically change the macroscopic properties, such as wettability and chemical reactivity. Such changes of macroscopic properties are believed to be associated with

drastic changes of interfacial liquid structure. Specific intermolecular interaction between chemical functional groups on solid and liquid molecules, becomes a key in structuring interfacial liquids. How the intermolecular interaction affects the structuring interfacial liquids is an important issue at researches in wide range of chemistry and its related area.

Experimental studies of the behavior of interfacial liquids require obtaining information about the density distribution near surfaces. However it is very difficult to measure the liquid density profile because the target interface is buried under bulk liquids. As a rule, only rough estimation has still been done in wide area of the research. On the other hand, surface or interface sensitive techniques have been applied to investigate the interfacial liquids. Spectroscopic methods have been most widely used in this area, including core level spectroscopy such as X-ray absorption fine structure (XAFS) [8], and vibrational spectroscopy such as infrared reflection absorption spectroscopy (IRRAS) [9,10], surface enhanced Raman spectroscopy (SERS) [11-13], and sum frequency generation (SFG) [14-16]. These spectroscopic methods have provided numerous information about multilayer of the interfacial liquids. However these provided only averaged information over the interfacial layers. Recent developments of nanotechnology and molecular or supramolecular science require to determine the local structure of interfacial liquids, for example, the way of solvation on a particular site of surface such as reaction center of a catalyst, binding site of a enzyme, or clathrate water sites in a native protein.

Studies using scanning probe techniques have been challenging to molecular scale study on local structure of interfacial liquids. In early studies of scanning probes, structured liquids are modeled as adsorption of single liquid molecule onto well-defined surfaces such as single crystal of metal or metal oxides. These studies were dealing with the structure of the first layer of modeled molecules because it was thought that the interfacial structure probably determined by liquid-solid interactions, and most of interfacial properties also determined by such interactions. However, there are second, third and subsequent layers at an actual solid-liquid interface. Such overlaid layers should also determine and modify the structure or property of the first layer. Strong influence can be generated, for example, when the liquid-liquid interaction is stronger than or comparable to the liquid-solid interaction. *In-situ* analytical methods are strongly desired to determine the local structure of interfacial liquids.

Crystallographic techniques such as X-ray crystal truncation rod (CTR) scattering [17] or neutron reflectivity measurement [18] are powerful methods for such *in-situ* investigation. These methods are not destructive and can access to the buried interfaces. Using high-energy, short wavelength rays can achieve a resolution of a fraction of a nanometer, so that information is gained at the molecular level. X-ray CTR is now being used for interface studies of minerals. Newtron reflection is for studies of interfacial chemistry on soft matters such as surfactant, polymers, lipids, and adsorbates at the interface. Although the facility of high-energy beam is increasing, the use of these techniques is not yet very common because the availability of beam time is restricted by high cost.

Direct force measuring techniques can also access to the structure of interfacial liquids. Surface force apparatus (SFA) is one of the conventional methods, where two flat surfaces are carefully approached toward and retracted from one another with a precision less than 1 nm. [1] Oscillatory forces arising from the packing of individual layers of liquid molecules have been successfully measured using the SFA technique. Though the vertical layer determined with subnanometer resolution, lateral resolution of the structured liquids is quite low because macroscopic walls are used as a probe.

Atomic force microscopy (AFM) can be a simple force measurement potential to measure *in-situ* local distribution of interfacial liquids in both lateral and vertical dimension. Early studies to show the ability of AFM in measuring the force toward structured liquids demonstrated in water on $CaCO_3$ [19] and in organic solvents on HOPG. [20] Such a force modulation was observed comparable to the size of a liquid molecule. Later, AFM has been applied as an effective tool for investigating the vertical structure of interfacial liquids over the years. [21-24] The force applied to the nano-sized AFM tip is determined as a function of tip-surface distance. The force would monotonously decay with increasing tip-surface distance, if the liquid density distribution were even as in the bulk. Force strength is modulated when the liquid density is uneven because of layered distribution of interfacial liquids. Recent developments [25] of force sensing system for frequency modulation AFM (FM-AFM) enable us to trace the topography of a solid object and the local structure of the liquid facing the solid, at the same time. The force applied to the tip is determined as a function of the tip-surface distance in a precision better than 10 pN [26]. Such a sensitive detection system for weak force enables to measure the laterally local

distribution of the force with subnanometer scale. In this study, the author applied the state-of-art FM-AFM to investigate the structure of solid-liquid interfaces with molecular scale, as well as experimentally demonstrated the ability of FM-AFM to investigate the interfaces.

1.2. Aims of this study

The purpose of this study is on the molecular scale investigation and understanding of the structuring of liquids at solid-liquid interfaces. The highly sensitive AFM [25] as mentioned in the former section can be a powerful tool to achieve this purpose. The author started this study to understand the mechanism of AFM measurement by extracting the interfacial liquid structure. Employing such ability of the highly sensitive FM-AFM, the interfacial liquid structures were observed over well-defined, functionalized surfaces. The observations lead to discuss the factors determining the interfacial structure, focusing on molecular structure and chemical functional groups of solids and liquids. In addition to these fundamental investigations, the possibilities and abilities of FM-AFM applications to the molecular scale investigation of the interfacial structure were demonstrated at practical solid-liquid interfaces.

Mechanism of AFM measurement detecting liquid structure

The direct measurement of interfacial liquids using the highly sensitive AFM mentioned in the former section is quite new approach to study the interface. Therefore many disputable questions still remains to determine the local structure of interfacial liquids from force measurement. In this study, the author focused on the following two problems.

1. Understanding the force distribution

Using SFA, many researchers have investigated how liquid structure forms and affects the forces between macroscopic surfaces at distances below a few nanometers. The force applied to macroscopic force probes is related to density distribution of the

confined liquids. On the other hand, in AFM experiment, extremely sharp tip apex has a potential to measure the distribution at open, intrinsic interface. The measurement using AFM has found an oscillatory force profile at the interface, and in recent studies, [27,28] the force profile was found to be dependent on the surface sites. However such local force distribution has not been fully understood yet, especially its relation with the molecular scale local structure of interfacial liquids. The author measured the force distributions at the interfaces of aqueous solution and metal oxides, and analyzed them by comparing with the density distributions obtained by X-ray diffraction or molecular dynamics simulation.

2. Role of tip apex

In AFM experiments, uncertainties about local tip geometry of the interaction area with an object, often lead to a problem in interpreting measured force profiles. Approximation of the tip apex was demonstrated theoretically [29-31], and experimentally in a vacuum [32-34] which suggested that such a small tip apex acts as the force probe, and enables molecular scale spatial resolution. In this case, only single or a few atoms tip apex attributes to load the force from a single atomic site of surface, resulted in pN-order weak forces. However experimental knowledge of the tip apex is quite limited at liquid-solid interfaces. In this study, two commercially available silicon cantilevers with sharpened or cone-shaped tips was used to compare the topography and force-distance curves. The presence and role of atomistic minitip on the tip bodies are discussed. In addition, the contribution of atomic scale tip apex to the force contrast is discussed in observing chemically heterogeneous surfaces.

The experimental verification and discussion of these issues is described in Chapter 3. A promising ability of FM-AFM was convinced through these experimental approaches for understanding the mechanism to measure the local structure of interfacial liquids.

Factors contributing to interfacial liquid structure

Another issue of this study is to discuss the mechanism of structuring interfacial liquids. Molecular scale analysis of interfacial liquid structures gives a new physical

insight to the structuring mechanism because experimental methods for direct observation of such a fine structure have been quite limited. As mentioned in section 1.1, molecular geometry and intermolecular interactions are thought to affect the structuring interfacial liquids, which is an important issue in researches of related area. The description and prediction of the interfacial liquids is noticeably complicated because many factors attribute to their structure. Therefore, the structure and chemical composition of surface needs to be controlled in subnanometer scale, to isolate the contributions.

In this study, self-assembled monolayer (SAM) was applied as a well-designed surface to verify the contribution of the surface functional group to structuring the interfacial liquid. SAM provides a flexible, atomically flat surface where the surface functional groups can be easily modified by alternating assembled molecules. [35] Though such a self-assembly method has been widely used, it is essential to optimize the preparation procedure of SAM for liquid AFM imaging because atomistic flatness, extreme cleanness, and chemical stability of surface is particularly required for achieving subnanometer resolution. Finding an appropriate condition of preparing SAM substrate is thus important. Indeed, only a few examples have been demonstrated to achieve subnanometer resolution in liquids such as mica and a kind of protein membrane at the beginning of this study. Establishing appropriate preparation procedure will lead the AFM measurement to a versatile method.

Using such a well-defined substrate, the interfacial structures of various liquids facing different surface functional groups were determined. These direct measurements of the interfacial structures provide fundamental insights in interfacial chemistry and molecular science, such as structural relation of interfacial liquids and surface with a molecular scale. Also, the author discusses the dominant factor for structuring at the interface from comparison of the interfacial structures. In this study, the author especially focuses on the following two factors.

One is molecular structure of liquids. The effect from geometric configuration of liquid molecules themselves is discussed for structuring at the solid interface. In order to isolate such steric contribution to the structuring of interfacial liquids, the interfacial structures of liquid hydrocarbons facing a CH_3-terminated SAM were investigated, where was no specific chemical interaction, and just with van der Waals interactions. This is a model inert interface where steric configuration of liquid molecules expected

to dominantly affect the interfacial structure. The discussion is described in Chapter 4.

The other is specific chemical interaction, such as hydrogen bonds. In order to discuss such a contribution of chemical interaction, local structure of interfacial liquids were compared by modifying of functional groups on surfaces and liquid molecules; in this study, the structure of water and polar organic liquids were determined over various hydrophilic surfaces. Besides, steric environment of reactive functional group of liquid molecules also affect the specific chemical interaction. To assess the steric contribution, the author compared the interfacial structure of primary, secondary, and tertiary, short-chain and long-chain alcohols. The discussion of the factor for structuring interfacial polar liquids is described in Chapter 5.

As well as providing fundamental insights in structural chemistry at the interface, a sequence of the measurements becomes experimental evidence that tip-probed force distribution is a consequence of the local structure of interfacial liquids, much less contribution of tip-induced effects. These should help establishing the AFM measurement to observe *in-situ* liquid structure.

Interfacial liquid structure in practical systems

The structure of interfacial liquids is thought to determine their wetting properties and underlies various phenomena. In addition to the fundamental studies as mentioned above, the author hopes that the analysis of interfacial liquid structure correlates with understanding the mechanism of practical phenomena or improvement of industrial processes. In this study, the author gives two examples of a practically important interface to suggest the utility and potentiality of the AFM analysis.

One example is wettability on metal oxide surfaces, such as mica, Al_2O_3, TiO_2, on which different wetting properties are exhibited for water. Cross-sectional structures of interfacial water of the three oxide surfaces are compared to discuss the relationship between microscopic interfacial structure and macroscopic wetting properties on the surface. These observations and discussion are described in Chapter 6.

The other example is synthetic polymers. Most polymers contain crystallized and amorphous domains to be heterogeneous. Crystallized domains, lamellae, are embedded in amorphous portions and the size of lamellae is typically less than 50 nm [36]. Interface with organic solvents is important in industrial applications and manufacturing

processes. The stability and chemical resistibility in solvent cast or extrusion manufacture, for example, should be related to the shape of domains and domain boundaries, as well as intra-domain structures. Physical and chemical properties of polymer products are also sensitive to the surroundings. It is thus demanded to observe the topography of synthetic polymers immersed in organic liquids in subnanometer resolution. High-resolution imaging using FM-AFM is suitable and can provide helpful information for the practical usage. These observations and discussion are described in Chapter 7.

References in Chapter 1

[1] J. N. Israelachvili, *Intermolecular and Surface Forces 3rd Ed.*, Academic Press, London, 2010.

[2] M. A. Henderson, *Surf. Sci. Rep.* 46 (2002) 1.

[3] A. Verdaguer, G. M. Sacha, H. Bluhm and M. Salmeron, *Chem. Rev.* 106 (2006) 1478.

[4] G. A. Somorjai, H. Frei and J. Y. Park, *J. Am. Chem. Soc.* 131 (2009) 16589.

[5] M. Chaplin, *Nat. Rev. Mol. Cell Biol.* 7 (2006) 861.

[6] Y. Levy and J. N. Onuchic, *Annu. Rev. Biophys. Biomol. Struct.* 35 (2006) 389.

[7] C. D. Taylor, M. Neurock, *Curr. Opin. Solid State Mater. Sci.* 9 (2005) 49.

[8] D. E. Ramaker and D. C. Koningsberger, *Phys. Chem. Chem. Phys.* 12 (2010) 5514.

[9] K. Ashley and S. Pons, *Chem. Rev.* 88 (1988) 673.

[10] T. Iwasita and F. C Nart, *Prog. Surf. Sci.* 55 (1997) 271.

[11] S. Zou and M. J. Weaver, *Anal. Chem.* 70 (1998) 2387.

[12] M. J. Weaver, S. Zou and H. Y. H. Chan, *Anal. Chem.* 72 (2000) 38 A.

[13] Z.-Q. Tian, B. Ren, and D.-Y. Wu, *J. Phys. Chem. B* 106 (2002) 9463.

[14] Q. Du, R. Superfine, E. Freysz, and Y. R. Shen, *Phys. Rev. Lett.* 70 (1993) 2313.

[15] C. D. Bain, *J. Chem. Soc., Faraday Trans.* 91 (1995) 1281.

[16] A. J. Hopkins, C. L. McFearin, and G. L. Richmond, *Curr. Opin. Solid State Mater. Sci.* 9 (2005) 19.

[17] P. Fenter and N. C. Sturchio, *Prog. Surf. Sci.* 77 (2004) 171.

[18] G. F.-Cusani, *J. Phys. Condens. Matt.* 13 (2001) 4973.

[19] J. P. Cleveland, T. E. Schäffer, and P. K. Hansma, *Phys. Rev. B* 52 (1995) 8692.

[20] S. J. O'Shea, M. E. Welland, and T. Rayment, *Appl. Phys. Lett.* 60 (1992) 2356.

[21] H.-J. Butt, B. Cappella, and M. Kappl, *Surf. Sci. Rept.* 59 (2005) 1.

[22] T. Fukuma, *Jpn. J. Appl. Phys.* 48 (2009) 08JA01.

[23] S. J. O'Shea, N. N. Gosvami, L. T. W. Lim, and W. Hofbauer, *Jpn. J. Appl. Phys.* 49 (2010) 08LA01.

[24] R. Hayes, G. G. Warr, and R. Atkin, *Phys. Chem. Chem. Phys.* 12 (2010) 1709.

[25] T. Fukuma, M. Kimura, K. Kobayashi, K. Matsushige and H. Yamada, *Rev. Sci. Instrum.* 76 (2005) 053704.

[26] T. Fukuma, K. Onishi, N. Kobayashi, A. Matsuki and H. Asakawa, *Nanotechnology* 23 (2012) 135706.

[27] K. Kimura, S. Ido, N. Oyabu, K. Kobayashi, Y. Hirata, T. Imai, and H. Yamada, *J. Chem. Phys.* 132 (2010) 194705.

[28] T. Fukuma, Y. Ueda, S. Yoshioka, and H. Asakawa, *Phys. Rev. Lett.* 104 (2010) 016101.

[29] K. Tagami and M. Tsukada, *Jpn. J. Appl. Phys.* 39 (2000) 6025.

[30] M. Harada and M. Tsukada, *Phys. Rev. B* 82 (2010) 035414.

[31] M. Watkins, M. L. Berkowitz and A. L. Shluger, *Phys. Chem. Chem. Phys.* 13 (2011) 12584.

[32] F. J. Giessibl, *Science* 267 (1995) 68.

[33] R. Pérez, I. Štich, M. C. Payne, and K. Terakura, *Phys. Rev. B* 58 (1998) 10835.

[34] S. Morita and Y. Sugawara, *Appl. Surf. Sci.* 140 (1999) 406.

[35] L. H. Dubois and R. G. Nuzzo, *Annu. Rev. Phys. Chem.* 43 (1992) 437.

[36] H. Schönherr and G. J. Vancso, *Scanning Force Microscopy of Polymers*, Springer, 2010.

Chapter 2: Principle and Instrument of Frequency Modulation Atomic Force Microscopy

2.1 Historical review on atomic force microscopy

Atomic force microscopy (AFM) is one of the high-resolution type of scanning probe microscopy, with demonstrated resolution better than the order of nanometer. AFM has invented by G. Binnig and coworkers in 1986 [1], and lattice image of graphite surface was successfully obtained [2]. After that, AFM has developed as a powerful tool to investigate the surface with an atomistic resolution, even in an ambient condition. AFM consists of a cantilever with a sharp tip (probe) at its end that is used to scan the surface. The cantilever is typically silicon or silicon nitride with a tip of radius on the order of nanometers as presented in Fig. 2.1. When the tip penetrates into proximity of a sample surface, forces between the tip and the surface lead to a deflection of the cantilever. Depending on the situation, forces that are measured in AFM include mechanical contact force, van der Waals forces, capillary forces, chemical bonding, electrostatic forces, magnetic forces, Casimir forces, solvation forces, etc.

One of the remarkable features in AFM is that it does not require any special environment. In addition, there is no special requirement for imaging object, such as conductive coatings in electron microscopy imaging. Because of these advantages over other atomically resolving imaging techniques, AFM applications to atomic scale *in vivo* imaging are greatly expected for chemical and biological fields.

A simple contact AFM measurement has been applied in various fields, and many outstanding results have been successfully obtained with atomic and molecular levels. Numerous kinds of materials have been investigated such metals, semiconductors, polymers, proteins and tissues.

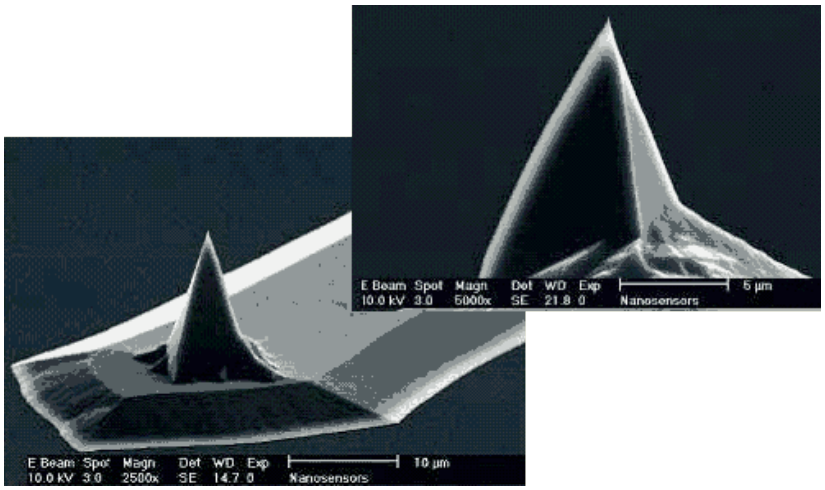

Figure 2.1. Scanning electron microscopy images of typical silicon nitride cantilever for AFM use (Nanosensor, NCH). The image is reprinted from a catalog (Nanosensor).

However, Pethica and Oliver pointed out that contact AFM could not observe atomic defects such as atom vacancies and also that the normal loading force for typical contact AFM measurement considerably exceeded the load limit of a single atom. [3] Contact area of the AFM tip should be larger than the size of a single atom as shown in Fig. 2.2(a), implying that contact AFM does not provide true atomic resolution. In 1992, Giessibl and Binnig [4] showed that a KBr surface was destroyed by tip scanning, but they succeeded in taking a step line image with atomic resolution in ultra high vacuum (UHV), at 4 K using contact AFM with -1 nN (attractive) of loading force. Furthermore Ohnesoge and Binnig succeeded in true atomic resolution image resolved atomic scale kinks and defects with its feedback regulated in attractive regime of tip-surface force. [5]

More clear and reliable true atomic resolution image has been required owing to development of non-contact AFM. Frequency modulation (FM) method [6] is one of the effective force detection methods, and is widely used today. In FM operation, the resonance oscillation of the cantilever is mechanically excited. The resonance frequency shift due to the applied force to the tip from the surface, is detected. Therefore weak force can be detected for small loading area of the tip apex (Fig. 2.2(b)). Using such

frequency modulation AFM (FM-AFM), atomically resolved image of Si(111)(7×7) was successfully obtained in UHV at room temperature by Giessibl [7] or Kitamura and Iwatsuki [8]. In addition, Ueyama et al. successfully obtained the atomic resolution image of atom vacancy on an InP(110) cleaved surface [9], and then Sugawara et al. revealed defect motion of the atomic vacancies on InP(110). [10]

Since FM-AFM can precisely measure the applied force to the tip with an atomic scale, three-dimensional force distribution can be further obtained with an atomic resolution. There are two ways to obtain such a three-dimensional force distribution. One is to obtain the site-specific frequency-shift distance curves at different specific lateral sites. The other is to obtain the lateral constant height frequency-shift images at different tip-surface distances. Thermal drift often disturbs relative position a tip and surface during a scan, which causes to distort the distribution. The three dimensional force distribution was successfully obtained on the Si(111)(7×7) surface using feedforward compensation for thermal drift. [11]

Recently the use of the small amplitude and large noise reduction in cantilever deflection sensor brought great progress in FM-AFM imaging in liquids [12,13]. Owing to the highly sensitive force detection system, true atomic-scale topography was firstly observed on mica also in an aqueous solution [12,14].

The precise force detection can be applied to the three- (or two-)dimensional force distribution measurement by FM-AFM. Two research group, Kimura et al. [15] and Fukuma et al. [16] recently found that frequency shift distribution measured in water reflects local structure of interfacial water. Oscillatory modulations were found in the vertical frequency shift-distance curve that should be reflected the oscillatory water density distribution due to the hydration to the surface.

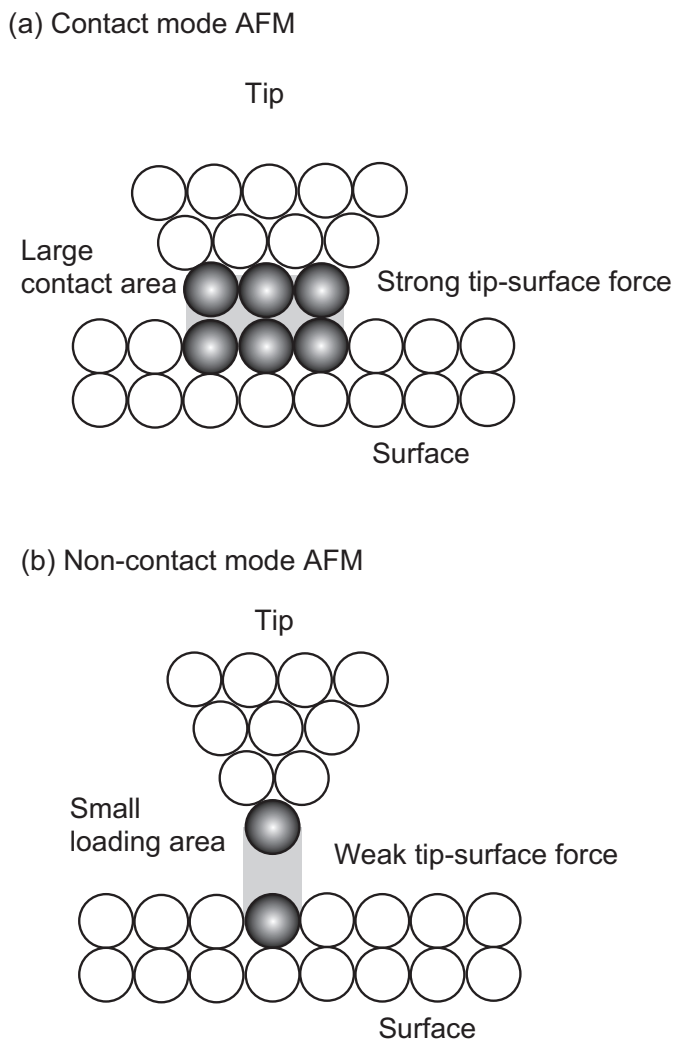

Figure 2.2. Schematic models of (a) contact-mode AFM and (b) non-contact mode AFM. Illustration (a) shows that contact-mode AFM has a large contact area. As a result, strong repulsive force is applied to the tip in contact-mode AFM. On the other hand, illustration (b) shows non-contact-mode AFM has a small area where the tip loads the force. As a result, weak attractive force can be detected via a modulation (typically frequency shift) in the mechanical oscillation of the cantilever.

2.2 Basic principle of atomic force microscopy

2.2.1 Imaging signal in AFM

In operating AFM, forces between the tip and the object are detected. When a tip close to a surface as schematically illustrated in Fig. 2.2, the potential energy from the surface (U) is applied to the tip and causes a z component of the tip-surface force (F_z) as (2.1).

$$F_z = -\frac{\partial U}{\partial z} \quad (2.1)$$

Depending on the mode of operation, AFM uses F_z as the imaging signal.

Vertical force (F_z) usually has a very strong distance dependence, varied from long- and short-range contributions. Here the contributions are classified by their range and strength. Van der Waals, electrostatic, and magnetic forces are typically with a long range and chemical forces with a short range (fractions of nm).

The van der Waals interaction is caused by fluctuations in the electric dipole moment of atoms and their mutual polarization. For a spherical tip with radius R to a flat surface, the van der Waals potential is given by [17]

$$U_{vdw} = -\frac{A_H R}{6z} \quad (2.2)$$

Here z defines the distance between the plane connecting the centers of the surface atoms and the center of the closest tip atom, and A_H is Hamaker constant. The Hamaker constant depends on atomic polarizability and density of the tip and surface atom. For most solids A_H is the order of 1 eV in vacuum. Suppose a spherical metal tip whose radius is 100 nm, van der Waals force can cause a large attractive interaction, and it can be estimated as the order of 10 nN at 0.5 nm above from the surface.

When both the tip and the surface are conductive, electrostatic force is also applied to the tip. For a spherical tip with radius R, electrostatic force is given by [17]

$$F_e = -\frac{\pi\varepsilon R(\Delta U_e)^2}{z} \quad (2.3)$$

Here ΔU_e is the difference of the electrostatic potential between the tip and surface, and ε is electric permittivity. Like a van der Waals interaction, the electrostatic force can cause a large attractive interaction, and it can be estimated the order of 10 nN when

estimated as R = 100 nm, and ΔU_e = 1V in vacuum.

Chemical interaction force is often described by a model potential [17] such as the Morse potential,

$$U_{Morse} = -E_{Bond}\left[2e^{-\kappa(z-\sigma)} - e^{-2\kappa(z-\sigma)}\right] \quad (2.4)$$

or the Lennard-Jones potential

$$U_{L-J} = -E_{Bond}\left(2\frac{z^6}{\sigma^6} - \frac{z^{12}}{\sigma^{12}}\right) \quad (2.5).$$

As seen in their formula, these potentials have strong dependence of the distance, acting at a short distance from surface. The short-range chemical interaction is especially important for observing atomic scale structure of the surface, as pointed out in many reports [18-26].

2.2.2 Measurement of cantilever deflection

In AFM, forces applied to the tip are detected through a deflection of the cantilever. The cantilever is characterized by its spring constant k, eigenfrequency f_0 and quality factor of oscillation Q. For rectangular cantilever as shown in Fig. 2.3, the spring constant k is given by [27],

$$k = \frac{E_y w t^3}{4L^3} \quad (2.6)$$

and the eigenfrequency is given by

$$f_0 = 0.162\frac{t}{L^2}\sqrt{\frac{E_y}{\rho}} \quad (2.7).$$

Here E_y is Young's modulus and ρ is the mass density of the cantilever's material. The Q-factor depends on the damping of the cantilever. Typical Q value is 10000 in vacuum, 100 in air and 10 in liquid for a typical micro-sized cantilever.

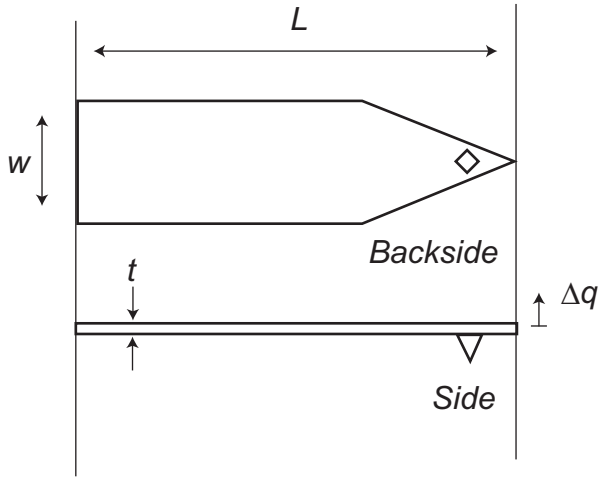

Figure 2.3. Schematic illustration of micrometer-scale cantilever.

Using these cantilever mechanical factors, the applied forces are calculated from the deflection changes when acting the force. Cantilever deflection is typically measured as following ways. One is using a laser spot reflected from the top surface of the cantilever into an array of photodiodes. Other methods are using optical interferometer, capacitive sensing or piezoresistive AFM cantilevers. The former optical lever method is applied in this study, and briefly reviewed here. One of the major configurations of optical lever detection system of cantilever deflection is shown in Fig. 2.4. Laser light from a laser diode (LD) is reflected off the back of the cantilever and collected by a position sensitive detector which consists of four individual photodiodes closely spaced each other. Angular displacement of the cantilever results in one photodiode collecting more light than the other photodiodes. A differential amplifier outputs the vertical and horizontal difference between the photodiode signals normalized by their sum, which is proportional to the deflection of the cantilever.

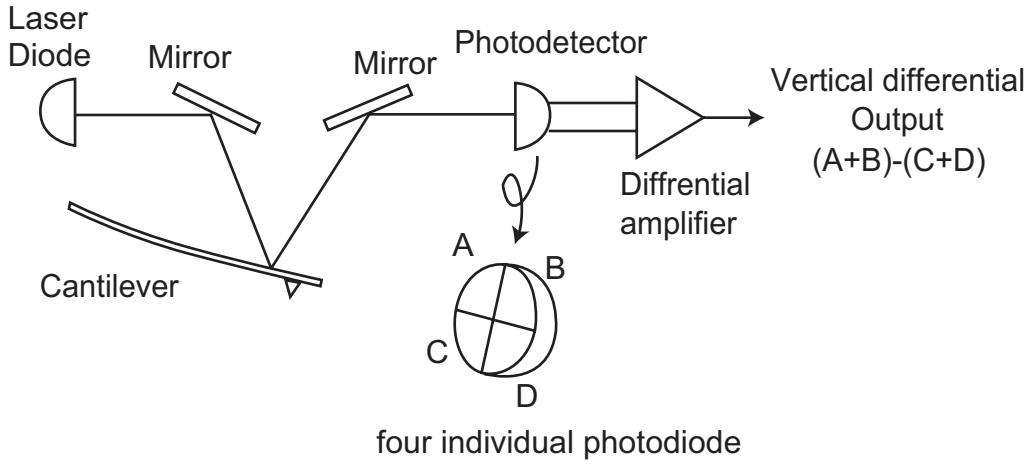

Figure 2.4. Schematic illustration of optical lever method for the detection of the cantilever deflection.

2.2.3 Operation modes

AFM can be operated in a number of scan modes, depending on its application. In general, possible imaging modes are divided into contact modes and a variety of dynamic modes where the cantilever is vibrated.

In the contact mode operation, the static tip deflection is used as a feedback signal. The force between the tip and the surface is kept constant during scanning by maintaining a constant deflection. The deflection Δq directly translates into the applied force with

$$F = k\Delta q \quad (2.8).$$

Low stiffness cantilevers are generally used to boost the deflection signal, because a static deflection signal is susceptible to noise and thermal drift. Since intra-atomic force constant in solids is typically in a range of 10-100 nN/m, the cantilever spring constant should be much softer than these values. Even though it has been demonstrated that an atomic resolution could achieved with contact-mode AFM, it causes detrimental effect for precise measurement that static deflection signal is susceptible to noise and thermal drift.

On the other hand, in the dynamic mode, the cantilever is externally oscillated at close to its fundamental resonance frequency or a harmonic. There are two basic methods to detect the applied forces to the tip. One is from the modulations of oscillation amplitude, the other is from the shift of resonance frequency.

In amplitude modulation AFM (AM-AFM), changes in the phase of oscillation can be used to discriminate between different types of materials on the surface. Amplitude modulation can be operated either in the non-contact or in the intermittent contact regime. In dynamic mode, the cantilever is oscillated such that the separation distance between the cantilever tip and the sample surface is modulated. Amplitude modulation has also been used in the non-contact regime to image with atomic resolution by using very stiff cantilevers and small amplitudes. Such an operation of AM-AFM with intermittent contact with the surface in repulsive force regime is often called "tapping mode."

On the other hand, in using the shift of the frequency or phase, the tip can constantly operate not to contact with the surface (non-contact mode.) The cantilever is instead oscillated at its resonant frequency where the amplitude of oscillation is typically less than a few nanometers for achieving atomic resolution. When force is applied to the tip at the free end of the cantilever, the resonance frequency shifts accordingly. Such shifts of resonance frequency in maintaining a constant oscillation amplitude of the cantilever, relates to the conservative component of the force is extracted in such frequency modulation (FM) detection.

Frequency modulation AFM (FM-AFM) does not suffer from tip or sample degradation effects that are sometimes observed after taking numerous scans with contact AFM. This is a grate advantage of non-contact AFM for contact AFM in measuring soft and elastic samples. Frequency can be measured with very high sensitivity and thus the frequency modulation mode allows over the use of very stiff cantilevers. Stiff cantilevers provide stability very close to the surface and, as a result, FM-AFM can provide true atomic resolution as mentioned in section 2.1. Also, when a few monolayers of adsorbed liquid are lying on the surface of a rigid sample, the images would look quite different. A non-contact mode operation where the tip penetrates into the liquid layer to image the underlying surface can image both the liquid and surface. In this study, this type of AFM has been applied to investigate a structure of solid-liquid interface.

2.3 Principle of frequency modulation AFM

2.3.1 Basic principle and experimental setups

Cantilever excitation

A cantilever is mechanically oscillated by an adjacent ceramic actuator. The excitation voltage induces piezoelectric vibration of the actuator, and the cantilever (and the attached tip) is vibrated in turn. Assumed the excitation voltage as $V_{exc}\cos(\omega t)$, the motion of the tip is described by,

$$z_t = z_{t0} + A\cos(\omega t + \phi). \quad (2.9)$$

Here, ϕ means the phase shift between the mechanical excitation at the actuator and the tip vibration.

The resultant tip motion is followed the equation of motion which is given by,

$$m\frac{d^2 z_t}{dt^2} + \gamma\frac{dz_t}{dt} + k(z_t - z_{t0}) = 0 \quad (2.10)$$

Here, m and γ represents mass and dissipation coefficient, respectively. From the equations (2.9) and (2.10), A and ϕ are described as

$$A = \frac{A_0}{\sqrt{Q^2(1 - f^2/f_0^2)^2 + f^2/f_0^2}} \quad (2.11)$$

$$\phi = \arctan[\frac{-f/f_0}{Q(1 - f^2/f_0^2)}] \quad (2.12)$$

Figure 2.5 shows the plots of A and ϕ as a function of the oscillation frequency f from these equations. The relevant parameters Q, A_0 and f_0 are defined as shown in the figure. At the resonance frequency $f = f_0$, the oscillation amplitude of the tip becomes its maximum. The phase shift ϕ becomes -90° just at the resonance.

In FM-AFM, the total phase shift through the feedback circuit ϕ_{FB}, is adjusted so as to meet ϕ_{FB} = -90°. Thus the cantilever is continuously oscillated at its resonance frequency during scans.

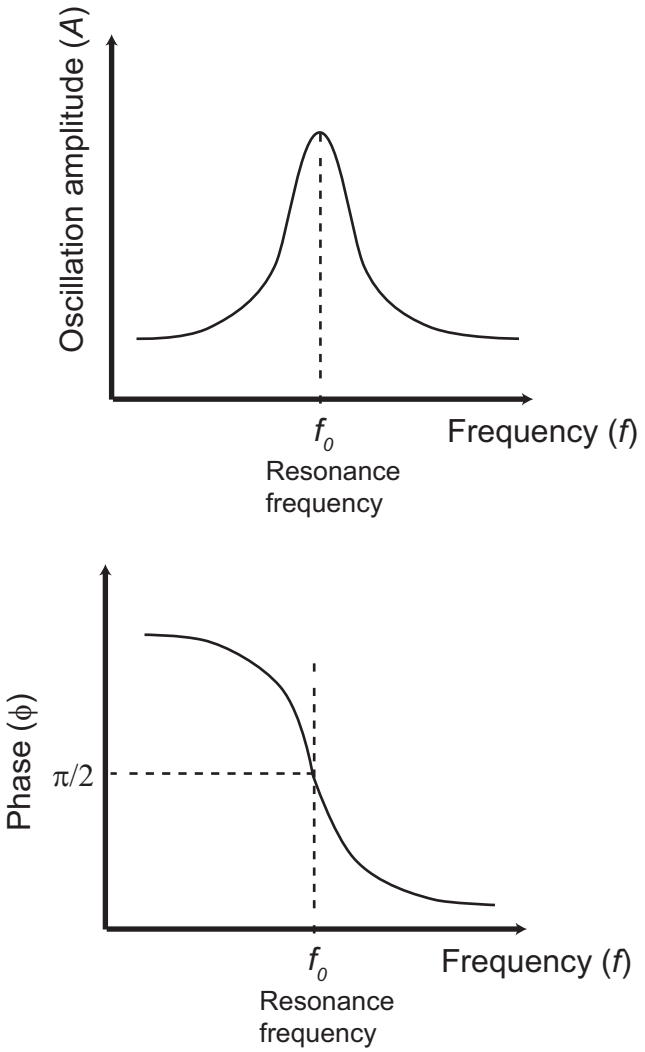

Figure 2.5. Frequency dependence of the oscillation amplitude (A) and the phase shift (ϕ) between the mechanical excitation at the actuator and the tip vibration. The plots are schematically illustrated as equations (2.11) and (2.12).

Experimental setup

Figure 2.6 shows a typical experimental setup for FM-AFM. In FM-AFM, a cantilever oscillated at eigenfrequency f_0 with controlled positive feedback in a way that it oscillates with a constant amplitude A. The deflection signal of the cantilever is phase-shifted, routed through an automatic gain control circuit, and fed back to the ceramic actuator for cantilever oscillation.

In the case of the closed feedback loops as shown in Fig. 2.6, the driving frequency is determined by eigenfrequency f_0, amplitude A, phase shift ϕ, and applied force to the tip. The purpose of the oscillator circuit is to provide controlled positive feedback with keeping the phase shift ϕ_{FB} of -90° such that the cantilever oscillates at constant amplitude.

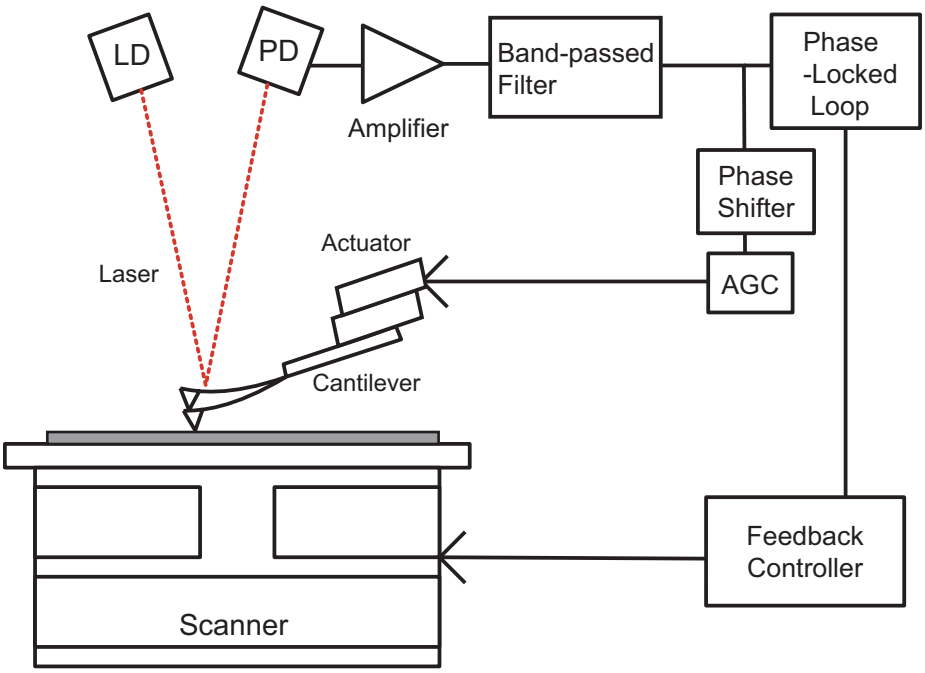

Figure 2.6. A typical experimental setup of FM-AFM.

The cantilever deflection signal is routed through a bandpass filter centered around f_0 which cuts off the noise from unwanted frequency bands. The filtered deflection signals branches into automatic gain control (AGC), a phase-shifter and frequency-shift detector. AGC is for amplitude regulation of oscillation amplitude constant to the setting target. The phase-shifter is adjusted so that the driving signal required the resonance condition (ϕ_{FB} = -90°).

The frequency shift is detected by the phase-locked loop (PLL) detector with an analog voltage controlled oscillator. Schematic block diagram of PLL is illustrated in Fig. 2.7. The PLL outputs a DC signal which is proportional to the difference between the input frequency and reference frequency (corresponding to eigenfrequency.) The phase difference between the deflection signal and voltage controlled oscillator (VCO) is detected by a phase detector. This signal is low-pass filtered and used as the input signal of the VCO whose oscillation frequency proportional to the signal. Thus, when the circuit is convergent, this filtered signal can be used as the frequency shift for imaging signal in FM-AFM.

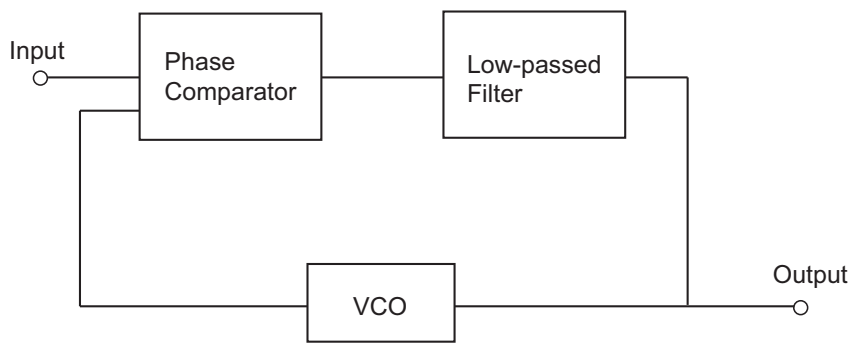

Figure 2.7. A schematic block diagram of a phase-locked loop circuit for detection of a resonance frequency shift.

2.3.2 Qualitative force calculation in FM-AFM

Frequency shift

One of advantages of FM-AFM is that the tip position can be precisely controlled using sensitive force detection of short-ranged interaction. Distance dependence of the force applied to the tip is essential for such a precise control of the tip position, which is required to achieve a true atomic resolution.

Conservative tip-sample forces cause a shift of the resonance frequency. When the phase shift is exactly -90°, the cantilever oscillates at a resonance frequency. Forces applied to the tip cause a change in $\Delta f = f - f_0$.

The unperturbed motion of the cantilever is given by:

$$\Delta q(t) = A\cos(2\pi f_0 t) \quad (2.13)$$

and the eigenfrequency is described by:

$$f_0 = \frac{1}{2\pi}\sqrt{\frac{k}{m}} \quad (2.14)$$

If the second derivative of the tip-sample potential U (or tip-sample force F)

$$k_{t-s} = \frac{\partial F}{\partial z} = \frac{\partial^2 U}{\partial z^2} \quad (2.15)$$

is constant for the whole range covered by the oscillating cantilever, the eigenfrequency that occurs is given by:

$$\Delta f = \frac{f_0}{2k} k_{t-s} = \frac{f_0}{2k}\frac{\partial F}{\partial z} \quad (2.16)$$

Namely, Δf is directly proportional to the force gradient. When such a empirical short-ranged potential as the Morse potential (2.4) or Lennard-Jones potential (2.5) applied to the tip, the applied force thus is short-ranged. However, $k_{t\text{-}s}$ varies by several orders of magnitude during one oscillation cycle in such cases and the perturbation has to be employed to the exact calculation of frequency shift.

Qualitative relationship between force and frequency shift

Observed frequency shift results from the interaction force between the tip and a surface. The force-distance curve can be obtained from the change of frequency shift with the tip-surface distance. Recently, Sader and Jarvis have developed the relationship between the frequency shift and force, which is given by [28]

$$F(z) = 2k\int_z^{\infty}\left(1+\frac{a^{1/2}}{8\sqrt{\pi(t-z)}}\right)\Omega(t) - \frac{a^{3/2}}{\sqrt{2(t-z)}}\frac{d\Omega(t)}{dt}dt \qquad (2.17)$$

where $\Omega(z) = \Delta f / f_0$ and a is oscillation amplitude. It is expected that the inverted force-distance curve is a total superposition of the various kinds of force acting on the tip. By fitting and subtracting the long-range part of the total force, the short range part, which dominates the interaction to the tip on achieving true atomic resolution, can be extracted.

2.3.3 Setup for FM-AFM measurement in liquids

In this study, a commercial AFM instrument (WET-SPM9600, Shimadzu) was customized for measurement in a liquid environment. In this subsection, the sample mounting system is introduced. Since xyz-piezos are set at the bottom in the current AFM, excess imaging liquids could damage the piezos. Thus the sample mount needs to be optimized for imaging with liquids. Figure 2.8 shows a developed custom-made sample mount compatible with imaging in water and organic solvents, and an experimental setup with an optical lever detection system for cantilever deflection. The body of the mount is a fluorocarbon polymer (polychlorotrifluoroethylene: PCTFE) disk with two circular trenches. Typically the sample substrate is securely fixed on the disk using an adhesive. The excess adhesive is injected into the inner trench and the sample is fixed to cover the trench. An imaging liquid is then placed on the sample. The liquid droplet is separated from the adhesive to avoid accidental contaminations. The cantilever and cover glass plate are finally put on the top. The glass plate is efficient to stabilize optical paths into/from the liquid droplet. Excess imaging liquid, if present, is held in the outer trench as not to contaminate the piezo scanner at the bottom of the mount.

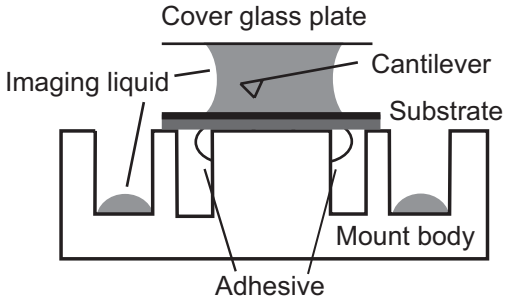

Figure 2.8. Experimental setups of AFM imaging in liquids. Samples are mounted on a manufactured fluorocarbon polymer disk.

2.4 Noises in FM-AFM

2.4.1 Noises of the cantilever deflection

Low vertical noise is prerequisite for obtaining high lateral and vertical resolution. The vertical noise in FM-AFM can be given by the ratio between the noise in the imaging signal and the slope of the imaging signal with respect to z:

$$\delta z = \frac{\delta \Delta f}{\left| \partial \Delta f / \partial z \right|} \quad (2.18)$$

The connection of $\delta \Delta f$ and δz is schematically indicated with frequency shift-distance curve as shown in Fig. 2.9.

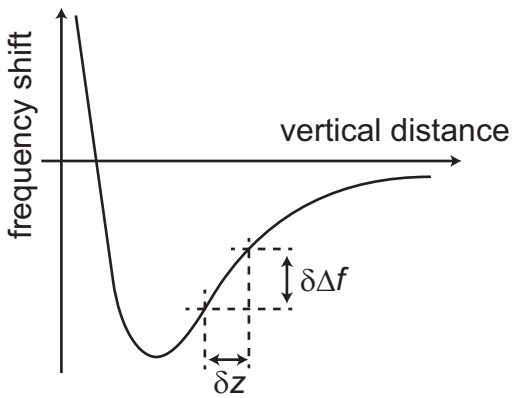

Figure 2.9. Plots of frequency shift as a function of tip-sample distance. The noise in the tip-sample distance δz is given by the noise of the frequency shift $\delta \Delta f$ divided by the slope of the frequency shift-distance curve.

Equation (2.18) shows that the accuracy of the frequency shift measurement, which is related to the measurement of the cantilever deflection, determines the vertical resolution in FM-AFM. The deflection noise $\delta \Delta z$ is schematically indicated in Fig. 2.10. The deflection noise $\delta \Delta z$ is has the two major contributions: thermal noise of the cantilever and instrumental noise in the deflection sensor. For most practical cases, the thermal limit is much lower than the actual instrumental deflection noise.

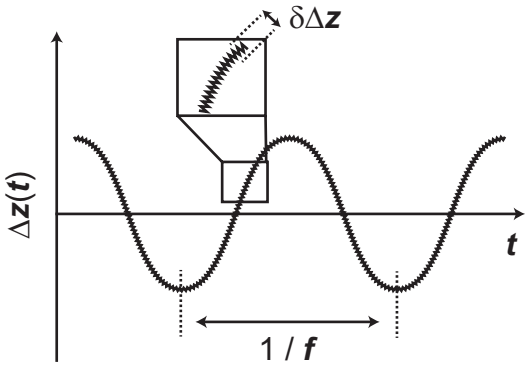

Figure 2.10. Schematic illustration of typical deflection signal in FM-AFM.

2.4.2 Thermal noises

Thermal excitation of the cantilever causes noise in the frequency measurement. The thermal fluctuation of the cantilever deflection is calculated using the principle of energy equipartition. The effect of thermal contact between the cantilever and a thermal reservoir at temperature T is that the cantilever is subject to thermal activation such that its mean energy equals $k_B T$. The frequency spectrum becomes white because the thermal activation is random. The rms driving amplitude density from thermal activation is given by, [29]

$$A_{Drive} = \sqrt{\frac{2k_B T}{\pi k f_0 Q}} \quad (2.19)$$

Consider the response of the cantilever for frequencies, an estimation of the thermal deflection noise is thus given by the square root of the integral of the squared driving amplitude over the measurement bandwidth B, [6]

$$\delta\Delta z = \sqrt{\frac{2k_B TB}{\pi k f_0 Q} \frac{1}{[1-(f/f_0)^2]^2 + [f/f_0 Q]^2}} \quad (2.20).$$

2.4.3 Noises in optical deflection method

In addition to the thermal noise, noises can be generated during the instrument in measuring the cantilever deflection.

One of the major noise sources in the optical deflection method is the photo diode shot noise. Here with a gain reduction factor of photo detector (ξ_{PD}) taken into account, the variation of the cantilever deflection signal ($V_{A\text{-}B}$) is given by,

$$\Delta V_{A-B} = \xi_{PD} R_{IV} \alpha \eta P B \frac{3s}{la} \Delta z \quad (2.21)$$

where R_{IV}, α, η, and P are the feedback resistor of the photodiode preamplifier, the efficiency of the light-to-current conversion at the photodiodes, the laser power attenuation coefficient in the optical path, and the output power of the laser diode, respectively. a^2 is the area of the laser spot is assumed to be square shape, and s/l is distance ratio of cantilever-PD (s) to LD-cantilever (l). The voltage noise arising from the shot noise is given by, [13]

$$\delta V_{LD} = \xi_{PD} R_{IV} \sqrt{2e\alpha\eta P B} \quad (2.22)$$

where e and B are the elementary charge and the bandwidth of the band-pass filter. From equations (2.21) and (2.22), the effective cantilever deflection noise caused by the shot noise is described by,

$$\delta\Delta z = \frac{\delta V_{LD}}{\Delta V_{A-B}/\Delta z} = \frac{la}{3s}\sqrt{\frac{2eB}{\alpha\eta P}} \quad (2.23).$$

This equation shows that the increasing laser power causes decreasing the deflection noise originated from the shot noise. For most of the well-designed optical deflection systems, the shot noise is the predominant noise component.

Another major noise source in optical deflection method is the Johnson noise originated from the resistor R_{IV} used in the preamplifier. The voltage noise arising from the Johnson noise is given by, [13]

$$\delta V_J = \sqrt{4 k_B T N_{PD} R_{IV} B} \quad (2.24)$$

where N_{PD} is the number of photodiodes used in the detector, which is 2 or 4 in most cases. From equations (2.21) and (2.24) the effective cantilever deflection noise caused by the Johnson noise is described by,

$$\delta\Delta z_J = \frac{\delta V_J}{\Delta V_{A-B}/\Delta z} = \frac{la}{3s}\frac{1}{\alpha\eta P\xi_{PD}}\sqrt{\frac{4k_B TN_{PD}B}{R_{IV}}} \quad (2.25)$$

This equation shows that the increasing laser power and the feedback resistor of the photodiode preamplifier causes decreasing the deflection noise from the Johnson noise. In most cases of the optical deflection systems, the load resistance Johnson noise is smaller than the photodiode shot noise. However Johnson noise should be taken into account when using high frequency cantilevers due to the insufficient bandwidth of the preamplifier.

The deflection noise arising from the intensity fluctuation of the laser diode driven by an automatic power control (APC) circuit is usually quite smaller than those from the shot noise and the Johnson noise. However, only small amount of the mode fluctuation of the laser diode can drastically increase the deflection noise. This is because the mode fluctuation causes a fluctuation of the spatial distribution of the laser spot on the photodiode detector. Such a fluctuation of the laser spot pattern produces a differential mode noise that is further amplified by a differential amplifier. This noise component strongly depends on the characteristics of the laser diodes and other optical components used in the optical deflection system.

2.4.4 Noise reduction for highly-sensitive force detection

For highly-sensitive force detection to achieve an atomic resolution, Fukuma et al. [13] have recently developed a low noise sensing system for the cantilever deflection. This has enabled us to determine the tip-surface force with a precision of better than 10 pN, even in liquid environments. Here the technical development of noise reduction is briefly reviewed.

Optimizing laser power

The equation (2.23) indicates that increasing output of laser power causes decreasing its shot noise. Fukuma et al. [13] reported that the deflection noise was reduced with increasing the laser power. However the deflection noise drastically

increased as the laser power exceeded a threshold. The threshold in their experiment was found to be 2.5 mW where a rated output power of their laser was 5 mW. In general, a laser diode presents intensity fluctuations originated from the spontaneous light emission, when operated with a relatively small output power compared to its rated one. As the laser power increases, such noise becomes negligible relative to the averaged laser power. Instead, the intensity fluctuations arising from the hopping of the laser oscillation mode becomes significant in the high output power regime. Mode hopping of laser caused a fluctuation of the laser spot on the deflection sensor, resulting in increase of total deflection noise in high power regime. In this study, the laser power was adjusted to be around 2 mW to minimize the deflection noise.

Radio frequency modulation of laser power

As mentioned above, the intensity fluctuation of the laser diode can produce the deflection noise of the cantilever. A laser mode hopping causes a fluctuation of the laser spot pattern on the photodiode detector. Also, the reflection and scattering of the laser beam can cause the mode hopping. The reflection and scattering of the laser beam occasionally produce some part of the laser beam going back into the optical resonator of the laser. This optical feedback causes another laser oscillation mode, leading to the increase of the mode hopping. In addition, the laser spot on the photodiode detector becomes fluctuated in a relatively long time scale, because laser beam interferes with other reflected or scattered laser beams. These noises are particularly dominant in a liquid-environment AFM. In the setup for a liquid-environment AFM as shown in Fig. 2.8, many obstacles such as cover glass and solution are inserted into the optical path of the laser beam.

These optical noises can be suppressed by modulating the laser power with a radio frequency (rf) signal whose frequency is typically 300–500 MHz. [30] The rf laser power modulation changes the laser oscillation mode from single- mode to multimode. The rf modulation considerably reduces the mode hopping induced by the optical feedback. In addition, the multimode laser beam has a lower coherence than the single-mode. Thus, the rf modulation also works well to suppress the optical interference noise.

Such an ultralow-noise deflection system demonstrates that the optimal noise

performance is limited only by cantilever thermal noise. Such a highly sensitive deflection sensor enables us to achieved atomic resolution in viscous liquid environment.

Efficient optical transmission

The laser power should be increased for reducing the deflection noise while the maximum laser power is limited for suppressing the laser mode hopping. Accordingly the laser power loss in the optical pass should be minimized.

In this respect, metal coating is beneficial. Increasing its reflectivity enhances the efficiency of the optical transmission. Small laser spot size on the cantilever backside is also helpful to increase the efficiency. In this study, the spot size was optimized to provide over 50 % of reflectivity on the metal-coated cantilever backside.

2.5 Measurement of cantilever Brownian motion in liquid environments

The microscope using in this study was equipped with the improved deflection sensor applied the noise reduction methods described in 2.4.4. Figure 2.11 shows the frequency spectrum of the typical cantilever deflection (NCH, Nanosensor) measured in an aqueous solution without piezoelectric excitation of the oscillation. The spectrum was obtained by a spectrum analyzer (4395A, Agilent.) The green dots represent the experimental measured values of the deflection noise density. The peak found in the spectrum is corresponding to the Brownian motion at the cantilever resonance while the background white noise comes from the optical deflection sensor. As the frequency spectrum of the cantilever Brownian vibration induced by the thermal energy is described by equation (2.20), the observed spectrum can be fitted as the following equation.

$$\delta\Delta z = \sqrt{\delta\Delta z_{Inst}{}^2 + \frac{2k_B T}{\pi k f_0 Q}\frac{1}{[1-(f/f_0)^2]^2 + [f/f_0 Q]^2}} \quad (2.26)$$

where $\delta\Delta z_{\mathrm{Inst}}$ represents the total instrumental noise density from the deflection sensor. The best fit was achieved as,

$$\delta\Delta z = \sqrt{1.09\times10^{-27} + \frac{4.33\times10^{-29}}{5.37\times10^{-6}\cdot f + (1-3.67\times10^{-5}\cdot f^{2})}} \quad [\mathrm{m}/\sqrt{\mathrm{Hz}}] \quad (2.27)$$

when the thermally induced noise was calculated at 300 K and k = 42 N/m. The fitting curve is presented as a blue solid line in Fig. 2.11. From equation (2.27), the noise density from the instruments was estimated as 33 fm/√Hz. This value is much smaller than the typical deflection noise density obtained with conventional optical deflection sensor, typically over 100 fm/√Hz.

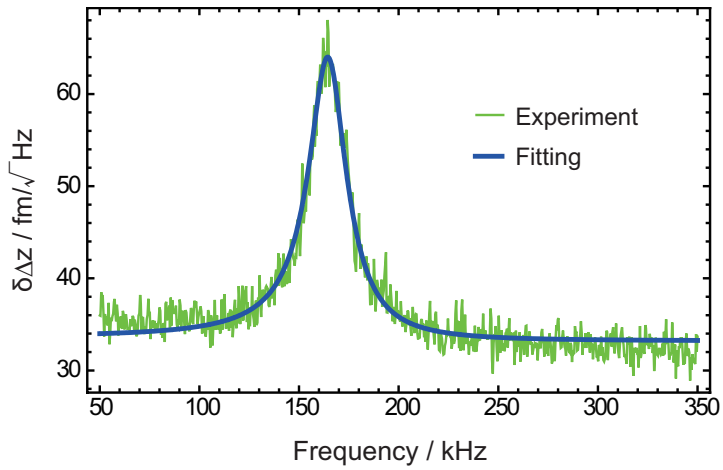

Figure 2.11. A frequency spectrum of noise density of the cantilever deflection measured by the improved optical deflection sensor using in this study. The spectrum was obtained in 1M KCl aqueous solution.

2.6 Measurement of structure of interfacial liquids

As mentioned in Chapter 1, the structure of liquids at a solid interface is of fundamental scientific interest and important for many industrial applications. The ability of highly sensitive force detection system was applied not only for obtaining the topography with subnanometer resolution, but also for determining such a structure of interfacial liquids.

At near surface less than the a few nanometers from the surface, the liquid density is often uneven because of layered distribution of interfacial liquids. When the force applied to an AFM tip is precisely determined as a function of the tip-surface distance (force-distance curve), the force strength at near surface is modulated by the layered liquids if present. On the other hand, the force would monotonously decay with increasing tip-surface distance, if the liquid density distribution were uniform as in the bulk. Such a vertical structure of interfacial liquids has been investigated over the years. In early studies, such a force modulation of related to the size of liquid molecules was observed in organic solvents on HOPG [31,32] and in water on $CaCO_3$. [33] Later, force-distance curves were observed at liquid-solid interfaces composed of various materials to examine the vertical structure of interfacial liquids. The vertical structure of layered liquids has been investigated on various solids and liquids, as summarized in recent reviews [34-37].

However, the structure of interfacial liquids is potentially sensitive to the local structure and composition of solids. A sensitive detection techniques of the oscillatory solvation force presented by the solvation layers formed at a solid-liquid interface, is needed to reach the goal to achieve subnanometer scale lateral resolution. As mentioned in the previous subsection, FM-AFM can be a powerful tool to sensitive force detection. The challenge of operating FM-AFM in liquid was initiated by Jarvis et al. in 2000. [38] The situation was dramatically changed in 2005 when the low noise optical deflection sensing system that is described in 2.4.4 has been developed by Fukuma et al. [13] The highly sensitive force detection systems enable to achieve an atomic resolution in liquid. Atomically resolved in lateral dimension reflected in modulations of force-distance curves at a lateral position. Thus a two-dimensional maps of the force applied to the tip were further determined in subnanometer scale.

Two-dimensional cross-sectional Δf distribution was obtained as the following

procedure. The tip was scanned vertically forward the surface. The frequency shift was measured as a function of the vertical coordinate to obtain one Δf-distance curve at one lateral coordinate. The tip was then laterally shifted by a fixed spacing, and then another vertical scan was done. By repeating Δf-distance curve measurement along lateral coordinate, a Δf distribution cross-sectional to the substrate was constructed. A few example of the cross-sectional distribution was acquired at a water-mica [15,16] and water-protein [15] interface. Site-specific modulations were found in the cross-sectional distribution, which was considered to relate the density modulation of water. In the current study, the cross-sectional distribution is obtained various solid-liquid interfaces to discuss the structure of interfacial liquids.

1. A tip is scanned vertically to the surface. The applied force was monitored as a function of tip-surface distance.

2. After one vertical scan, the tip is then laterally shifted by a fixed spacing and another vertical scan is done. By repeating scans along the lateral coordinate, cross-sectional force distribution is obtained.

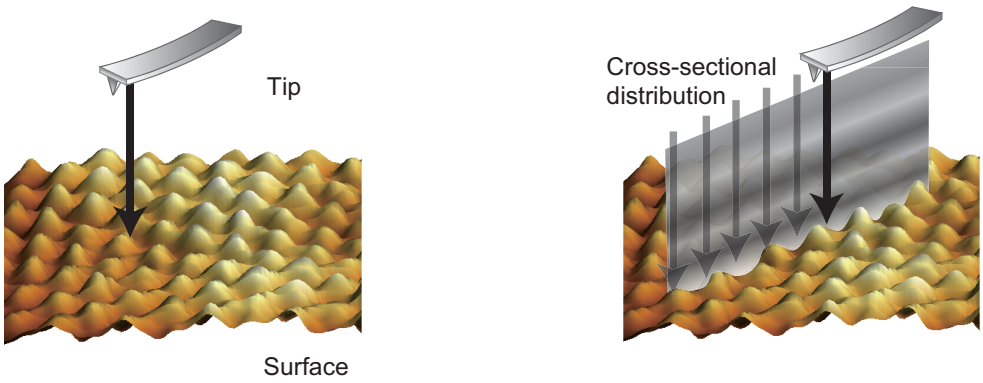

Figure 2.12. Typical procedure to obtain the two-dimensional force (frequency shift) distribution cross-sectional to the surface.

References in Chapter 2

[1] G. Binnig, C. F. Quate, and Ch. Gerber, *Phys. Rev. Lett.* 56 (1986) 930.

[2] G. Binnig, Ch. Gerber, E. Stoll, T. R. Albrecht and C. F. Quate, *Europhys. Lett.* 3 (1987) 1281.

[3] J. B. Pethica, *Phys. Scr. T* 19 (1987) 61.

[4] F. J. Giessibl and G. Binnig, *Ultramicroscopy* 42-44 (1992) 281.

[5] F. Ohnesorge and G. Binnig, *Science* 260 (1993) 1451.

[6] T. R. Albrecht, P. Grütter, D. Horne, and D. Rugar, *J. Appl. Phys.* 69 (1991) 668.

[7] F. J. Giessibl, *Science* 267 (1995) 68.

[8] S. Kitamura and M. Iwatsuki, *Jpn. J. Appl. Phys.* 34 (1995) L145.

[9] H. Ueyama, M. Ohta, Y. Sugawara, and S. Morita, *Jpn. J. Appl. Phys.* 34 (1995) L1086.

[10] Y. Sugawara, M. Ohta, H. Ueyama, and S. Morita, *Science* 270 (1995) 1646.

[11] Y. Sugimoto, T. Namikawa, K. Miki, M. Abe, and S. Morita, *Phys. Rev. B* 77 (2008) 195424.

[12] T. Fukuma, K. Kobayashi, K. Matsushige and H. Yamada *Appl. Phys. Lett*. 86 (2005) 193108.

[13] T. Fukuma, M. Kimura, K. Kobayashi, K. Matsushige and H. Yamada, *Rev. Sci. Instrum.* 76 (2005) 053704.

[14] B. W. Hoogenboom, H. J. Hug, Y. Pellmont, S. Martin, P. L. T. M. Frederix, D. Fotiadis, and A. Engel, *Appl. Phys. Lett.* 88 (2006) 193109.

[15] K. Kimura, S. Ido, N. Oyabu, K. Kobayashi, Y. Hirata, T. Imai, and H. Yamada, *J. Chem. Phys.* 132 (2010) 194705.

[16] T. Fukuma, Y. Ueda, S. Yoshioka, and H. Asakawa, *Phys. Rev. Lett.* 104 (2010) 016101.

[17] J. N. Israelachvili, *Intermolecular and Surface Forces 3rd Ed.*, Academic Press, London, 2011.

[18] S. Ciraci, A. Baratoff, and I. P. Batra, *Phys. Rev. B* 41 (1990) 2763.

[19] R. Pérez, M. C. Payne, I. Štich, and K. Terakura, *Phys. Rev. Lett.* 78 (1997) 678.

[20] R. Pérez, I. Štich, M. C. Payne, and K. Terakura, *Phys. Rev. B* 58 (1998) 10835.

[21] J. Tóbik, I. Štich, R. Pérez,and K. Terakura, *Phys. Rev. B* 60 (1999) 11639.

[22] A. I. Livshits, A. L. Shluger, A. L. Rohl, and A. S. Foster, *Phys. Rev. B* 59 (1999) 2436.

[23] A. Abdurixit, A. Baratoff, and E. Meyer, *Appl. Surf. Sci.* 157 (2000) 355.

[24] S. H. Ke, T. Uda, I. Štich, and K. Terakura, *Phys. Rev. B* 63 (2001) 245323.

[25] J. Tóbik, I. Štich, and K. Terakura, *Phys. Rev. B* 63 (2001) 245324.

[26] L. N. Kantorovich, A. L. Shluger, and A. M. Stoneham, *Phys. Rev. B* 63 (2001) 184111.

[27] C. J. Chen, *Introduction to Scanning Tunneling Microscopy,* Oxford University Press, 1993

[28] J. E. Sader and S. P. Jarvis, *Appl. Phys. Lett.* 84 (2004) 1801.

[29] S. Morita, R. Wiesenganger, and E.Meyer, Eds., *Noncontact Atomic Force Microscopy*, Springer, 2002.

[30] M. Ojima, A. Arimoto, N. Chinone, T. Gotoh, and K. Aiki, *Appl. Opt.* 25 (1986) 1404.

[31] S. J. O'Shea, M. E. Welland, and T. Rayment, *Appl. Phys. Lett.* 60 (1992) 2356.

[32] S. J. O'Shea, M. E. Welland, and J. B. Pethica, *Chem. Phys. Lett.* 223 (1994) 336.

[33] J. P. Cleveland, T. E. Schäffer, and P. K. Hansma, *Phys. Rev. B* 52 (1995) 8692.

[34] H.-J. Butt, B. Cappella, and M. Kappl, *Surf. Sci. Rept.* 59 (2005) 1.

[35] T. Fukuma, *Jpn. J. Appl. Phys.* 48 (2009) 08JA01.

[36] S. J. O'Shea, N. N. Gosvami, L. T. W. Lim, and W. Hofbauer, *Jpn. J. Appl. Phys.* 49 (2010) 08LA01.

[37] R. Hayes, G. G. Warr, and R. Atkin, *Phys. Chem. Chem. Phys.* 12 (2010) 1709.

[38] S. P. Jarvis, T. Uchihashi, T. Ishida, and H. Tokumoto, *J. Phys. Chem. B* 104 (2000) 6091.

Chapter 3: Understanding Applied Force in Liquids Related to Interfacial Structure of Liquids

3.1. Introduction

As mentioned in Chapter 2, AFM has been a powerful tool for the investigation of liquid-solid interfaces. It is now possible to observe the structure of interfacial liquid in addition to the topography of a solid. When a liquid is structured over a solid to form liquid layers on the surface, modulations appear in force distance curve. The latest technical development by Fukuma et al. [1] reduced the noise of frequency-modulation AFM (FM-AFM) to less than 20 fm $Hz^{-1/2}$. The improved force sensitivity allows weak-force detection. Using the improved microscope, molecular-scale modulations of force-distance curves were found at aqueous interfaces of mica [2,3] and bacteriorhodopsin. [3] In this chapter, the ability of such microscopes to detect interfacial liquid is experimentally demonstrated at aqueous solution-metal oxide interface. Here it is discussed how the force modulations relates to the density modulation of liquid molecules by comparing them with the density distributions obtained by X-ray diffraction or molecular dynamics simulation.

It is also important for interpreting the force distribution to understand the role of the tip in loading the force. The tip apex was shown to play an important role in simulations of AFM at liquid-solid interfaces. [4,5] A small tip apex is desirable to detecting the weak force with high spatial resolution. However experimental knowledge of the tip apex is quite limited, especially for tips scanned in liquids. In this chapter, two commercially available silicon cantilevers with sharpened or cone-shaped tips was used to compare the topography and force-distance curves at water-mica and alkane-thiolate monolayer. The presence and role of atomistic minitips on the tip bodies are discussed. In addition, chemical composition of the tip apex could affect the force contrast. This was also verified with observing alcohol-HOPG interface where the surface shows the chemical heterogeneity due to the alcohol adsorbates.

3.2 Experimental methods

3.2.1. Substrates

Muscovite mica (Furu-uchi Chemical) was cleaved with scotch tape to use as a substrate. The dodecanethiol self-assembled monolayer was prepared on Au(111) films of 150 nm thickness deposited on cleaved mica wafers. The gold-deposited wafers were soaked in a 1 mM ethanol solution of 1-dodecanethiol (Wako, >98%) for 24 hours. The soaked wafers were rinsed several times with pure ethanol and immersed in the imaging liquid. Experimental details of the preparation of SAM are described in the later chapter.

An α-Al_2O_3(01-12) wafer ($10 \times 10 \times 0.5 mm^3$, Shinko-Sha) was washed with concentrated nitric acid, ultrasonically rinsed with pure water, dried in a N_2 flow, and calcined in air at 1273 K for 12 hours. A rutile TiO_2(110) wafer ($10 \times 10 \times 0.3 mm^3$, Shinko-Sha) was calcined in air at 1273 K for 12 hours. The calcined wafer was fully oxidized and transparent for visible light. The wafers were cooled, immediately placed in a homemade liquid AFM cell as described in Fig. 2.8.

Highly oriented pyrolytic graphite ($10 \times 10 \times 1.2 mm^3$, ZYA Quality, NT-MDT) was cleaved with scotch tape to use as a substrate.

3.2.2. Imaging solutions

The KCl solution was prepared at a concentration of 1 mol L^{-1} with KCl (Nakarai, >99.5%) dissolved in Millipore water. Minimizing the electric double layer force was important to observe force modulations caused by hydration layers. This was achieved with the strong screening in the electrolyte solution of this concentration. *n*-Hexadecane (Wako, >97%) and 1-decanol (Wako, >97%) was used as received. Approximately 30 μL droplet of these imaging liquids was put on the substrates for scans.

3.2.3. Microscope and cantilevers

Topography and force-distance curves were determined in the aqueous KCl solution, neat *n*-hexadecane, or 1-decanol, using a modified Shimadzu SPM 9600 microscope. The microscope equipped the optimized low-noise force detection system as mentioned in Chapter 2. The deflection noise of the microscope had been reduced to less than 20 fm $Hz^{-1/2}$. The low deflection noise is critical for the observation of weak tip-surface forces in liquids.

The frequency shift of the cantilever oscillation was detected with a phase locked loop and the oscillation amplitude was regulated to be constant with a feedback loop. The absolute amplitude was estimated by comparing the theoretical amplitude of the cantilever Brownian motion to the cantilever deflection sensor output recorded with a spectrum analyzer (Agilent, 4395A). In this measurement the divided photodiodes had a differential readout of 1 V when the cantilever was deflected by 5 nm.

Two commercial silicon cantilevers with different tip radii, 10 nm (Nanosensors, NCH) and 250 nm (Team Nanotech, LHCR250), were used. The shape of the tips was checked after imaging scans using a scanning electron microscope (JEOL, JSM-5610). As mentioned in Chapter 2, a stiff cantilever is essential for sensitive force detection. The nominal spring constants of NCH and LHCR provided by the suppliers, are 40 N m^{-1} for each cantilever. NCH cantilevers were coated with aluminum on the back surface (NCH-R) when used in hexadecane or decanol, and coated with gold in the aqueous solution. LHCR cantilevers were coated with aluminum on the back surface. The resonance oscillation frequency of the cantilevers was in the range of 140-190 kHz, and the quality factor (Q) of resonance was 5-10 in liquids. To remove spurious oscillation in low Q environments, a bandpass filter of Q = 20 was inserted in the feedback loop to regulate the oscillation amplitude constant.

Topography was obtained with regulation of the tip-surface distance to keep the frequency shift (Δf) constant. Cross-sectional Δf distribution to the surface was acquired as described in section 2.5. All the experiments were performed at room temperature. The vertical drift of the tip was less than 0.1 nm min^{-1} relative to the surface. The typical acquisition time of one Δf-distance curve was 0.25 s.

3.3. Interpretation of applied force in liquids

3.3.1. Δf-distance curve over α–Al_2O_3

The author started by determining *Δf*-distance curve over α–Al_2O_3 (01-12) surface in an aqueous solution. The density distribution of water was experimentally determined on the (01-12) surface using XCTR. It is important in this study to compare the force-distance curves obtained by AFM with the water density distribution.

One hundred *Δf*-distance curves were observed at different lateral positions over the Al_2O_3 surface. Panel (a) of Fig. 3.1 presents a two-dimensional *Δf* distribution constructed with the consecutive scans of *Δf*-distance curves. Four of individual curves are shown as (i)-(iv) in panel (b). The four curves were observed within the lateral distances of a few nanometers, as evidenced in (a), and presented different *Δf* features as a function of the vertical distance. The forward (i) curve was determined with the tip approaching the surface, whereas the backward (i) curve was determined with the tip leaving the surface at the same lateral position. The identical features of the two curves suggest that the *Δf*-distance measurements were reproducible at a fixed lateral position.

The different shapes of curves (i)-(iv) indicate that the tip-surface force is heterogeneous over the surface. Using established a quantitative relationship [6] the frequency shifts were converted to the force. The 100 *Δf*-distance curves were thereby converted to 100 force-distance curves. Definition of the zero tip-surface distance is not a trivial issue in this case. The current definition in Fig. 3.1(b) was the distance where the converted repulsive force exceeds 350 pN.

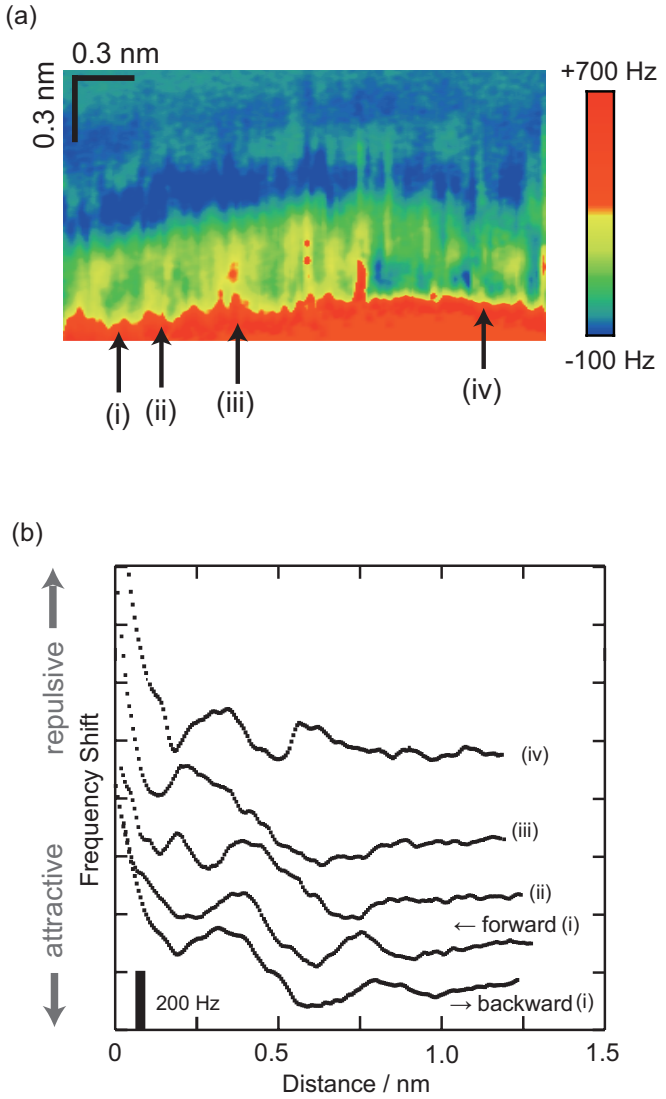

Figure 3.1. Frequency shift-distance curves over the Al_2O_3(01-12) surface. Panel (a) shows a two-dimensional distribution of the frequency shifts. Four curves observed at positions (i)-(iv) were shown in panel (b). Forward (i) curve and backward (i) curve were determined with the tip approaching the surface and leaving from the surface, respectively. Cantilever oscillation amplitude: 0.2 nm.

3.3.2. Electric double layer force

The AFM tip and Al_2O_3 surface are accompanied by their own electric double layers when immersed in the electrolyte solution. The gradient of the ion concentration is modified in the overlapped portion of the double layers. The energy consumption or gain to modify the gradients causes the tip-surface force of long-range decaying background. [8]

For the case when only counterions are present near the surface, the chemical potential μ is written as,

$$\mu = ze\psi + kT\log\rho \quad (3.1)$$

where ψ is the electrostatic potential and ρ is the number of density of ions of its valancy z and the elementary charge e. From the equilibrium requirement that the chemical potential be the same throughout the all the position, equation (3.1) shows the Boltzmann distribution of counterions.

$$\rho = \rho_0 \exp(-\frac{ze\psi}{kT}) \quad (3.2)$$

Another important fundamental equation is the well-known Poisson equation for the net excess charge density at x:

$$ze\rho = -\varepsilon\frac{d^2\psi}{dx^2} \quad (3.3)$$

which when combined with the Boltzmann distribution, equation (3.2), give the Poisson-Boltzmann (PB) equation:

$$\frac{d^2\psi}{dx^2} = -\frac{ze\rho_0}{\varepsilon}\exp(-\frac{ze\psi}{kT}) \quad (3.4).$$

When solved, the PB equation gives the potential ψ and ion density ρ at any point x between the two surfaces.

Differential of equation (3.2) is described using equation (3.4) as,

$$\rho_x - \rho_0 = \frac{\varepsilon}{2kT}\int_0^x d\left(\frac{d\psi}{dx}\right)^2 = \frac{\varepsilon}{2kT}\left(\frac{d\psi}{dx}\right)_x^2 \quad (3.5)$$

which gives ρ at any point x in terms of at the midsurface density ρ_0 and $d\psi/dx$. The interaction pressure between two identically charged surface in an electrolyte solution can be derived quite simply as follows,

$$P_x(d) - P_x(\infty) = -\frac{\varepsilon}{2}\left[\left(\frac{d\psi}{dx}\right)^2_{x(d)} - \left(\frac{d\psi}{dx}\right)^2_{x(\infty)}\right] + kT\left[\sum_i \rho_{xi}(d) - \sum_i \rho_{xi}(\infty)\right] \quad (3.6)$$

for any x or d, where $\Sigma\rho_{mi}$ is the total ionic concentration of the center of the two surfaces at $x = d/2$. Incorporating equation (3.5) into (3.6) and again putting $P_x(d = \infty) = 0$, yields two useful and equivalent expressions for the pressure:

$$P_x(d) = kT\left[\sum_i \rho_{mi}(d) - \sum_i \rho_{mi}(\infty)\right] \quad (3.7).$$

Here assuming the midsurface potential ψ_m, equation (3.7) is written for a 1:1 electrolyte such as KCl,

$$\begin{aligned} P &= kT\rho_\infty\left[\left(\exp(-\frac{e\psi_m}{kT}) - 1\right) + \left(\exp(+\frac{e\psi_m}{kT}) - 1\right)\right] \\ &= 2kT\rho_\infty\left[\cosh(\frac{e\psi_m}{kT}) - 1\right] \end{aligned} \quad (3.8)$$

Also for a 1:1 electrolyte, the midsurface potential are given from (3.5),

$$\psi_x = \frac{2kT}{e}\log\left[\frac{1+\gamma\exp(-\kappa x)}{1-\gamma\exp(-\kappa x)}\right] \approx \frac{4kT}{e}\gamma\exp(-\kappa x) \quad (3.9)$$

where

$$\gamma = \tanh(\frac{e\psi_0}{4kT}) \quad (3.10)$$

$$\frac{1}{\kappa} = \sqrt{\frac{\varepsilon k_B T}{e^2 z^2 \rho_\infty}} \quad (3.11).$$

Here $1/k$ is called as the Debye length of the solution. Equation (3.9) is known as the Gouy-Chapman theory. For potentials is low (typically for under 25 mV), equation (3.9) reduces as:

$$\psi_x \approx \psi_0 \exp(-\kappa x) \quad (3.12).$$

This is called as Debye-Hückel equation where the Debye length appears as characteristic decay length of the potential. Considering that ψ_m is simply the sum of the potentials from each surface at $x = d/2$, then ψ_m is given by equation (3.9) as:

$$\psi_m = 2\frac{4kT}{e}\gamma\exp(-\kappa\frac{d}{2}) \quad (3.13)$$

Inserting equation (3.13) into (3.8), the final result for the repulsive pressure between two planer surface:

$$P \approx \frac{e^2 \psi_m{}^2 \rho_\infty}{kT} \qquad (3.14)$$
$$= 64 kT \rho_\infty \gamma^2 \exp(-\kappa \cdot d)$$

At low surface potential the equation simplify to the following.

$$P \approx 2\varepsilon\kappa^2 \psi_0{}^2 \exp(-\kappa \cdot d) \quad (3.15)$$

In a similar fashion, an approximate equation for the pressures of two asymmetric surface whose potential is unequal but constant potential in 1:1 electrolyte is described for two plane surfaces as:

$$P = \frac{2\varepsilon\kappa^2 \left[(e^{+\kappa d} + e^{-\kappa d}) \psi_1 \psi_2 - (\psi_1{}^2 + \psi_2{}^2) \right]}{(e^{+\kappa d} - e^{-\kappa d})^2} \quad (3.16)$$

At large separations ($d >> 1/\kappa$), equation (3.16) is described as:

$$P \approx 2\varepsilon\kappa^2 \psi_1 \psi_2 \exp(-\kappa \cdot d) \quad (3.17)$$

In an analogous way, Butt *et al.* [9,10] described an analytical form of EDL force with a spherical tip of radius R and a plane surface as a function of tip-surface distance d as:

$$F = \frac{4\pi R \sigma_{tip} \sigma_{sur}}{\varepsilon\kappa} \cdot \exp(-\kappa \cdot d) \quad (3.18)$$

σ_{tip} and σ_{sur} are the surface charge density on the tip and surface. In the preceding equation, $\psi_{tip/sur}$ and $\sigma_{tip/sur}$ are related by $\sigma = \varepsilon\kappa\psi$.

The 100 force-distance curves over α–Al_2O_3 (01-12) surface were averaged and fitted to the function (3.18), as shown in Fig. 3.2. The best fit was achieved with,

$$F = 3.2\times10^{-10}\ \mathrm{N} \cdot exp(-6.8\times10^{9} \cdot d / \mathrm{m}) \quad (3.19).$$

The Debye length deduced from the fitted function was 0.15 nm. This length agreed with the length from the equation (3.11), 0.20 nm. A negative σ_{tip} is assumed on a silicon tip after ref. 11. Thus the positive sign of the pre-exponential factor of the fitted function (3.19) suggests a negative σ_{sur} of the Al_2O_3 wafer. The suggested negative charge density is consistent with literature. The isoelectronic point was reported to be

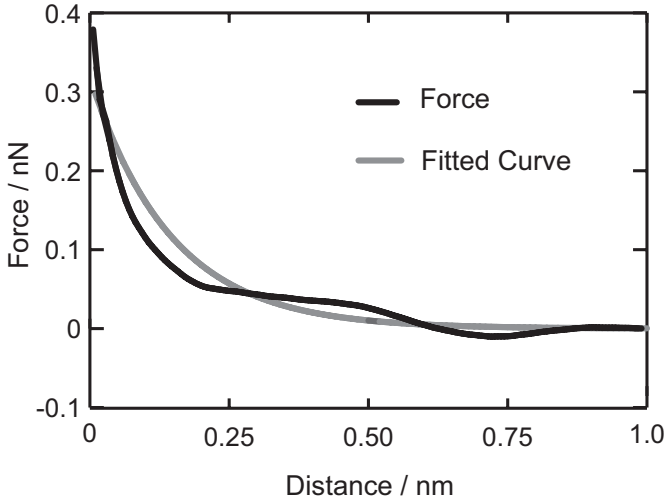

Figure 3.2 The force-distance curve averaged over the solution-Al_2O_3 interface. The exponential function fitted to the observed curve is shown with the gray line.

pH 5 in a sum-frequency study [12] and pH 5-6 in a surface force study. [13] Negative charge density was estimated on solution-alumina interfaces at pH 7. [14,15] Employing the typical radius *R* of NCH cantilever is 10 nm, the surface charge density of the tip and surface was estimated as in the order of -10^{-2} C/m. Silica and alumina presented around -10^{-2} C/m of charge density in the previous report. [15,16] The observed value is reasonable as long as the order estimation. However the propriety of fitting to equation (3.19) is limited due to the ambiguities of the tip radius, which makes quantitative discussion difficult about the surface charge density provided from the fit.

A short-ranged, monotonic, repulsive surface force was found in the previous study at sapphire-solution-sapphire interfaces. [16] The observed surface force was interpreted with energy cost to collapse the hydration shell of solute cations. A number of hydrated cations should have been pinched and collapsed in the two sapphire plates of a macroscopic size. On the other hand, pinching a K^+ cation should be rare in the small tip apex and the sapphire surface. The contribution of the shell-collapse force is thus less probable with the tip-surface force depicted in Fig. 3.2.

3.3.3. Interfacial water structure over α–Al_2O_3

The 100 Δf-distance curves were converted to 100 force-distance curves with equation (2.17). [6] The EDL force represented by function (3.19) was subtracted from the force curves. Figure 3.3 shows the four subtracted curves deduced from curves (i)-(iv) in Fig. 3.1. Each subtracted force-distance curve should contain two force terms; the force induced by inhomogeneous distribution of water molecules, and the van der Waals force from the solid. The repulsive contribution of the van der Waals force is apparent at distances smaller than 0.1 nm. The attractive contribution of the van der Waals force is less evident and perhaps present at distances of 0.2-0.5 nm.

The water-induced force provides force oscillations. The force curves present different features as a function of the distance with local maxima at distances of 0.2, 0.4, 0.6 and 0.8 nm. The heterogeneity of force-distance curves is ascribed to the uneven distribution of structured water over the surface. The layered structure of water distribution is present in a limited region from the surface, whose thickness should be less than 1 nm. It is thus supposed that the tip penetrating into the structured region was small enough to recognize the laterally inhomogeneous distribution of the water. The lateral structure therefore was not averaged out. This is frequently assumed in AFM studies. Structured water interacts with the tip apex, and the resonant oscillation of the whole cantilever is affected by the force applied on the tip apex. The tip body protrudes out of the structured region and remains in the bulk solution. The number of water molecules in contact with the tip body, and hence the force applied to the tip body is insensitive to the tip-surface distance. This scheme is illustrated in Fig. 3.4. The existence of extremely small tip has been also experimentally evidenced using the sharp and blunt tips as described in the following section.

Suppose such an infinitely small tip, the potential is given by the convolution of the density distribution of water molecules ρ and the tip-water pair potential u, as: [2]

$$U(r_t) = \int \rho(r) \cdot u(r - r_t) dr \tag{3.20}$$

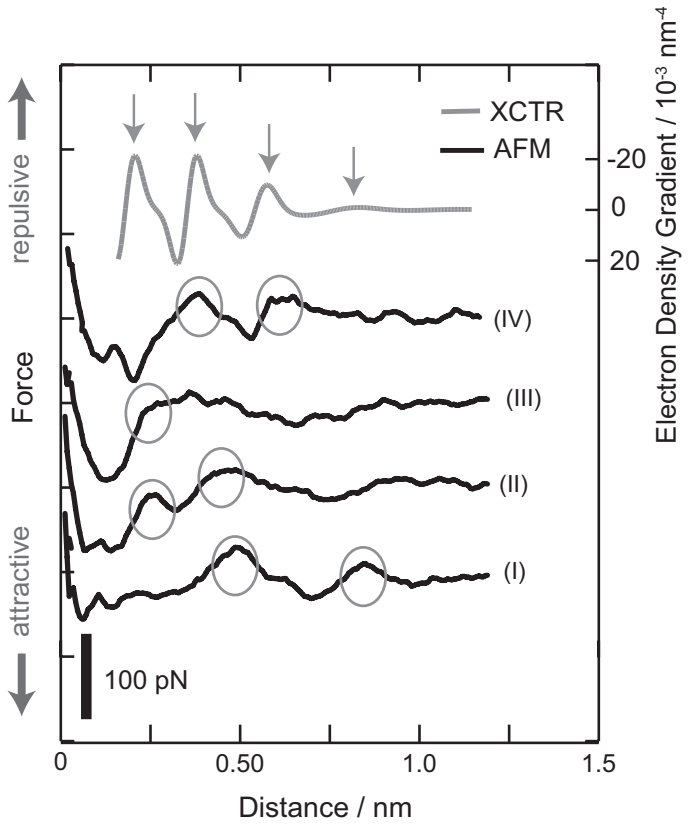

Figure 3.3. The subtracted force-distance curves over the aqueous-Al_2O_3 interface. The Δf-curves (i)-(iv) in Fig. 3.1 were converted to force-distance curves. The averaged EDL force in Fig. 3.2 was subtracted from each converted force curve. Curves (I)-(IV) were deduced from converted curves (i)-(iv) in Fig. 3.1. Local maxima of the repulsive tip-surface force are indicated with circles. The electron density distribution found in an XCTR study [17] was differentiated with respect to the vertical coordinate, inverted in the sign, and inserted on the top of the figure. Local minima of the electron density gradient are marked with arrows.

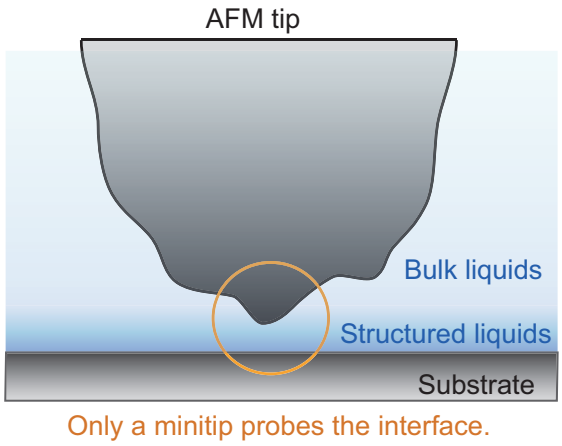

Figure 3.4. Minitip penetrating into the structured liquid.

Here, U is the convoluted potential and r_t is the coordinate of the tip. When the pair potential is simplified to a δ function,

$$u(r - r_t) \approx \delta(r - r_t) \quad (3.21)$$

the convoluted potential is proportional to the density distribution.

$$U(r_t) \propto \rho(r_t) \quad (3.22)$$

The force applied on the tip is given by the gradient of U and therefore proportional to the gradient of the density distribution.

$$F(r_t) \propto -\nabla\rho(r_t) \quad (3.23)$$

Based on this assumption, the author compared the force-distance curves with the gradient of the electron density distribution determined in an XCTR study. [17] The sign of the electron density gradient is inverted and inserted on the top of Fig. 3.3. According to equation (3.23), each force maximum should correspond to a local minimum of the electron density gradient. This was the case with the results shown in Fig. 3.3.

The magnitude of the force modulations supports the current assumption of probing local density distribution. The amplitude of the modulations was observed to be 30-70 pN. Such small amplitude of force suggests small area where the modulated force was

loaded. Suppose that effective loading area of the force is estimated to be the order of a few nanometers square, hydrostatic pressure near the surface is the order of 1 MPa, that is reasonable value as about 10 times as ambient pressure. The detail discussion of the small loading area of the tip is described in 3.5.

The four force curves are not completely identical. This suggests different manners of hydration on different lateral positions. Water is dissociated on Al^{3+} cations to produce hydroxyl end-groups. The hydroxyl end-groups can create hydrogen bonds with water in the solution. The water density distribution may be modified in the presence or absence of Al^{3+} cations and hydroxyl end-groups. The XCTR results [17] reveal the density distribution laterally averaged over the interface. On the other hand, the force-distance curves represent the unaveraged density distribution probed by the AFM tip. In this respect, the XCTR-based density distribution gradient can be related to an average of force-distance curves, rather than individual curves.

3.3.4. Δf-distance curve over TiO_2

Another example of discussion in the relationship between the force and liquid density was provided at an aqueous-TiO_2 interface. A frequency shift-distance curve is shown in Fig. 3.5(a) with the tip scanned from the solution to the surface. The amplitude of the tip oscillation was simultaneously watched to be constant. The observed frequency shift (a) was transformed to the force applied toward the tip (b) with the force conversion algorithm developed by Sadar and Jarvis. [6] In this force-distance curve, zero force is defined as the force at 2.6 nm, the maximum distance examined in our measurements. The scale of the vertical static deflection was calculated on the sensitivity of optical deflection sensor described in 3.2.3. The time-averaged vertical deflection of the cantilever was fluctuated as little as 0.1 nm with no systematic shift as a function of the tip-surface distance. The actual tip-surface distance can thus be properly projected on the horizontal scale of Fig. 3.5. Zero distance of Fig. 3.5 was defined as the minimum distance examined in the current measurements. With distances smaller than that length the cantilever oscillation was no more excited by the piezo actuator, which was also intended to preserve the sharp tip apex from undesired tapping.

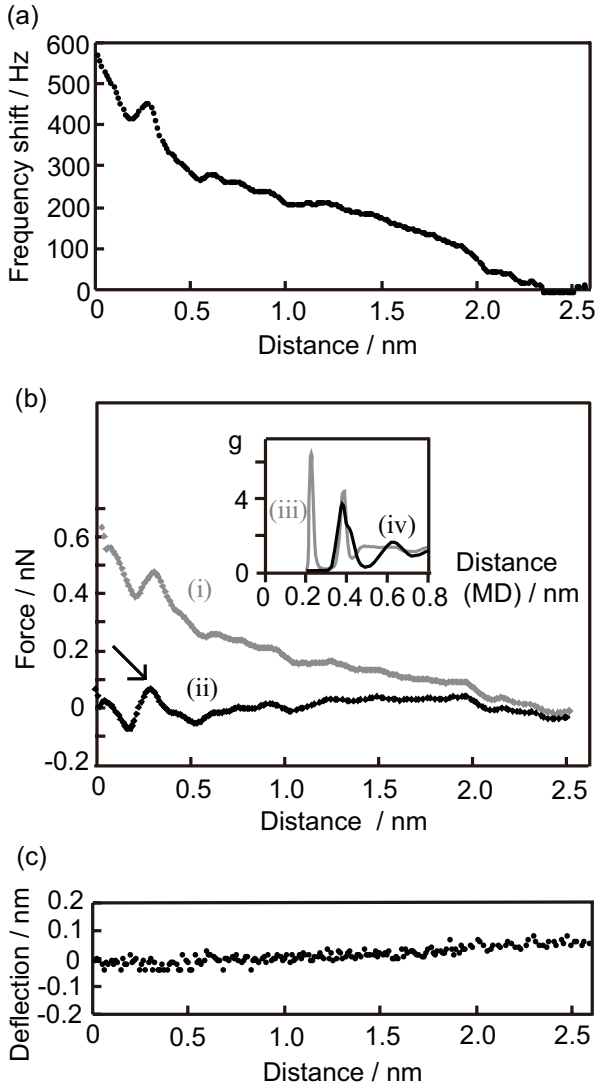

Figure. 3.5. The frequency shift of the cantilever resonance (a) and vertical deflection of the cantilever (b) as a function of the tip-surface distance. Two curves inserted in (a) present the occupation probability predicted in a molecular dynamic calculation. [7] The black and gray curves were predicted on a hydroxylated and nonhydroxylated TiO_2 (110) surfaces.

The repulsive tip-surface force gradually decayed with the distance in Fig. 3.5(a). This monotonic decay is ascribed to the electric double layers formed at the TiO_2-solution interface and at the tip-solution interface as discussed in subsection 3.3.2.

The repulsive, double layer force exponentially decays with the distance from the surface as equation (3.18). The exponential, background term (F_B) was deduced by fitting curve (i) to a function,

$$F_B(z) = a \cdot \exp(-b \cdot z) \qquad (3.24)$$

where z represents the distance with two fitting parameters, a and b. The best fit was achieved with a = 0.583 nN and b = 1.12 nm^{-1}. The Debye length (b^{-1}) is larger than the theoretical value of 1 M KCl solution. This would be due to the hydrophobic property of TiO_2 surface. The detail discussion is described in Chapter 6.

Here the author focused on the force modulations on the force-distance curve. The fitted F_B was subtracted from the raw force to make curve (ii) of Fig. 3.5(b). The subtracted force curve (ii) presents a local maximum at 0.3 nm as marked with an arrow. As discussed in the subsection 3.3.4, the modulations is assumed to relate with the density distribution of water molecules. The suggested relationship is successfully supported by a theoretical simulation. In the present water-TiO_2(110) interfaces, a molecular dynamic simulation was demonstrated by Pedota *et al.* [7] The simulation predicted the axial density of water molecules on hydroxylated and non-hydroxylated TiO_2(110) surfaces. The simulated density curves are inserted in Fig. 3.5(b). On the non-hydroxylated surface, two maxima were found at 0.22 and 0.38 nm from the top Ti atom plane. The first maximum at 0.22 nm represents water molecules adsorbed on the five-fold coordinated Ti atoms. The second-nearest maximum at 0.38 nm corresponds to a water molecule array out of contact to the TiO_2 surface. On the hydroxylated surface one maximum for the out-of-contact water was predicted at 0.38 nm. The observed force curve presents a positive peak at 0.3 nm, and the peak shape is similar to that of the simulated out-of-contact water array at 0.38 nm. The author hence considers the relation of the out-of-contact array of water to the experimentally observed force peak. The adsorbed water at 0.22 nm, if any, is recognized by the tip as a part of the surface rather than the structured water in the solution.

Figure 3.6 shows seven frequency shift-distance curves successively observed. Intervals from one curve to another were one second. The curves represent the solution

structure at different lateral positions, because a finite drift of the tip was present relative to the surface. The shape of the curves was sensitive to the lateral positions. This was similar to α-Al_2O_3(01-12) interface and suggests the laterally heterogeneous structure of the solution. The shape of the curves was not randomly fluctuated. One major type has a positive peak at 0.4 nm, one of which was seen in Fig. 3.4(a). Curves of this type are shown with black lines in Fig. 3.6. The peak at 0.4 nm is suppressed on curves of the other type, as shown with gray lines. The characteristic features of the two major types were reproducibly observed as shown in Fig. 3.6 and also in separate series of measurements. The laterally heterogeneous structures of the solution are also found at the TiO_2 interface, possibly caused by heterogeneity of the surface.

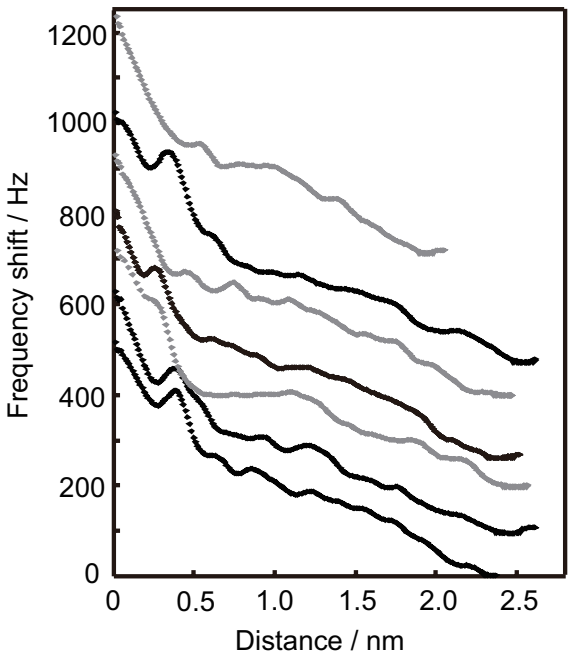

Figure 3.6. Serially observed frequency shift-distance curves. Seven curves were determined at one-second intervals from the bottom to the top. Each curve is shifted by 0, 100, 200, 300, 400, 475, and 700 Hz for illustration. Four curves with a local maximum at 0.4 nm are presented in black, while three curves without the maximum are in gray.

Here the author briefly summarized the section 3.3. An α-Al_2O_3(01-12) and TiO_2(110) surface immersed in a concentrated aqueous electrolyte solution was probed with an advanced FM-AFM. The force distance curves composed of short-range oscillatory modulations and monotonic long-range decay. The modulations of the force-distance curve reflect the molecular-scale liquid structure at the interface, and the monotonic decay does the electrostatic force produced by the overlapped electric double layers of the tip and surface. The observed force modulations were consistent with the intrinsic water density distribution of a previous XCTR or MD simulation result. From these comparisons, the author suggests a simple model that the small tip apex probes the water-induced force modulations, and the modulations are approximately proportional to the gradient of the water density distribution. This is a reasonable model and a good start point for interpreting the force.

Establishing a better quantitative relation of the density distribution and force distribution is an important issue for further studies. To accomplish this, factors including real tip size and potential needs to be included in more precise sense. Theoretical force simulation with consideration of these factors can be an effective approach. However there still remains difficulty to determine the exact shape of the tip apex of loading the force, because it is too small to be observed experimentally and easily changeable during the measurements. It is therefore important for interpreting the force distribution to understand the role of the tip apex. In the next section, the role of the tip apex in liquids is discussed in loading the force. Thorough the experimental insights of the role of the macroscopic shape of tip, the author propose a better way to handle a real tip shape in quantification of the interpretation of the force.

3.4. Role of tip apex in force-distance curve measurement in liquid

In this section, the role of tip apex in AFM measurement in liquids is discussed. compared with the results obtained using the sharpened (NCH) and cone-shaped tip (LHCR).

3.4.1. Tip body shape

Getting discussion started on macroscopic shape of the two different the tip. The shape of the tips was monitored after AFM imaging scans with a scanning electron microscope (SEM; JEOL, JSM-5610). Figure 3.7 presents the SEM images of the tips after scans. There was no sign of tip-surface collisions during the scans. The tip of the NCH-R cantilever remained sharp, as expected from the nominal radius of 10 nm. The tip of the LHCR cantilever retained its cone shape with a 250 nm radius.

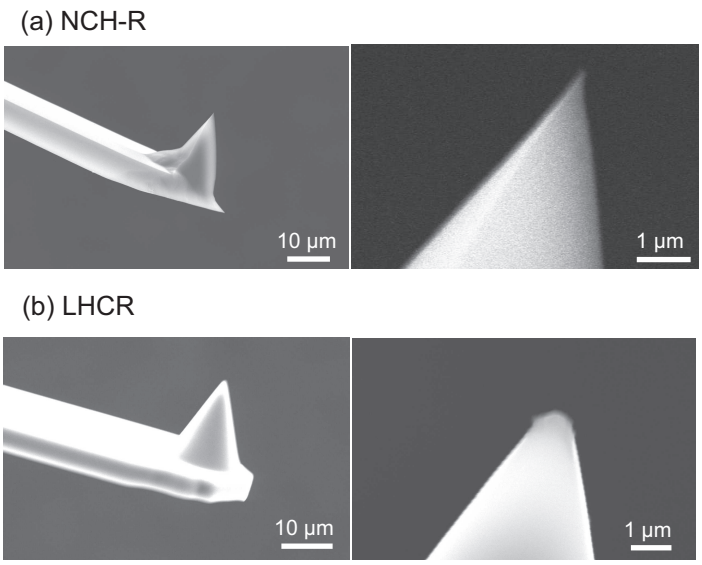

Figure 3.7. SEM images of the (a) NCH-R and (b) LHCR cantilevers after use in AFM measurements of the interface of hexadecane and dodecanethiol SAM. The right-hand-side images are close-ups of the tip apex.

3.4.2. Topography obtained with sharpened and cone-shaped tips

Figure 3.8 shows the topography of mica measured in the KCl solution with the two cantilevers. Using the quantitative relationship of the force and Δf, [6] the repulsive tip-surface force was estimated to be on the order of 0.1 nN during the feedback control of the imaging scan. The topography observed with the two tips shows equivalent honeycomb structures with hexagons of 0.5 nm. The honeycomb structure observed agreed with an earlier report. [18] Note that subnanometer resolution was achieved with the cone-shaped LHCR tip. The topographic resolution and contrast of mica was insensitive to the shape of the two tips. It was difficult to deduce a possible contribution of long-range force to the topography observed with the cone-shaped tip.

Subnanometer resolution was also achieved on a soft, organic surface using the two tips. Figure 3.9 shows the topography of the dodecanethiol SAM in hexadecane. Protrusions appeared with a hexagonal arrangement of 0.5 nm spacing and are assigned to the methyl head groups of the ($\sqrt{3}\times\sqrt{3}$)-ordered thiol monolayer. Detail discussion on the structure of dodecanethiol SAM is described in Chapter 4. Here the author focused on the fact that the sub-nanometer resolution topography was acquired.

Subnanometer resolution was achieved regardless of macroscopic shape of the tip. The topography obtained with AFM is generally a convolution of the surface corrugation and tip. The subnanometer resolution thus suggests a subnanometer-sized apex present on both the sharpened and cone-shaped tips. This suggestion is in line with the minitip assumption frequently assumed in scanning probe microscopy. Protrusions may be naturally present on a tip body. One such protrusion, which is closest to the surface, exclusively receives the short-ranged repulsive force response from the surface in atomic force microscopy. [19-22]

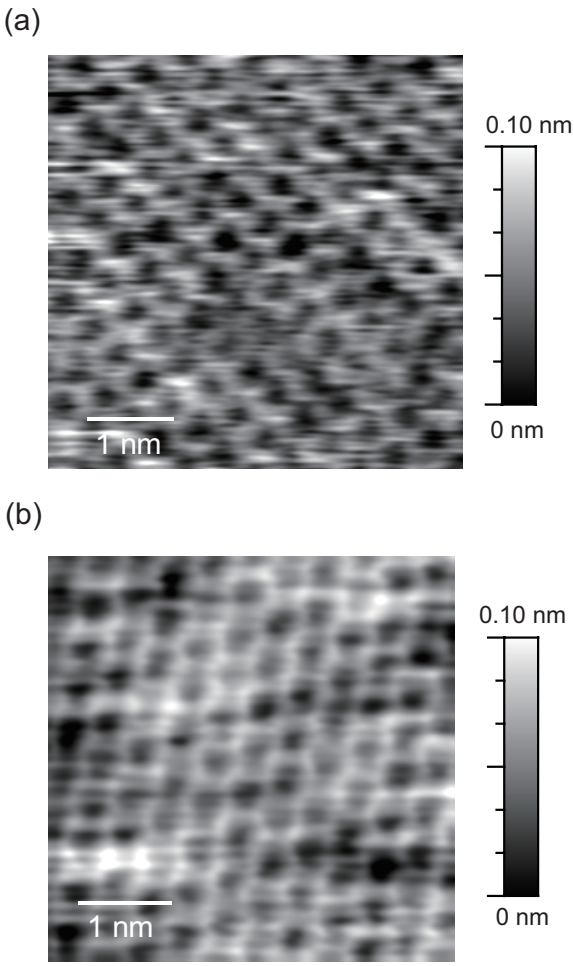

Figure. 3.8. Topography of mica in the 1 M KCl aqueous solution using (a) the sharpened and (b) the cone-shaped tip. Oscillation amplitude: 0.2 nm. Frequency shift: (a) +350 Hz and (b) + 300 Hz.

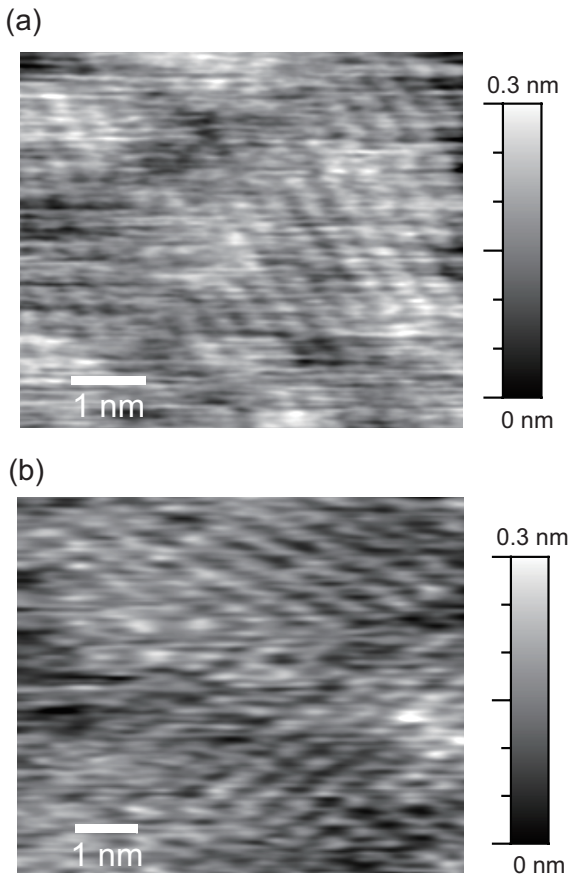

Figure. 3.8. Topography of the dodecanethiol SAM in hexadecane using (a) the sharpened and (b) the cone-shaped tip. Oscillation amplitude: 0.2 nm. Frequency shift: (a) +1300 Hz and (b) + 800 Hz.

3.4.3. Force curves obtained with sharpened and cone-shaped tips

Force-distance curves were measured at the hexadecane-thiol SAM interface using the two cantilevers. The oscillating cantilever was scanned vertically from the liquid to the surface until Δf exceeded a threshold, +1000 Hz to avoid the tip tapping the surface. Liquid hexadecane structured on the thiol monolayer presented an uneven Δf distribution as a function of the vertical distance from the surface. The Δf distribution was, on the other hand, homogenous along lateral coordinates. The detail discussion of laterally homogenous distribution is described in Chapter 4. Here the author focuses on the feature of individual Δf-distance curves. Fifty Δf-distance curves were observed in scan-shift cycles and summed to obtain an averaged curve. The water-mica interface was not favorable for averaging, since the interfacial water was laterally structured to give heterogeneous Δf curves along lateral coordinates. [2,3] The Δf curves in hexadecane were converted to force-distance curves and then averaged. The nominal spring constants provided by the suppliers were used in the conversion. Detailed insight on applied force was gained by quantitatively comparing the averaged curves.

Figure 3.10 shows force-distance curves obtained with the sharpened and cone-shaped tips. The horizontal axis of the figure represents relative tip-surface distance, as the two curves were adjusted at the second local maximum. Three local maxima were identified on each of the two curves, with the same peak-to-peak distances and modulation amplitude. The force acting in the nano-sized particle has been widely analyzed by the Derjaguin approximation on condition that all the interaction is additive. [23] This approximation relates the radius of two spheres (R_1, R_2) to the total force strength (F) as:

$$\begin{aligned} F(z) &= \int_z^{\infty} 2\pi\left(\frac{R_1R_2}{R_1+R_2}\right) f\left[z+\frac{x^2}{2}\left(\frac{1}{R_1}+\frac{1}{R_2}\right)\right]\left(\frac{1}{R_1}+\frac{1}{R_2}\right)xdx \\ &= 2\pi\left(\frac{R_1R_2}{R_1+R_2}\right)W(z) \end{aligned} \qquad (3.25).$$

Here, f is force field in a system and W is the interaction free energy between the particles. Suppose the system of a spherical tip near a flat surface, so that the one sphere can be regarded as very large sphere, $R_2 >> R_1$, the equation (3.25) can be deduced as,

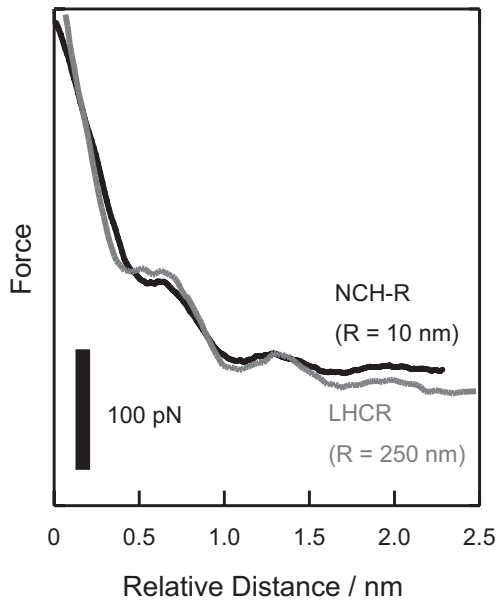

Figure 3.10. Averaged force-distance curves at the hexadecane-dodecanethiol SAM interface. The dark and gray curves were determined with the sharpened and cone-shaped tips, respectively. The curves are vertically shifted to overlap, to aid comparison. The origin of the relative distance is set to the distance at which *Δf* of the NCH-R cantilever exceeded the threshold of +1000 Hz.

$$F(z) = 2\pi R_1 W(z) \qquad (3.26).$$

This equation indicates that the total force is proportional to the radius of the tip body in a continuum liquid. The approximation works well with micrometer-sized colloidal tips. Lim *et al.* [24] pointed out that the modulation amplitude deviated from the prediction of the Derjaguin approximation when they used tips of 15-100 nm radius in organic solvents over graphite. If we applied the approximation to the two tips, the modulation amplitude would be larger by 25 times with the cone-shaped tip than with the sharpened tip. However the results show in Fig. 3.10 clearly deviated from the Derjaguin approximation. The measured force curves were totally insensitive to the tip body radius. This suggests that the effective area loading the force to surface and structured hexadecane is smaller than the nominal radius, less than 10 nm in this study. This is

consistent to the minitip assumption mentioned before, where the identical topography was obtained regardless of the tip body shape.

The author focused on the independent force modulations to macroscopic shape of the tips and considers again here the relationships between the force and the gradient of liquid density as suggested in 3.2. The thickness of the region occupied by layered hexadecane was 2 nm, as seen in Fig. 3.10. When the minitip closest to the surface penetrates that region, it receives force modulated by the structured hexadecane. Hexadecane density should be uniform outside of the 2-nm-thick layer. The rest of the tip body and entire cantilever are surrounded by hexadecane liquid of uniform density, as described in Fig. 3.4. The tip body cannot contribute to the amplitude of force modulations caused by the structured hexadecane. The dominant role of the short-range force only applied to the tip apex cause deviation of Derjaguin approximation. Mass point model of simple relationships (3.23) between force and density gradient is confirmed to be reasonable assumption for interpreting the force modulations as first approximation.

3.5. Fluctuating minitip

The effective area of the tip apex loading the force is estimated to be near the size of a small cluster of a few atoms. Individual minitips can diversify in terms of its size or chemical composition. In this section, the specificity of individual minitips is discussed from the fluctuation of the observed force modulation, as well as chemistry of the tip apex is argued from the topographic contrast of a chemically heterogeneous surface.

3.5.1. Fluctuating size of force loading area

The amplitude of force modulations fluctuated in scan-shift cycles to a limited extent. Figure 3.11(a) shows a cross-sectional presentation of Δf distributions over the hexadecane-thiol interface obtained with the cone-shaped tip. Positive (negative) Δf is shown to be bright (dark). The brightest region at the bottom represents the contour on which Δf exceeded the threshold. Three pairs of dark and bright layers appeared from the surface to the liquid, showing the uneven density distribution of structured

hexadecane. This layered feature was disturbed occasionally. One of disturbances appeared in the region marked by a broken line. The shape of force curves discontinuously fluctuated to a limited extent at the disturbance.

Force curves before and after the disturbance are compared in Fig. 3.11(b). Fifty curves in each of boxes (1) and (2) were averaged to produce curves (1) and (2). The two averaged curves presented the same peak-to-peak distances with different modulation amplitudes. The amplitude from the second minimum to second maximum was 18 pN in curve (1) and 13 pN in curve (2). The different amplitude should reflect the different effective area of the minitip. By accumulating similar events observed in repeated scans, the amplitude of the second minimum and second maximum was seen to fluctuate in the range of 10-30 pN. This range of force fluctuation is consistent with the minitip assumption, in which only a few atoms are exposed to the structured liquid. In an earlier study of water on $CaCO_3$ [25], attractive forces on the order of 10 pN acting between single atomic sites on the sample and the front atoms of the tip were measured.

The author considers here the extent of confinement caused by the minitip. When solid walls pinch a liquid, diffusion of liquid molecules is limited. The pressure applied by the walls also enhances the dense packing of the liquid molecules. These effects of confinement distinctly appear in SFA studies. [8] *n*-undecane presented layer-to-layer distances of 0.3-0.4 nm when confined by octadecyltriethoxysilane-covered mica wafers. [26] On the other hand, the force curves shown in Figs. 3.10 and 3.11 presented longer peak-to-peak distances of 0.6 nm. The longer distance should be resulted from less confinement. The two force curves in Fig. 3.11(b) exhibit the same peak-to-peak distances accompanied by different force amplitudes. The peak-to-peak distance insensitivity to the minitip size suggests that the minitip was not large enough to cause the confinement of hexadecane. The author concluded that the intrinsic structure of an open liquid-solid interface should be observable by atomic force microscopy with a 10-pN-order force sensitivity.

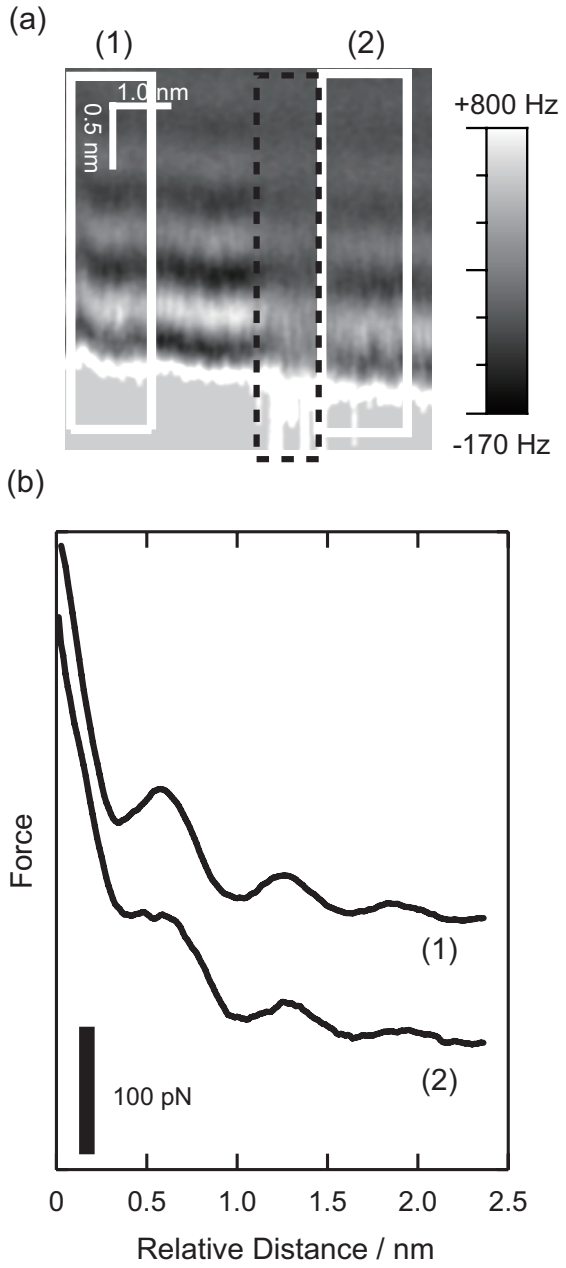

Figure 3.11. Force distribution on the hexadecane-thiol SAM interface observed with the cone-shaped tip. A cross-sectional Δf distribution is shown in (a). The disturbed region is marked with a broken line. Fifty force-distance curves accumulated in regions (1) and (2) were averaged and presented in (b). Each curve is laterally adjusted to each force maxima and staggered vertically for viewing ease. The origin of the relative distance is set to the distance at which Δf of curve (2) exceeded the threshold of +1000 Hz.

3.5.2. Fluctuating chemical composition of minitip

Topography

Fluctuation of force contrast owing to the minitip was also found on the adsorbed decanol layers over highly oriented pyrolytic graphite (HOPG). Chemical heterogeneity of the adsorbed decanol molecules should enhance the difference of chemical composition of tip apex. The contributions of chemical composition of the minitip to force contrast are discussed in this subsection.

Figure 3.12 presents a set of the topography of decanol/HOPG interface obtained using the advanced FM-AFM. Typical large-area image is presented in Fig. 3.12(a). The stripe structure of adsorbed decanols was found in the image. The separation of the strip was 2.6 nm. Earlier STM studies [27,28] showed that the decanol molecules were hydrogen-bonded with its hydroxyls and alkyl chains lie in side by side. The size of lamellar was found to be 2.65 nm in width in previous low-angle X-ray diffraction study. [29] The observed stripe separation was comparable to the lamellar width, and can therefore be assigned to the structure of decanol molecular adlayer over the HOPG.

The bright stripes were appeared with characteristic boundary of the lamella. The adjacent decanol lamella crossed each other with the angle of 120°. The domain orientation resulted from the epitaxial growing on the HOPG surface. [30]

The lamellae can resolve in sub-molecular features in the high-resolution image of (b) and (c). During the repeated experiments, two types of contrast were found at intra-lamella. One has double bright rows side by side of the lamella as shown in (b), the other has additionally the single bright row runs in the center of lamellae as shown in Fig. 3.12(c). Previous report of *in-situ* STM study [27] showed the dimerized arrangements of decanol which was a hydrogen bonded pair of two decanols with their alkyl chain extended straightly, bended at 120° with each chains. Such herringbone arrangements were commonly found in alcohols adlayer on HOPG. The lamella of dimerized decanols was calculated to be stable in the herringbone arrangement rather than the straight-line arrangement where the molecules were adjacent parallel with their chains. [28] From a calculation study [31], the terminal methyl groups of the alkyl chain were protruded onto the surface when the molecular adlayer takes the herringbone arrangement as shown in Fig. 3.12(d). The observed double rows appeared side by side

at the molecular lamella should be assigned to these protruded methyl groups.

The author assumes that the enhanced contrast at the center of the lamella as shown in Fig. 3.12(c) should be a consequence of the different chemical composition of tip apex, not the different intra structure of decanol lamellae. This is because the enhanced topographic contrast was observed to appear and disappear during the consecutive scans, although the setpoint of Δf and oscillation amplitude kept constant.

Tip apex is generally responsible for such sub-nanometer contrast as presented in the previous sections. One of the earlier STM observations give a clue to interpret the contrast enhancement. The 1-octadecanol layer physisorbed from 1-phenyl octane solution onto HOPG exhibited the similar contrast of single bright row by chemically modified gold tips. [32] They suggested that adsorption of contaminant should cause the enhanced contrast of the center of the molecular lamella. The enhanced contrast in their STM images arose due to the hydrogen-bond interaction between hydroxyl residues of the octadecanol lamellae and adsorbed molecules on the tip. The author considers that this argument can be applied in the case of the current AFM topography. In general, when achieved sub-nanometer resolution in topography, the strong tip-sample force is loaded at the near-contact region where the tunneling current is induced between tip and substrate. Also in this case, hydrogen-bond-capable end-groups probably induced onto the tip apex owing to adsorbed decanols or some organic contaminants. Such the induced end-groups may interact with the hydroxyl residues of the decanol lamella through hydrogen bond. The hydrogen bond caused to enhance the tip force onto such regions, which provided higher contrast of the topography. In addition, the contrast changes during the scan should be the result of the transmutative tip apex. The adsorbate onto the tip apex may be introduced and removed during the scan, which causes the observed contrast changes.

Here note that the mixed appearance of these contrasts, which contains the three identical bright rows, was also found as shown in Figure 3.13. The mixed appearance however, was found less frequent than the structures of Figs. 3.12 (b) and (c). This may be the case that the contribution of the hydrogen bond for the total imaging force was comparable to that of other interactions. A possible tip apex may be the cluster of hydrogen-bond-capable and incapable groups. The mixed contrast is supported the assumption that the contrast changes were due to fluctuations of the tip apex.

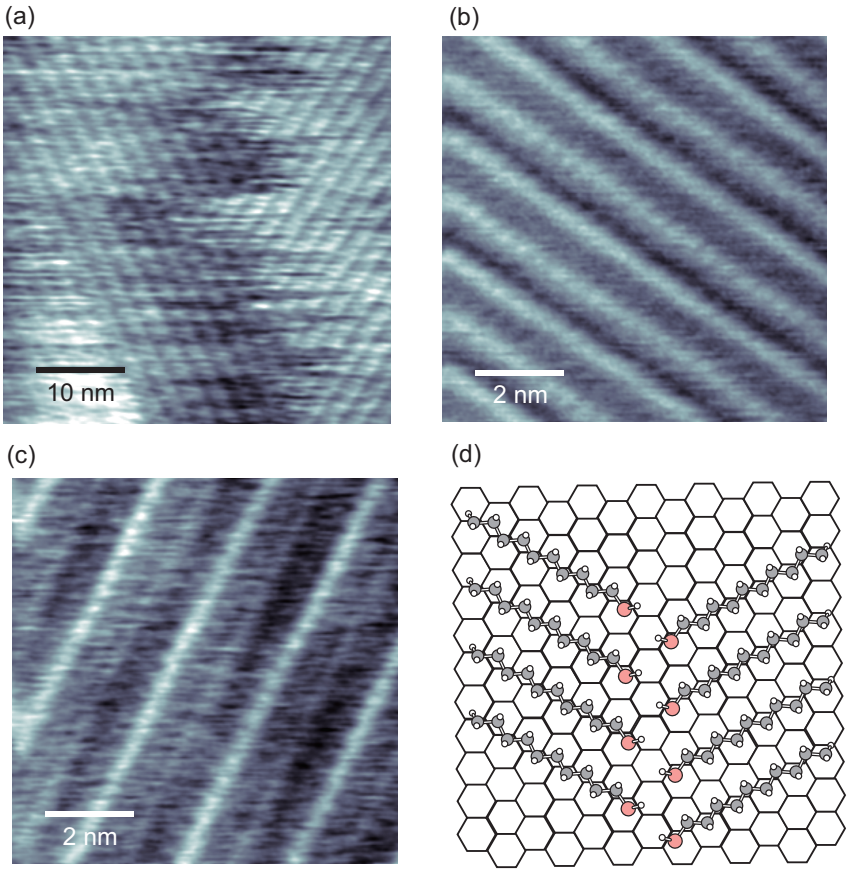

Figure 3.12. (a-c) Topography of adsorbed decanol onto HOPG. Amplitude 0.1 nm Frequency shift (a) +400 Hz, (b) +300 Hz, (c) +700Hz. (d) The suggested herringbone structure of the adsorbed decanol layer on HOPG drawn after ref. 33.

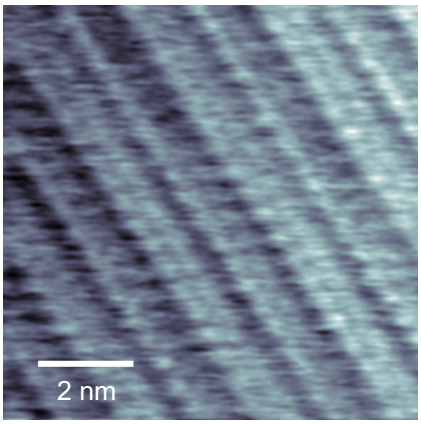

Figure 3.13. Topography of adsorbed decanol onto HOPG presented mixed contrast of Figs. 3.12(b) and (c). Amplitude 0.1 nm Frequency shift +400 Hz.

Δf distributions

The force contrast dependence on the chemical composition of minitip was also acknowledged on the cross-sectional *Δf* distributions.

Figure 3.14(a), (d) and (g) shows the cross-sectional *Δf* distributions over the decanol adsorbed layers soon after obtaining the topography of (b), (e) and (h). The *Δf*-distance curve also displayed in the panel (c), (f) and (i). Each curves is depicted where indicated by the arrows of corresponding color of the curves. Detail discussion of the force modulations was described in 5.7. Here the author focuses on the difference of the force contrast due to the tip apex, which attributed to the different contrast of the topography.

The *Δf* modulation due to the localized decanol was found on the *Δf*-distance curves. All tip apex present majorly the same tendency of *Δf* modulation. The amplitude of the modulation enhanced over molecular adsorption layer as seen in the green curves on each panels, (c), (f), and (i), but depressed at the grooves between molecular adsorption layer as seen in the yellow curves. The enhancement of *Δf* modulation is related to the enhancement of liquid density of decanol, which is related to the localization of the molecules. Such localized features of the solvated decanol molecules were probed insensitive to the tip apex.

On the other hand, the *Δf* distributions over the OH end-groups of the adsorbed decanols, that are shown in the blue curve on each panel, showed different oscillation magnitudes. The author assumes that the difference comes from the force enhancement due to the hydrogen bond onto such regions, as suggested in the mechanism of the enhanced topographic contrast. The OH group of the liquid decanol is expected to locate around the OH groups of the adsorbed decanols, because the orientation of the liquid decanol should be limited due to the hydrogen bond to the adsorbed decanol layers onto HOPG surface. Over the OH groups of the adsorbed decanols, the tip apex was affected by the hydrogen bond to OH group of localized liquid decanols, providing the enhanced oscillation of the force modulations.

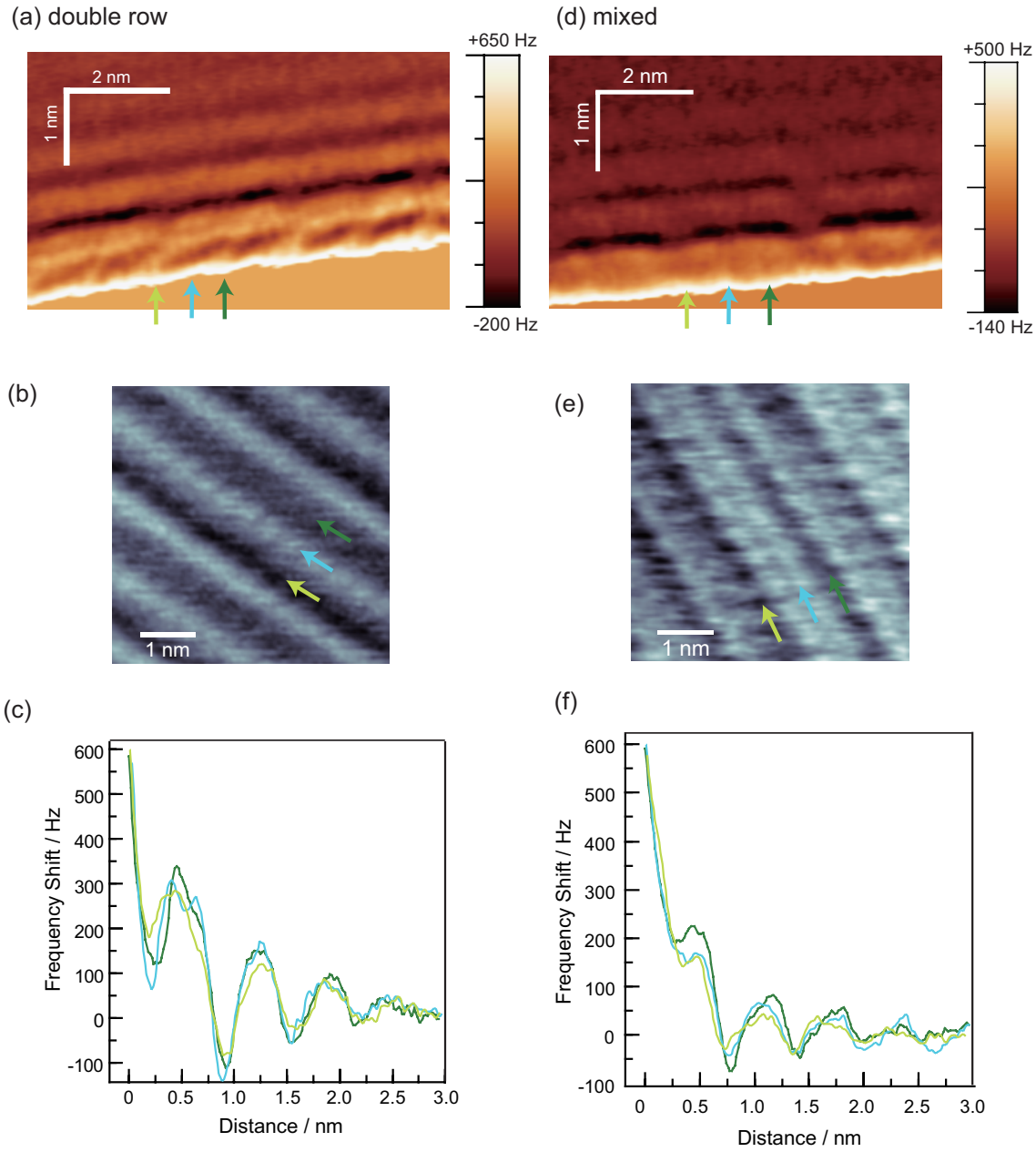

Figure 3.14. (Continued to next page) (a, d, g) Cross-sectional Δf distributions over the decanol adsorbed layers soon after obtaining the topography of (b, e, h). (c, f, i) The Δf-distance curves also displayed in the panel (c), (f) and (i). Each curves is depicted where indicated by the arrows of corresponding color to the curves. Amplitude 0.1 nm.

(g) one line

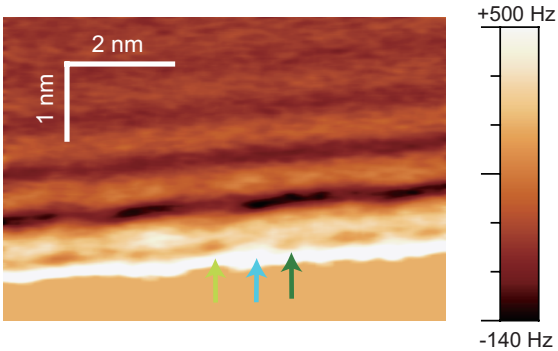
2 nm
1 nm
+500 Hz
-140 Hz

(h)

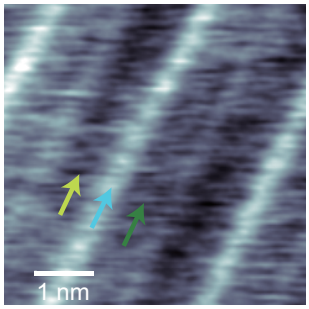
1 nm

(i)

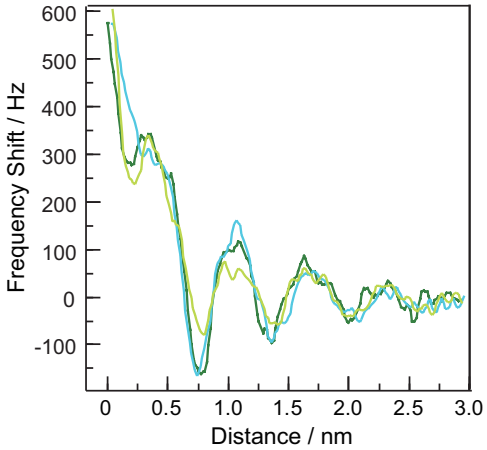
Frequency Shift / Hz
600
500
400
300
200
100
0
-100
0
0.5
1.0
1.5
2.0
2.5
3.0
Distance / nm

Chemical modification of the tip is a possible solution to interpret force contrast further. Takamatsu et al. [34] arranged a single-molecular tip with self-assembled azobenzene derivatives onto the tip body, to control the chemical composition of the tip apex with photoisomerization induced by light irradiation. Measurements in liquids using such a chemical controllable tip are desired to be demonstrated in near future, in order to estimate the contribution of chemical composition of tip apex to the applied force.

Note that the chemical heterogeneity of surface enhanced the contribution of tip chemistry. The topography of chemically uniform surfaces, such as OH-, COOH-, or CH_3-terminated thiolate self-assembled monolayers as discussed in the following chapters, was totally homogeneous even when the tip composition changed. Water and hydrocarbons that can be regarded as chemically uniform in liquid phase, are also unobservable of significant dependence on the tip chemistry in the force distributions. One of the latest studies of FM-AFM conducted by Kaggwa et al. also found the similar trend to the current findings. [35] They measured the force-distance curves at an interface of water/hydrophilic surface using chemically modified tips to arrange hydrophilic and hydrophobic surface. They indicated that the oscillatory force modulation due to the structured water was irrespective of the tip chemistry. In conclusion, chemical interaction should be needs to be taken into consideration in such a case that chemical heterogeneity of surface or liquid causes diversity of the interaction with the tip apex.

3.6. Conclusions

In this chapter, a promising ability of the highly sensitive AFM to probe the local structure of interfacial liquids is discussed. This study provided two successful example of force-distance curves at aqueous interfaces of α-Al_2O_3(01-12) and TiO_2(110) surface, which are comparable to theoretical or another experimental results of interfacial water structure. The force-distance curve contained local force oscillations accompanied with an exponentially decayed, electric double layer force. The force modulations were found to be related with the intrinsic density distributions of water molecules obtained by XCTR or MD simulation. The force distance curves further found to be laterally heterogeneous due to atomically heterogeneous structure of the surfaces. This suggested that the tip apex is possible to probe water-induced force modulations, to extract the local structure of interfacial liquids as suggested in recent studies. [2,3]

To demonstrate the role of tip apex, constant frequency-shift topography and force-distance curves were obtained on hexadecane-thiol SAM and water-mica interfaces using sharpened and cone-shaped tips. The topography of SAM and mica was obtained with subnanometer resolution regardless of the nominal radius of the tips. The amplitude of force modulation and layer-to-layer distances of the interfacial hexadecane were totally insensitive to the nominal tip radius. Insensitive topography and force-distance curves revealed that a minitip which is quite smaller than the nominal radius, 10 nm in this study, are present on the tip body and function as a force probe.

Dominant role of the tip apex enables to probe the local structure of interfacial liquid in both lateral and vertical coordinates in subnanometer scale. The presented experimental results convince us that the enhancement and depression of the liquid density, which shows the extent of localization of liquid molecules, can be probed by the AFM tip apex in the relative scale. The observed force distribution was successfully explained with supposing a minitip, as first approximation. However the more quantitative way to link AFM data to the structure of interfacial water is required in determining the absolute value of the density distribution. In the case of chemical heterogeneity of surface or liquid, specific chemical interaction toward the tip apex should also need to be taken into account. Collaborations of theoretical studies will help to complete the quantitative relationships, including quantitative estimation of contribution of an actual tip and real potential for the applied force.

References in Chapter 3

[1] T. Fukuma, M. Kimura, K. Kobayashi, K. Matsushige, and H. Yamada, *Rev. Sci. Instrum.* 76 (2005) 053704.

[2] K. Kimura, S. Ido, N. Oyabu, K. Kobayashi, Y. Hirata, T. Imai, and H. Yamada, *J. Chem. Phys.* 132 (2010) 194705.

[3] T. Fukuma, Y. Ueda, S. Yoshioka, and H. Asakawa, *Phys. Rev. Lett.* 104 (2010) 016101.

[4] M. Watkins, M. L. Berkowitz, and A. L. Shluger, *Phys. Chem. Chem. Phys.* 13 (2011) 12584.

[5] M. Harada and M. Tsukada, *Phys. Rev. B* 82 (2010) 035414.

[6] J. E. Sader and S. P. Jarvis, *Appl. Phys. Lett.* 84 (2004) 1801.

[7] M. Pedota, A. V. Bandura, P. T. Cummings, J. D. Kubicki, D. J. Wesolowski, A. A. Chialvo, and M. L. Machesky, *J. Phys. Chem. B* 108 (2004) 12049.

[8] J. N. Israelachvili, *Intermolecular and Surface Forces 3rd Ed.*, Academic Press, London, 2010.

[9] H.-J. Butt, *Nanotechnology* 3 (1992) 60.

[10] H.-J. Butt, M. Jaschke, and W. Ducker, *Bioelectrochem. Bioenerg.* 38 (1995) 191.

[11] W. A. Ducker, T. J. Senden, and R. M. Pashley, *Langmuir* 8 (1992) 1831.

[12] J. P. Fitts, X. Shang, G. W. Flynn, T. F. Heinz, and K. B. Eisenthal, *J. Phys. Chem. B* 109 (2005) 7981.

[13] G. F. Franks and L. Meagher, *Colloids and Surfaces A* 214 (2003) 99.

[14] J. V. Walther, *Am. J. Sci.* 296 (1996) 693.

[15] J. Guo, D. E. Ellis, and D. J. Lam, *Phys. Rev. B* 45 (1992) 13647.

[16] W. A. Ducker, Z. Xu, D. R. Clarke, and J. N. Israelachivili, *J. Am. Ceram. Soc.* 77 (1994) 437.

[17] J. G. Catalano, C. Park, Z. Zhang, and P. Fenter, *Langmuir* 22 (2006) 4668.

[18] T. Fukuma, K. Kobayashi, K. Matsushige, and H. Yamada, *Appl. Phys. Lett.* 86 (2005) 193108.

[19] F. J. Giessibl, *Science* 267 (1995) 68.

[20] R. Pérez, I. Štich, M. C. Payne, and K. Terakura, *Phys. Rev. B* 58 (1998) 10835.

[21] S. Morita and Y. Sugawara, *Appl. Surf. Sci.* 140 (1999) 406.

[22] K. Tagami and M. Tsukada, *Jpn. J. Appl. Phys.* 39 (2000) 6025.

[23] B. V. Derjaguin, *Kolloid Z.* 69 (1934) 155.

[24] L. T. W. Lim, A. T. S. Wee, and S. J. O'Shea, *Langmuir* 24 (2008) 2271.

[25] F. Ohnesorge and G. Binnig, *Science* 260 (1993) 1451.

[26] J. Peanasky, H. M. Schneider, S. Granick, and C. R. Kesse, *Langmuir* 11 (1995) 953.

[27] G. C. McGonigal, R. H. Bernhardt, Y. H. Yeo, and D. J. Thomson, *J. Vac. Sci. Technol. B* 9 (1991) 1107.

[28] X. Miao, C. Chen, J. Zhou, and W. Deng, *Appl. Surf. Sci.* 256 (2010) 4647.

[29] K. Morishige, Y. Takami, and Y. Yokota, *Phys. Rev. B.* 48 (1993) 8277.

[30] B. Venkataraman, J. J. Breen, and G. W. Flynn, *J. Phys. Chem.* 99 (1995) 6608.

[31] T. Yang, S. Berber, J.-F. Liu, G. P. Miller, and D. Tománek, *J. Chem. Phys.* 128 (2008) 124709

[32] T. Ito, P. Bühlmann, and Y. Umezawa, *Anal. Chem.* 70 (1998) 255.

[33] S. Yin, C. Wang, Q. Xu, S. Lei, L. Wan, and C. Bai, *Chem. Phys. Lett.* 348 (2001) 321.

[34] D. Takamatsu, Y. Yamakoshi, and K. Fukui, *J. Phys. Chem. B* 110 (2006) 1968.

[35] G. B. Kaggwa, P. C. Nalam, J. I. Kilpatrick, N. D. Spencer, and S. P. Jarvis, *Langmuir* 28 (2012) 6589.

Chapter 4: Interfacial Structure of Liquid Hydrocarbons at Inert Interfaces

4.1 Introduction

4.1.1 Interfacial structure of liquid on inert interface

As reviewed in Chapter 1, structures of liquids at solid-liquid interface are important consequences in wide range of phenomena in chemistry, biochemistry and material sciences. Interfacial structure is thought to reflect various physical and chemical properties of solid surface and liquid. In this chapter, the effect of geometric configuration of liquid molecules themselves is discussed for structuring over solid surfaces. In order to isolate such steric contribution, the interfacial structures of liquid hydrocarbons facing a well-defined, CH_3-terminated self-assembled monolayer (SAM) were investigated, where was no specific chemical interaction, and just with van der Waals interactions. This is a model interface where steric configuration of liquid molecules expected to dominantly attribute the interfacial structure.

The interfacial structures of liquids are discussed by the two-dimensional, cross-sectional distribution in various hydrocarbons over dodecanethiol SAM. Steric effect of the interfacial liquid structure is discussed by comparing the cross-sectional distribution in *n*-dodecane, *n*-hexadecane and 1-phenyloctane. Those possess common chemical properties as hydrocarbons but with different chain lengths and different molecular volumes.

4.1.2 Introduction to self-assembled monolayers

Here the author briefly reviews the model substrate used in this study, self-assembled monolayer (SAM). In analytical studies of nanoscience and nanotechnology such as scanning probe and electron microscopy, SAMs have been a remarkable tool for observing and manipulating atomic- or molecular-scale objects. SAMs provide a convenient, flexible, well-defined system with which to tailor the surface or interfacial properties. SAMs are typically organic molecular assemblies formed by the adsorption of the molecule from solution or the gas phase onto the solid surface such as metals, metal oxides, or semiconductors. The organic adsorbates spontaneously and often epitaxially construct a crystalline structure. A specific affinity for a solid substrate is driven to the structuring. There are number of functional groups that bind to the specific metals, metal oxides, or semiconductors. The most extensively investigated class of SAMs is derived from the adsorption of alkanethiols on gold [1-9], silver [10,11], copper [12], palladium [13], platinum [14], and mercury [15]. The considerable affinity of thiols for the metal substrates makes it possible to generate well-defined surfaces. Using a chemical functionality of another end-group of the thiol molecules, useful and highly alterable chemical functionality can display onto the surface. (Figure. 4.1)

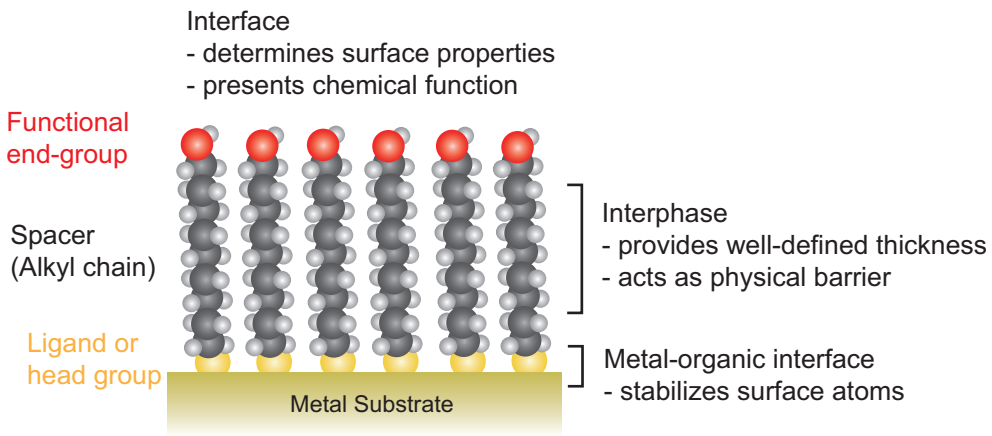

Figure 4.1. Scheme of a self-assembled monolayer of alkanethiolates supported on a gold substrates.

Nanostructures of alkanethiolate SAMs are well-suited for studies in nanoscience and nanotechnology. One of the reasons of their suitability is that they are easy to prepare, especially no needs to ultra high vacuum (UHV) condition or other specialized instruments. The major approach of forming the monolayers is dipping treatment of the substrates in the solution of the organic molecules for assembling. Since the SAM forms owing to strong interactions such as metal-thiolate chemical bonding, the resulting layers are thermodynamically stable and mechanically robust. Thus SAMs are stable enough to perform subnanometer-scale analysis with scanning probe techniques.

4.2 Experiment

Thiolate SAMs were prepared on vacuum-deposited, 150-nm thick gold films. Cleaved mica wafers were annealed at 723 K in a vacuum of 10^{-5} Pa and exposed to a custom-designed chamber (Sensor and Works, Japan). Dodecanethiol monolayers were self-assembled on the gold film. The gold-coated wafers were immersed in a 1 mM ethanol solution of 1-dodecanethiol (Wako, >98%) for 24 hours, rinsed with pure ethanol, and immersed in the liquid hydrocarbon: *n*-dodecane (Wako, >99%), *n*-hexadecane (Wako, >97%) or 1-phenyloctane (Junsei, >98%).

The microscope was a Shimadzu SPM 9600 modified with a low noise optical deflection sensor [16] described in Chapter 2. Multi-mode laser operation in the sensor reduced the noise of cantilever deflection to as low as 20 fm $Hz^{-1/2}$, near the theoretical limit. Silicon cantilevers (Nanosensors, NCH-R) with a nominal spring constant of 40 N m^{-1} were resonantly oscillated at 130-150 kHz with quality factors (Q) of 5 in the hydrocarbons. To stabilize a self-oscillation loop in the low-Q environments, bandpass filters (Q = 20) were inserted in the loop for oscillation amplitude regulation.

Topography was obtained with regulation of the tip-surface distance to keep the Δf constant. Imaging scans to make topographic images were done with 256×256 pixels. Cross-sectional Δf distributions to the surface were acquired as described in section 2.5. One Δf-distance curve contained 200-220 pixels. The scan frequency was typically 25 Hz and the acquisition time was 10 s per frame. All the experiments were performed at room temperature.

4.3. Topography of dodecanethiol monolayer in n-dodecane

The author started by observing the topography of the dodecanethiol SAM. Figure 4.2 presents the constant frequency-shift topography observed in *n*-dodecane. Islands of the gold substrate epitaxially grown on mica provided atomically flat terraces 200-300 nm wide with small pits, as shown in Fig. 4.2(a). The pits were typically 10 nm in diameter and 0.3 nm in depth. These are strong evidence of thiol absorption. Those pits are known to be created by gold atom extraction and incorporation to sulfur–gold bonds [17]. Gold adatoms are removed from the terrace associated with thiolate self-assembly. The following reconstruction of gold surface causes to generate these pits [18]. Some contaminants were additionally identified as bumps larger than 5 nm in the lateral dimension, which are not a trivial issue for scanning topography and Δf distribution in the narrow area.

Periodic protrusions were apparent in a zoomed image of Fig. 4.2(b). The protrusions exhibited a hexagonal arrangement with spacing of 0.5 nm. Previous AFM [19] and electron diffraction [20,21] studies revealed that alkanethiol molecules are densely packed on Au(111) to present a $(\sqrt{3}\times\sqrt{3})R30°$ long-range order as illustrated in Fig. 4.2(c). Based on these results, we assigned the protrusions to the individual methyl groups of the dodecanethiol monolayer. *n*-Dodecane was not inserted into the dodecanethiol monolayer, though the two compounds are analogues. The intrinsic $\sqrt{3}\times\sqrt{3}$ structure of the SAM was also stable in the other two hydrocarbons.

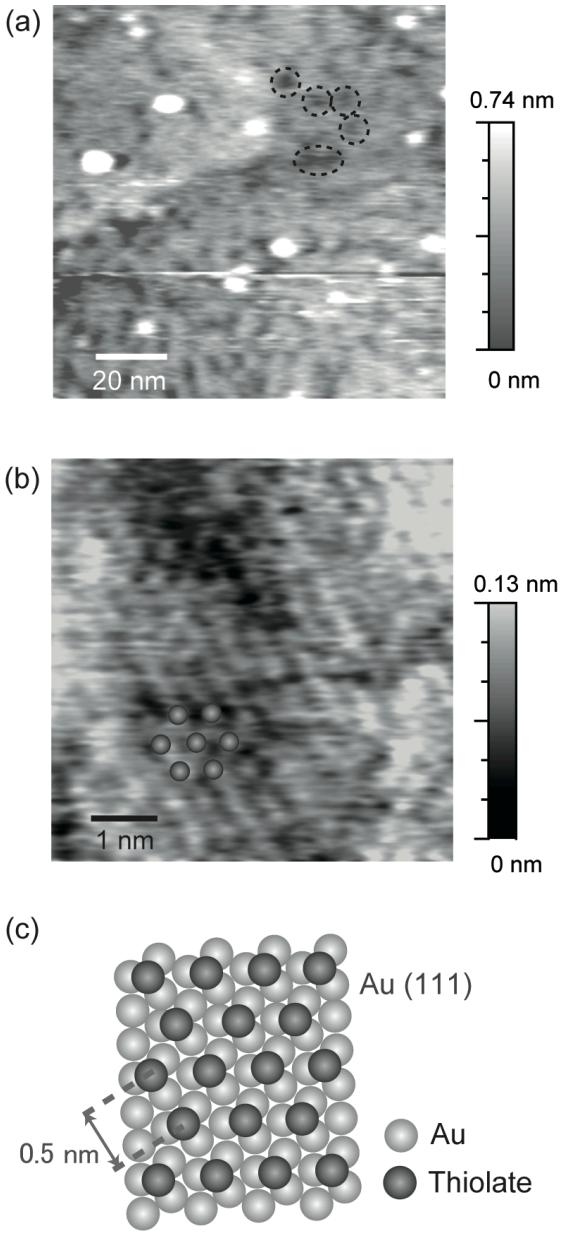

Figure 4.2. Constant frequency-shift topography of the dodecanethiol monolayer observed in *n*-dodecane. Some of pits are marked with dotted circles. Spheres are superimposed to show protrusions. Amplitude of cantilever oscillation: 0.2 nm, frequency shift: +1100 Hz, image size: (a) 100 nm square and (b) 8 nm square. (c) An illustration of the $\sqrt{3}\times\sqrt{3}$ structure of thiols on Au(111).

4.4. Interfacial structure of liquid hydrocarbons over dodecanethiol SAM

4.4.1. Structure of hexadecane liquid

In order to determine the interfacial structure of liquid hydrocarbons, the two-dimensional Δf distribution was observed as a function of vertical and lateral coordinates over the monolayer shown in Fig. 4.2. The AFM tip was scanned vertically from the liquid to the surface until Δf exceeded a threshold (+1000 Hz). The threshold was set in order to prevent the tip damaging the monolayer. The thermally induced drift of the cantilever was in the order of 0.1 nm min^{-1} relative to the surface. The acquisition time of a two-dimensional distribution was typically 10 s and drift-induced distortions were not serious.

Figure 4.3(a) shows a typical Δf distribution cross-sectional to the surface. Positive (negative) Δf is shown to be bright (dark). A brightest region appeared in the bottom of the Δf distribution. When the tip went down into that region, Δf increased monotonously. This is a sign of near-contact of the tip to the thiolate monolayer. The topography of the brightest region thus represents the physical topography of the monolayer terminated with CH_3 end-groups. A contour line, on which Δf exceeded +900 Hz, was superimposed on the distribution, to trace the topography of the brightest region. Periodic protrusions found on the contour line represented individual CH_3 end-groups aligned on the $\sqrt{3}$ order. The protrusion-to-protrusion distance was 0.5 nm in Fig. 4.3(a) and consistent to the cell size of the long-range order confirmed in Fig. 4.2(b). The distance of 0.5 nm suggested that the imaging plane of Fig. 4.3(a) was parallel to the line connecting nearest neighbour thiolates.

Three pairs of dark and bright layers were identified in liquid hexadecane over the monolayer, showing an uneven density distribution of hexadecane as a function of the vertical distance from the surface. Vertical spacings between adjacent bright layers were 0.5-0.6 nm. This indicates that the density distribution of hexadecane was modulated with this periodicity, being consistent with a molecular dynamics simulation. Srivastava et al. [22] predicted that hexadecane molecules prefer to lie on an alkanethiol monolayer and present a layered liquid. According to Fig. 9 of ref. 22, the layer-to-layer spacing of the structured hexadecane was 0.5 nm.

The strength of the layered Δf distribution was even along the lateral coordinate. *n*-dodecane and phenyloctane also presented vertically uneven and laterally even Δf distributions over the thiolate monolayer. The laterally even strength distribution of the alkanes contrasts to the site-specific distribution of water observed over hydrophilic surface of the metal oxides in Chapter 3. On the hydrophilic oxide surfaces, interfacial water was involved in hydrogen-bond networks induced by surface OH groups to produce laterally uneven distributions. The even distribution of the alkanes is thus interpreted by the absence of any functional groups that produce specific interactions with the thiolate monolayer. This is consistent with the basic picture of the interface from statistical-mechanical approach.

Note that the thermal drift of the tip and substrate gives little influence on the laterally even distribution. If the lateral structure of the layered liquid was averaged out by the drift of the tip, the topography of the surface should also be averaged out. This was not the case in the result of Fig. 4.3(a). The layered hexadecane presented the Δf distribution of an even strength along the lateral coordinate, whereas periodic corrugations appeared on the topographic trace of the surface.

Figure 4.3(b) depicts a set of Δf-distance curves obtained in hexadecane. The two curves were recorded on a common lateral coordinate with the tip approaching or retracting the surface. The forward and backward Δf-distance curves were identical with no sign of hysteresis. Using the formulated relationship of Δf to the conservative force developed by Sader and Jarvis [23], the forward Δf-distance curve was converted to a force-distance curve according to their formula and shown in Fig. 4.3(c). The amplitude of force modulation was 20 pN from first minimum to first maximum in the force-distance curve. Force modulation amplitudes reported in early AFM studies [24-26] were in the order of 1 nN. The small force amplitude and the sub-nanometer resolution achieved in Fig. 4.2(b) and Fig. 4.3(a) to identify the individual end-groups of the thiolates, are consistent with the suggested small effective area of the tip apex in Chapter 3.

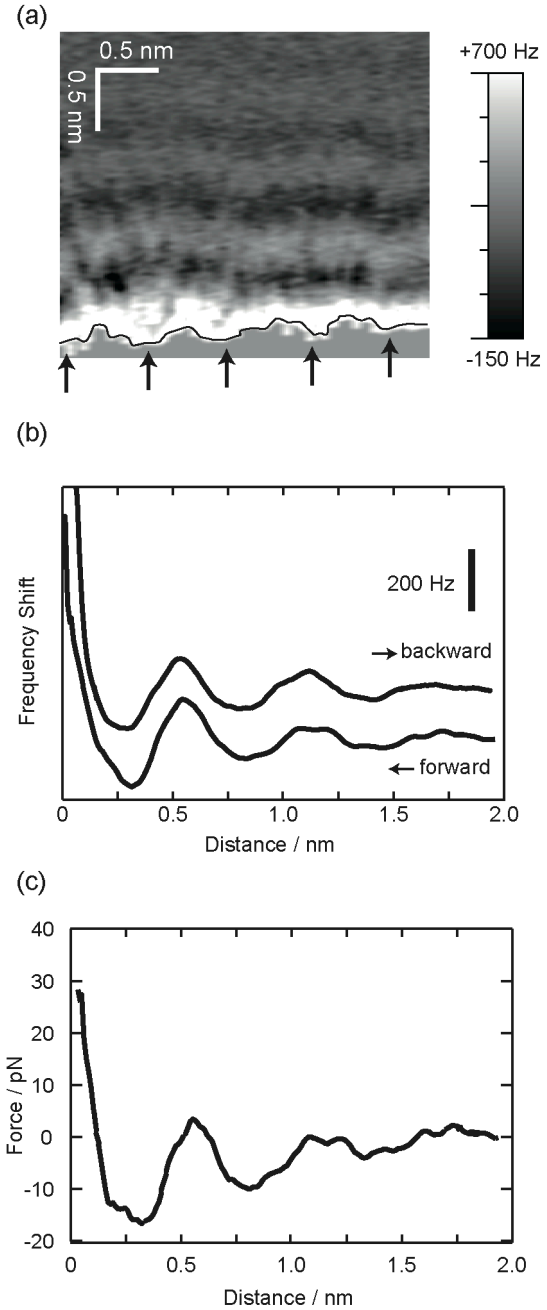

Figure 4.3. Interfacial *n*-hexadecane over the dodecanethiol monolayer. (a) A two-dimensional Δf distribution observed with a cantilever oscillation amplitude of 0.1 nm. The dark line shows a contour line on which the frequency shift exceeded +900 Hz. Arrows indicate periodic trenches of the contour line. (b) A set of frequency shift-distance curves obtained with the tip approaching and leaving the monolayer. Each curve was determined in a single forward or backward scan. (c) The force-distance curve converted from the forward Δf-distance curve in (b).

The threshold of +1000 Hz was needed to complete full Δf curves. With smaller thresholds, vertical scans sometimes aborted at local Δf maxima caused by the layered liquid. The strength of repulsive tip-surface force was estimated to be 30 pN at the threshold. The tip driven by force of this strength did not damage the monolayer, as evidenced by the reproducible Δf curves observed with the forward and backward scans.

In aqueous electrolyte solutions, force modulations were found with the electric double layer force monotonously decaying as a function of the vertical distance. The alkane liquids examined in this study were free from electrolyte and the author expected the absence of the double layer force. The force-distance curve in Fig. 4.3(c) showed a flat background with no sign of a monotonously decaying force. The short-range repulsive force of the background appearing at distances less than 0.2 nm and the attractive force appeared within 0.2 - 1.5 nm, is ascribed to van der Waals force between the monolayer and tip.

4.4.2. Layer-to-layer distances of different hydrocarbons

In this subsection, the author considers what determined the layer-to-layer spacing of structured liquids. For this purpose averaged Δf-distance curves were determined with *n*-dodecane and 1-phenyloctane. Those two compounds, along with *n*-hexadecane, possess common chemical properties to hydrocarbons but with different chain lengths and different molecular volumes. As the distribution of Fig. 4.3(a) observed in hexadecane, dodecane and phenyloctane presented layered distributions with enhanced Δf as a function of the vertical coordinate. Since the lateral distributions of the enhanced layers were even, fifty Δf-distance curves were recorded at different lateral positions and were simply averaged. Figure 4.4 shows the averaged Δf-distance curves in the three hydrocarbons. The curves are laterally shifted to adjust the first local maximum of each curve to be the origin of relative distance, the horizontal axis.

The peak-to-peak spacing of the averaged curves was sensitive to the composition of the hydrocarbons. First-to-second and second-to-third peak spacings are listed in Table 4.1. Dodecane and hexadecane had a common spacing of 0.56-0.58 nm, independent to the different chain lengths. Spacings with phenyloctane were 0.63-0.66

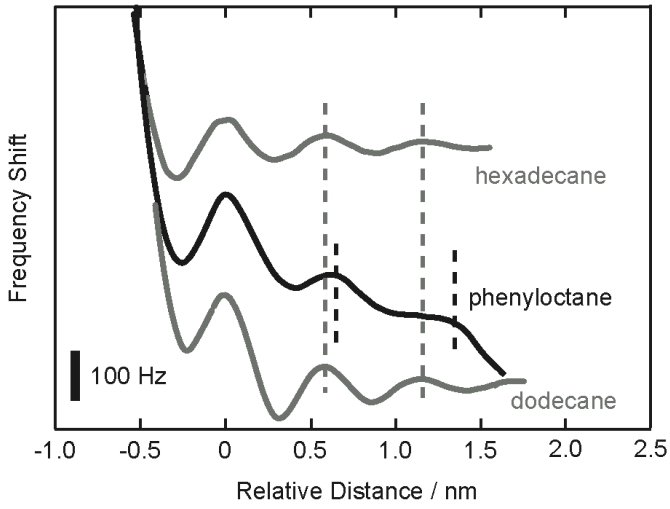

Figure 4.4. Averaged *Δf*-distance curves in *n*-hexadecane, 1-phenyloctane, and *n*-dodecane. The three curves are laterally shifted to adjust each first local maximum to be the origin of the horizontal axis. Broken lines show second and third local maxima. Vertical offsets are added for illustration.

Table 4.1. Peak-to-peak spacings on the averaged *Δf*-distance curves. The numbers in parentheses present the minimum and maximum spacings observed on individual, non-averaged curves.

Solvent	Average Spacing / nm	
	1st to 2nd	2nd to 3rd
Hexadecane	0.57 (0.55-0.59)	0.56 (0.53-0.60)
Phenyloctane	0.63 (0.61-0.69)	0.66 (0.60-0.72)
Dodecane	0.58 (0.55-0.59)	0.57 (0.53-0.59)

nm, clearly larger than those for the *n*-alkanes. The common spacing of the *n*-alkanes suggest favorable orientations with the molecular axis parallel to the surface, even though the SAM orientation is normal to the surface. This is consistent with a molecular dynamics simulation [22] and reasonable, because the structure of the *n*-alkane liquid should be dominated by van der Waals forces. The number of atoms in contact with the solid is maximized per molecule by parallel orientation. The van der Waals energy gain is thus optimized. This is also the case with *n*-alkanes in the second liquid layer being in contact with the first. In phenyloctane, the phenyl end-group is rigid and free to twist around the C_6H_5-C_8H_{17} single bond. The twisting end-group does not allow the whole molecule to be in contact with an object. The stacking capability is thus low with phenyloctane, and the peak-to-peak spacings are large.

The layer-to-layer spacing insensitive to the chain length of *n*-alkanes was found in an SFA study [27]. *n*-alkanes with different chain lengths presented nominal spacing of 0.4-0.5 nm. Larger spacing of 0.56-0.58 nm was observed with the two *n*-alkanes in the current study. The difference between SFA-based and FM-AFM-based spacing suggests different manners of packing liquid alkanes. Alkane molecules are confined in two walls of SFA, while they are less confined between the surface and AFM tip. Another difference between SFA-based and FM-AFM-based results is in the force modulation strength of less symmetric alkanes. 2-methyloctadecane [28] and cyclohexane [29] presented weak force modulations with SFA compared to those of *n*-alkanes. Our AFM results showed the comparative strength of force modulations with phenyloctane and the two *n*-alkanes. This difference can also be ascribed to the different extent of confinement in SFA and AFM, as pointed out by O'Shea and co-workers [25].

Interfacial *n*-hexadecane was examined in an early AFM study over graphite [30] and thiolate monolayer [31]. Hexadecane was structured to form layers on the substrates and tip jumps appeared from one layer to another. Jump distances, which should correspond to layer-to-layer spacings, were 0.45-0.50 nm. The vertical force distribution in squalane (2,6,11,15-tetramethylhexadecane) was also observed on graphite [32] to exhibit a layer-to-layer distance of 0.58 nm. Squalane, a methyl-substituted bulky alkane, caused a large distance. The current results obtained on the CH_3-terminated molecular monolayer showed a similar relationship of molecular structure and layer distance of liquid alkanes.

4.5 Conclusions

In this chapter, topography and cross-sectional Δf distribution were obtained at the inert interface of liquid hydrocarbons and dodecanethiol SAM. Topographic protrusions of individual CH_3 groups of the thiolates were identified and the ($\sqrt{3}\times\sqrt{3}$) long-range order of a dodecanethiol self-assembled monolayer remained intact in *n*-hexadecane, *n*-dodecane, and 1-phenyloctane.

The three liquid hydrocarbons were structured on the monolayer to present uneven density distributions as a function of distance from the monolayer. On the other hand, the density distribution of the hydrocarbons was even along lateral coordinates over the monolayer. The even distribution of the alkanes was interpreted by the absence of any functional groups that produce specific chemical interactions with the thiolate monolayer.

The layer-to-layer spacings were insensitive to the alkyl chain length, suggesting that the *n*-alkanes were oriented with their molecular axis parallel to the surface. A larger distance was observed with phenyloctane, which was ascribed to the large excluded volume of the phenyl group. The two *n*-alkanes lie on the monolayer to present common distances of 0.56-0.58 nm, whereas phenyloctane exhibited a larger distance of 0.63-0.66 nm, affected by the phenyl end-group. Layered hexadecane liquid was found in early AFM studies. Those studies were focused on the structure along the vertical direction. The current study revealed the cross-sectional structure as a function of vertical *and* lateral coordinates. The bulky feature of liquid molecule themselves provided significant contribution for their structuring at an inert interface.

References in Chapter 4

[1] G. E. Plirier, and E. D. Pylant, *Science* 272 (1996) 1145.

[2] R. G. Nuzzo, and D. L. Allara, *J. Am. Chem. Soc.* 105 (1983) 4481.

[3] M. D. Porter, T. B. Bright, D. L. Allara, and C. E. D. Chidsey, *J. Am. Chem. Soc.* 109 (1987) 3559.

[4] L. H. Dubois and R. G. Nuzzo, *Annu. Rev. Phys. Chem.* 43 (1992) 437.

[5] C. D. Bain, J. Evall, and G. M. Whitesides, *J. Am. Chem. Soc.* 111 (1989) 7155.

[6] C. D. Bain and G. M. Whitesides, *Science* 240 (1988) 62.

[7] H. A. Biebuyck, C. D. Bain, and G. M. Whitesides, *Langmuir* 10 (1994) 1825.

[8] P. E. Laibinis, G. M. Whitesides, D. L. Allara, Y. T. Tao, A. N. Parikh, and R. G. Nuzzo, *J. Am. Chem. Soc.* 113 (1991) 7152.

[9] L. H. Dubois, B. R. Zegarski, and R. G. Nuzzo, *J. Chem. Phys.* 98 (1993) 678.

[10] M. M. Walczak, C. Chung, S. M. Stole, C. A. Widrig, M. D. Porter, *J. Am. Chem. Soc.* 113 (1991) 2370.

[11] P. Fenter, P. Eisenberger, J. Li, N. Camillone III, S. Bernasek, G. Scoles, T. A. Ramanarayanan, and K. S. Liang, *Langmuir* 7 (1991) 2013.

[12] J. C. Love, D. B. Wolfe, R. Haasch, M. L. Chabinyc, K. E. Paul, G. M. Whitesides, and R. G. Nuzzo, *J. Am. Chem. Soc.* 125 (2003) 2597.

[13] A. Carvalho, M. Geissler, H. Schmid, B. Micel, and E. Delamarche, *Langmuir* 18 (2002) 2406.

[14] Z. Li, S.-C. Chang, and R. S. Williams, *Langmuir* 19 (2003) 6744.

[15] N. Muskal, I. Turyan, and D. J. Mandler, *J. Electroanal. Chem.* 409 (1996) 131.

[16] T. Fukuma, M. Kimura, K. Kobayashi, K. Matsushige, and H. Yamada, *Rev. Sci. Instrum.* 76 (2005) 053704.

[17] P. Maksymovych, O. Voznyy, D. B. Dougherty, D. C. Sorescu, and J. T. Yates Jr., *Prog. Surf. Sci.* 85 (2010) 206.

[18] J. Zhang, Q. Chi, and J. Ulstrup, *Langmuir* 22 (2006) 6203.

[19] C. A. Alves, E. L. Smith, and M. D. Porter, *J. Am. Chem. Soc.* 114 (1992) 1222.

[20] L. Strong and G. M. Whitesides, *Langmuir* 4 (1988) 546.

[21] C. E. D. Chidsey and D. M. Loiacono, *Langmuir* 6 (1990) 682.

[22] P. Srivastava, W. G. Chapman, and P. E. Laibinis, *Langmuir* 2 (2005) 12171.

[23] J. E. Sader and S. P. Jarvis, *Appl. Phys. Lett.* 84 (2004) 1801.

[24] H.-J. Butt, B. Cappella, and M. Kappl, *Surf. Sci. Rept.* 59 (2005) 1.

[25] S. J. O'Shea, N. N. Gosvami, L. T. W. Lim, and W. Hofbauer, *Jpn. J. Appl. Phys.* 49 (2010) 08LA01.

[26] R. Hayes, G. G. Warr, and R. Atkin, *Phys. Chem. Chem. Phys.* 12 (2010) 1709.

[27] H. K. Christenson, D. W. R. Gruen, R. G. Horn, and J. N. Israelachvili, *J. Chem. Phys.* 87 (1987) 1834.

[28] J. N. Israelachvili, S. J. Kott, M. Gee, and T. A. Witten, *Macromolecules* 22 (1989) 4247.

[29] H. K. Christenson, R. G. Horn, and J. N. Israelachvili, *J. Colloid Interface Sci.* 88 (1982) 79.

[30] N. N. Gosvami, S. K. Sinha, W. Hofbauer, and S. J. O'Shea, *J. Chem. Phys.* 126 (2007) 214708.

[31] N. N. Gosvami, S. K. Sinha, M. P. Srinivasan, and S. J. O'Shea, *J. Phys. Chem. C* 112 (2008) 297.

[32] R. Lim and S. J. O'Shea, *Phys. Rev. Lett.* 88 (2002) 246101.

Chapter 5: Interfacial Structure of Liquids - Hydrophilic Interface under Specific Chemical Interaction

5.1 Interfacial structures of polar liquid on hydrophilic interface

In Chapter 4, the interfacial structure of hydrocarbons was found to be sensitive to its steric configuration over the inert CH_3-terminated monolayer. In this chapter, effects of chemical interaction for structuring interfacial liquids are discussed. Hydrophilic groups contained in liquid or solid surface, can cause a strong chemical interaction through a hydrogen bond, rather than such as van der Waals interaction. Specific intermolecular interaction often becomes a key in structuring interfacial liquids, which has been believed to be important consequences in biological system such as denaturalization of proteins or process of enzymes recognizing specific molecules.

At first in this chapter, the contributions of surface functional group are discussed. The state-of-the-art AFM has been applied to compare the interfacial water structure with sub-nanometer scale over two well-defined, functionalized surfaces: OH-terminated mercaptoundecanol and COOH-terminated mercaptoundecanoic acid monolayers self-assembled on gold surface. In addition, interfacial structure of liquid should be sensitive to not only chemical properties of solid substrates, but also those of liquids themselves. In order to discuss the contribution of chemical nature of liquid for constructing the interfacial structure, the structures of liquid alcohols were further investigated. Alcohol contains both a reactive OH group and inert alkyl chain, and moreover can present various steric environments around the OH group. Such multi-chemical character of alcohols is appropriate to discuss the effect of specific chemical interaction for structuring interfacial liquid, by comparing the interfacial structure of alcohols. The author conducted the two dimensional Δf distribution measurement for primary, secondary and tertiary, short-chain and long-chain alcohols over hydrophilic monolayers. The Δf distribution also determined over the alcohol adsorbed layer on HOPG whose surface presents local heterogeneity of chemical functional groups.

5.2 Experiment

5.2.1 Operating condition of AFM

The microscope was a Shimadzu WET-SPM 9600 modified with a low noise optical deflection sensor [1] as described in Chapter 2. Silicon cantilevers with a nominal spring constant of 40 N m^{-1} (Nanosensors, NCH) were used with their backside coated by gold or aluminum. The resonance frequency of the cantilever oscillation was 130-150 kHz and the quality factor (Q) of resonance was typically 10 in the aqueous solutions and 5 in the organic compounds. To stabilize the resonance oscillation in the low-Q environment, band pass filters of Q = 20 were inserted in feedback loops. All the experiments were performed at room temperature. The vertical and lateral drift rate of the cantilever was on the order of 1 and 0.1 nm min^{-1} relative to the surface, respectively.

5.2.2 Preparation of imaging solutions

The two neutral aqueous imaging solutions, 50 mM KCl or NaCl solution, were prepared with KCl (Nakarai, >99.5%) or NaCl (Wako, >99.5%) dissolved in Millipore water. The phthalate buffer solution of pH 4 (Wako) was used as received. Organic solvents were used as received by suppliers; 1-octanol (Wako, >98%), 2-octanol (Wako, >98%), 2-methyl-2-heptanol (Tokyo Chemical Industry, >97%), 1-butanol (Wako, >99%) 2-methyl-2-butanol (Wako, >98%), 1-decanol (Wako, >95%) and octanoic acid (Wako, >98%).

5.3 Preparation of hydrophilic SAMs

5.3.1 Literature review

As reviewed in 4.1.2, alkanethiolate SAM provides a well-defined surface suit for AFM observation. SAM formation of organosulfur molecules occurs from either solution and vapor phase. Especially, assembly from the solution has widely used from the early stage of the research because of its convenience. Numerous experiments have been demonstrated to reveal some of the basic structural characters of self-assembly process, and practical protocols for preparing SAMs has been established. [2] The most common protocol for preparing SAMs is immersion of a freshly prepared metal substrate into a dilute solution of alkanethiols for 12-24 hours at room temperature. Following the fast adsorption on the substrate from the solution, the adsorbed molecules slowly reorganize to maximize the density of molecules. The slower process requires 12-24 hours. This procedure has been widely used because dense packed monolayer of the thiolates is formed, which is beneficial for experiments in terms of reproducibly producing the same quality of the monolayer.

However various experimental factors can attribute the self-assembly process such as concentration of the solution, length of time for immersion, solvent, pH and temperature, as summarized in early reviews [3-5]. In the use as well-defined surface of atomistic structure, experimental conditions should be optimized to exert desired function. Assembly of the organosulfur molecules contained a hydrophilic end-group such as hydroxyl, carboxyl or amino groups, requires special care for preparation because moiety of the end-group can prevent the formation of well-ordered monolayer such as due to dimerization by hydrogen-bond. [6]

Flat, well-ordered monolayer is needed for purpose of sub-nanometer scale AFM observation. Here the experimental conditions were optimized to make a hydrophilic monolayer suit for AFM observation.

5.3.2 Preparation of hydrophilic SAMs suit for AFM observation

The monolayers were prepared on vacuum-deposited, 150-nm-thick gold films. Cleaved mica wafers were annealed at 723 K in a vacuum of 10^{-5} Pa and exposed to a custom-made gold evaporator (Sensor & Works, Japan).

To start, the gold-deposited wafers were dipped in 1 mM ethanol solution of 11-mercaptoundecanol (Wako, >98%) for 24 hours as a general procedure. The dipped wafers were multiple-rinsed with pure ethanol and immediately immersed in an aqueous KCl solution of 50 mM for AFM observation at room temperature. Figure 5.1 shows the topography of the prepared monolayer. Epitaxial growing gold island was clearly observed in the image, but the small particles whose diameter are about 2 nm were found on the flat terrace. The particles were not removed by rinse of water, dodecane, or acetone, which suggested the strong adsorption on the terrace. It was supposed that the particles originated from aggregates of excess thiol adsorbates from the concentrated solution.

To reduce excess adsorbates, the concentration of the prepared solution was reduced to be 10 μM. Figure 5.2 shows the topography of the mercaptoundecanol SAM prepared by the improved procedure. There are few aggregate found on the terrace. COOH-terminated mercaptoundecanoic acid SAM also showed the clean terrace when preparing with the same procedure. The hydrophilic SAMs using the following section were prepared by the optimized procedure: 24 h immersion in 10 μM ethanoic solution.

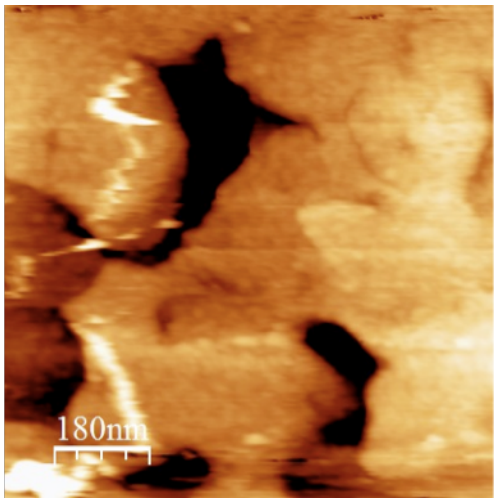

Figure 5.1. Topography of mercaptoundecanol SAM prepared by 24-hours immersion of the 1 mM ethanol solution.

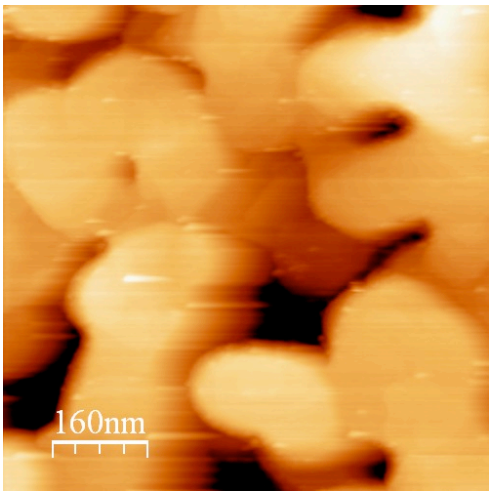

Figure 5.2. Topography of mercaptoundecanol SAM prepared by 24-hours immersion of the 10 μM ethanol solution.

5.3.3 IRRAS measurement

The author checked and confirmed the chemical composition of the prepared monolayers with infrared reflection absorption spectroscopy (IRRAS). The spectra in Fig. 5.3 were observed in air using a Fourier-transform spectrometer (Jasco, FT/IR-610) with an attachment for reflection absorption (Jasco, RAS PRO410-H). The wavenumber resolution was set to be 8 cm^{-1} and 256 interferograms were accumulated for each spectrum.

The IRRAS spectra of (a) the COOH-terminated SAM and (b) the OH-terminated SAM contained double peaks at 2930-2850 cm^{-1}. They were asymmetric and symmetric stretching modes of methylene groups. In addition, peaks appeared at 1724, 1614, 1455 and 1170 cm^{-1} on spectrum (a), assignable to stretching modes of the COOH terminal group, being consistent to an early work. [7] The broad absorption at 3285 cm^{-1} comes from the OH stretching. The COOH-related absorptions were absent on spectrum (b) of OH-terminated SAM. The absorption of OH stretching mode can be weak on OH-terminated SAMs as evidenced in a previous study. [8]

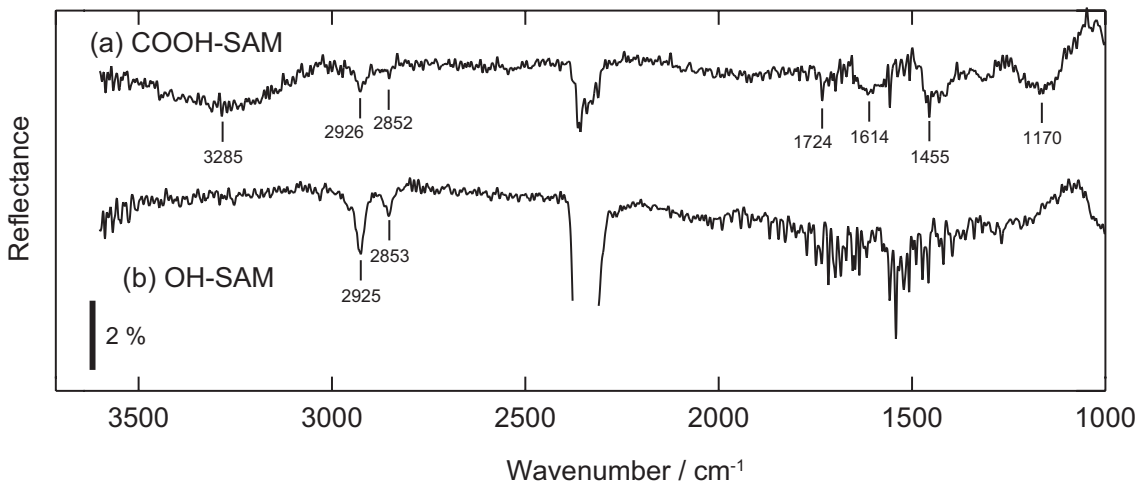

Figure 5.3. Infrared reflection absorption spectra of (a) COOH-terminated mercaptoundecanoic acid SAM and (b) OH-terminated mercaptoundecanol SAM observed in air.

5.4 Topography of hydrophilic thiolate SAMs in liquids

5.4.1. Topography in aqueous solution

The author checked the quality of the monolayers confirmed by topographic imaging in solutions. At first in this section, topography of the thiolate monolayers was observed in the 50 mM KCl aqueous solution. Figure 5.4. presents a wide-area topography of the OH-terminated monolayer. The tip was not in severe contact with the monolayer, since the time-averaged deflection of the oscillating cantilever was monitored and found to be nil, although the positive Δf set point suggested a repulsive tip-surface force. Gold substrate epitaxially grown on mica provided atomically flat terraces 200-300 nm wide with small pits. The pits were typically 10 nm in diameter and 0.3 nm deep. These are due to surface reconstruction with Au adatoms incorporated into Au-S bond as discussed in section 4.3. [9] Similar pits were found on COOH-terminated monolayers.

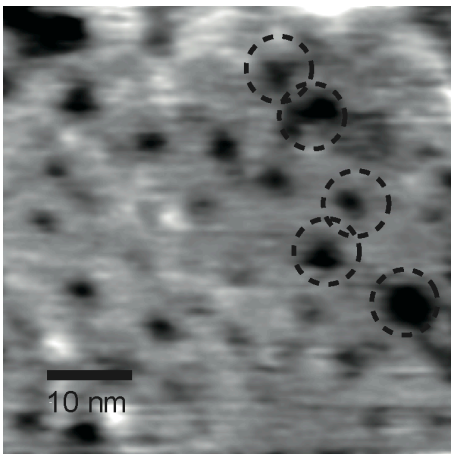

Figure 5.4. Wide-area topography of the OH-terminated thiol monolayer observed in the 50 mM KCl aqueous solution. Some of pits are marked with dotted circles. Oscillation amplitude: 0.3 nm. Frequency shift: +200 Hz.

Figure 5.5(a) presents narrow-area topography of the OH-terminated monolayer. Hexagonally aligned protrusions were identified with a regular spacing of 0.5 nm. The hexagonal arrangement with this spacing is commonly observed on *n*-alkanethiolate monolayers assembled on Au(111) substrates, as illustrated in panel (b). [10-13] The protrusions were assigned to individual OH end-groups of the thiolates. The presence of well-ordered thiolate monolayers was evidenced by these topographic images.

There was no sign of OH end-groups pairing with each other. This is natural in the aqueous solution, since the solvent water is readily able to form hydrogen bonds with the end-groups. When water is hydrogen-bonded to the hydrophilic end-groups tightly, those water molecules may possibly present protrusions in topography. However, this is not probable with the topography of (a). The Δf set point in the imaging scan was +800 - +1000 Hz. On the other hand, the amplitude of Δf modulations caused by hydrogen-bonded water layers was 200 Hz or less, as mentioned in the following section. The large Δf set point suggested that the scanning tip penetrated hydrogen-bonded water layers and descended to the surface of the thiolate monolayer. It was also supported the assumption that the similar protrusions appeared in the topography of a CH_3-terminated thiolate monolayer immersed in *n*-hexadecane where specific adsorption of liquid was not expected, as shown in Fig. 4.2(b).

Figure 5.5(c) presents narrow-area topography of the mercaptoundecanoic acid monolayer. The pK_a of COOH in a siloxane-anchored carboxylate monolayer was around 5. [6] The COOH end-group of mercaptoundecanoic acid was expected to be deprotonated and negatively charged in the neutral solution, as COO^--terminated. The topography of Fig. 5.5(c) showed that protrusions were identified in a hexagonal arrangement with spacing of 0.5 nm. The protrusions should thus be the result of individual COO^- end-groups.

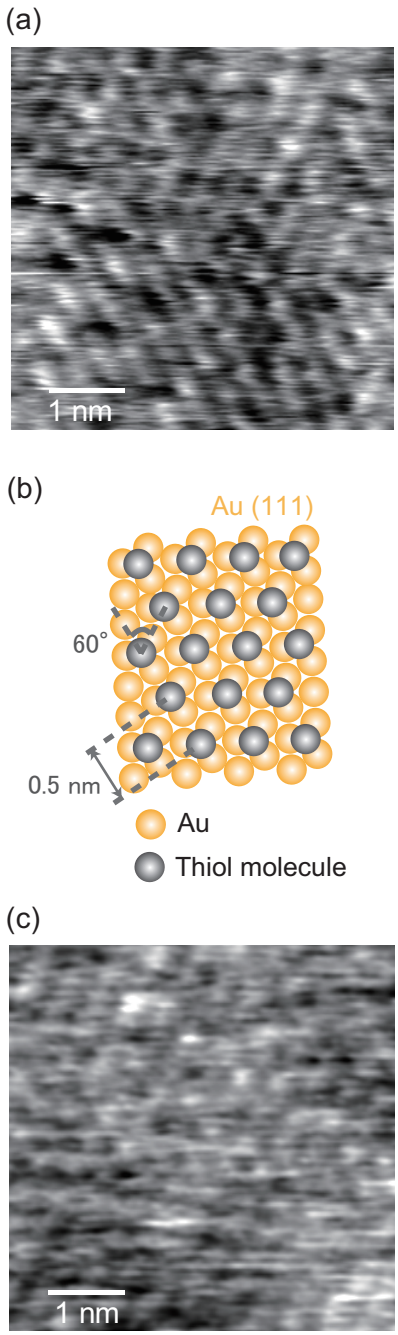

Figure 5.5. Narrow-area topography of (a) OH-terminated mercaptoundecanol monolayer in the KCl solution. (b) An illustration of the hexagonal arrangement of thiolates on Au(111). (c) Narrow-area topography of COOH-terminated mercaptoundecanoic acid monolayers. Oscillation amplitude: (a) 0.2 nm and (c) 0.1 nm. Frequency shift: (a) +1000 Hz and (c) + 800 Hz.

5.4.2. Topography in alcohol

In order to further check the stability of the structure of the SAMs when immersed in alcohols, topography of the prepared OH- and COOH-terminated SAMs were scanned also in 1-octanol. Figure 5.6 shows set of the topographies of COOH-terminated mercaptoundecanoic acid SAM. In wide-area scans (a), pits of the gold substrate were identified as in the aqueous solutions. These pits are evidence of thiol adsorption.

On pit-free portions, a hexagonal arrangement of assembled thiolate molecules would be apparent in the narrow-area scan because hexagonal lattice of individual thiolate molecules clearly observed in an aqueous solution, as presented one of which is shown in Fig. 5.5(c). However, it was difficult to identify the hexagonal arrangement on narrow-area images. The author ascribed the poorly ordered topography to COOH end-groups fluctuating on the well-ordered monolayer. An IRRAS study indicated that carboxyl end-group can make a hydrogen-bond pair to adjacent carboxyl with hydrogen bond, and about half of neighbor COOH groups bound by the single hydrogen bond. [14] A carboxyl end-group can choose any one of the six neighbor carboxyls as hydrogen bond pair because each end-group has rotational freedom around the C-C bond to the assembled alkyl moiety. Here note that the self-assembled structure still remained even when the end-groups formed hydrogen bond pairs in the alcohol. The authors confirmed that the intrinsic structure of the monolayer was preserved even after immersion in 1-octanol where the topography of Fig. 5.6(b) was acquired. After obtained the topography in 1-octanol, the wafer were dried in N_2 stream, and then immersed in aqueous solution of 50 mM KCl. The topography of the wafer of COOH-SAM which had been taken from 1-octanol was determined in the aqueous solution as shown in Fig. 5.6(c). The $\sqrt{3}\times\sqrt{3}$ structure was clearly observed as the topography shown in Fig. 5.5(c). This result evidenced that not a destruction of the monolayer but a fluctuation of the terminal site resulted in the poor resolved topography. The protruded end-groups have considerable mobility to select a more stable coordination, whereas S-Au linkage remained rigid. In addition, the COOH end-groups prefer to accept hydrogen bonds from solvent water than a neighbor COOH group in

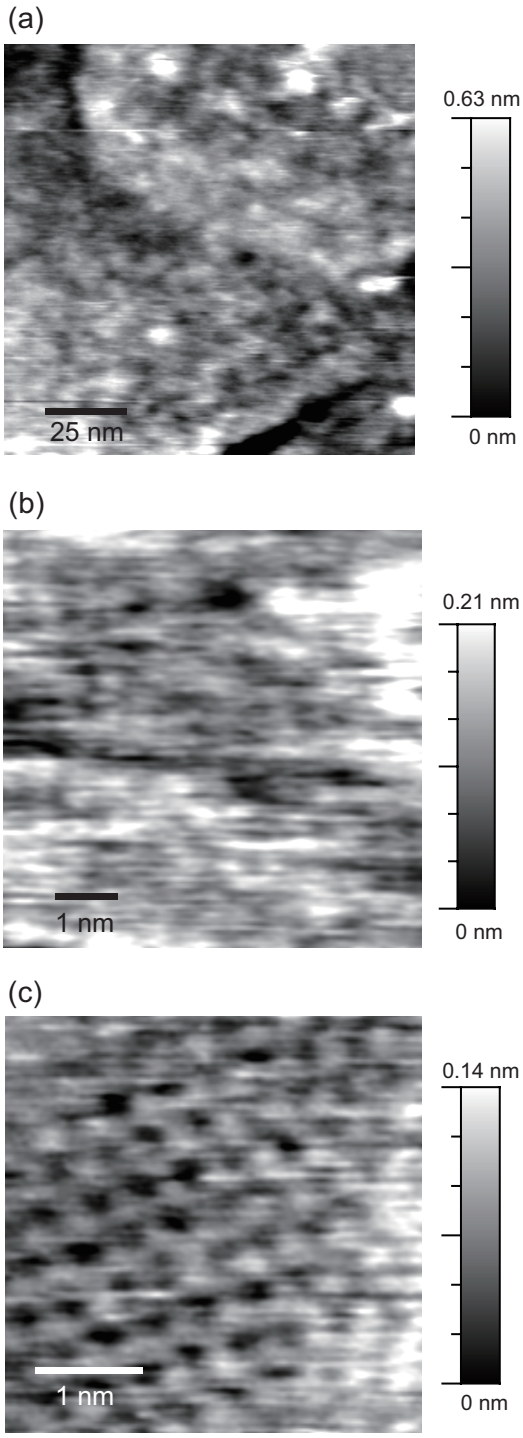

Figure 5.6. (a) A wide-area and (b) a small area topography of COOH-terminated monolayers in 1-octanol. (c) The topography obtained in aqueous solution after immersion in 1-octanol. Oscillation amplitude: (a) 0.2 nm and (b,c) 0.1 nm. Frequency shift: (a) +1000 Hz, (b) + 600 Hz and (c) +600 Hz.

aqueous solutions, whereas the end-groups prefer to make the bonds with the neighbors in facing to an alcohol. 1-Octanol is a less efficient hydrogen-bond donor or acceptor than water, in which the end-groups prefer to pair with each other. The paring probability may be subject to hydrogen bonding ability of the end-groups toward liquids.

The results of COOH-terminated SAM are intermolecular hydrogen bonds affected the AFM topography. However OH-terminated SAM presented different topography from the COOH-terminated one though the hydroxyl group is capable to make hydrogen bonds each other. Figure 5.7 shows set of the topography of OH-terminated mercaptoundecanol SAM. In wide-area scans (a), pits of the gold substrate were identified as on the COOH-terminated SAM. In contrast to the COOH-terminated SAM, individual end-groups of the thiolate molecule were clearly identified in a narrow-area scan of Fig. 5.7(b). The hexagonal arrangement aligned with regular spacings of 0.5 nm, suggested a ($\sqrt{3}\times\sqrt{3}$) structure of the adsorbed thiolate monolayers. The well-ordered topography suggested the absence of end-group-to-end-group hydrogen bond, though the OH end-group is possible to become a hydrogen bond donor or accepter. This is probably due to the small size of OH end-groups. The nearest neighbor distance of 0.5 nm is too large to make a hydrogen-bonded pair. In addition, the location of the OH end-groups may also prevent the OH groups paring with each other due to surrounding alkyl chains tilted to the gold surface.

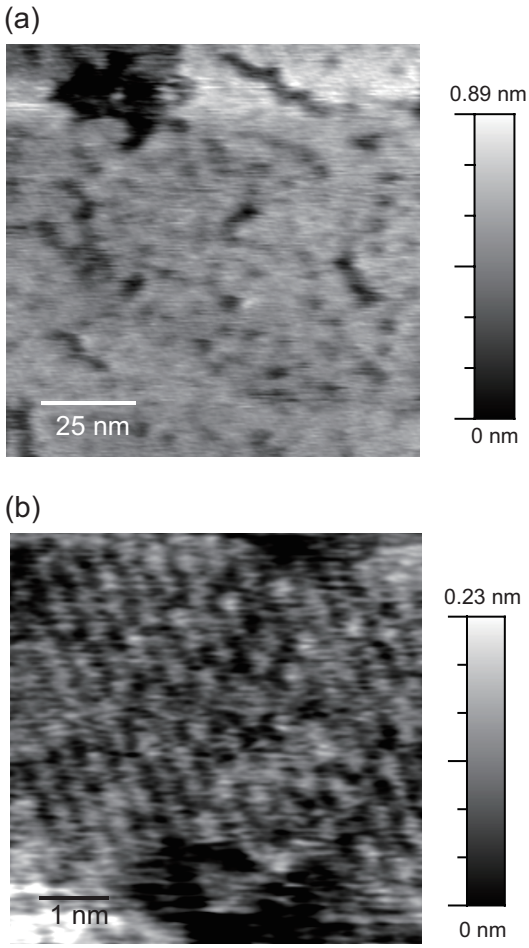

Figure 5.7. (a) Wide-area and (b) narrow area topography of OH-terminated monolayers in 1-octanol. Oscillation amplitude: (a) 0.2 nm and (b) 0.1 nm. Frequency shift: (a) +1000 Hz and (b) + 800 Hz.

5.5 Interfacial structures of water over hydrophilic SAMs

5.5.1 Water structure over OH-terminated SAM

Over the monolayer depicted in Fig. 5.5(a), a cross-sectional Δf distribution was observed as a function of the vertical and lateral coordinates. Figure 5.8(a) shows the Δf distribution in the 50 mM KCl aqueous solution. Positive (negative) Δf is shown to be bright (dark). Periodic protrusions and grooves of the brightest region appeared at the bottom of the Δf distribution. When the tip descended into that region, Δf increased monotonically. The monotonic increase is a sign of tip contact to a solid, OH-terminated monolayer in the present case. The topography of the brightest region, which is traced with a solid line to guide the eye, represents the physical topography of the monolayer. Hence, the periodic protrusions appeared in the trace are assigned to individual OH end-groups aligned with hexagonal order. The protrusion-to-protrusion distance was 0.5 nm in Fig. 5.8(a), which is consistent with the closely packed thiolate monolayer.

Figure 5.8(b) depicts Δf-distance curves averaged over a topographic protrusion or groove. The frequency shift was modulated from negative to positive at distances of 0.3-0.4 nm over the groove, while monotonically reduced on the protrusion. Modulated regions appeared as dark-to-bright changes along the vertical coordinate in the distribution of Fig. 5.8(a). Those Δf-modulated regions were always present on the topographic grooves. This suggests that the water density was modulated from low to high in the regions between the two adjacent OH end-groups. Based on this argument, a possible structure of interfacial water is proposed as illustrated in panel (c). Water molecules are hydrogen-bonded to adjacent OH end-groups in a bridge form, while they should remain mobile in translational and orientational movements. This is consistent with the prediction of a molecular dynamics simulation, [15] in which most OH end-groups are fully coordinated with water and separated from each other by one or more water molecules.

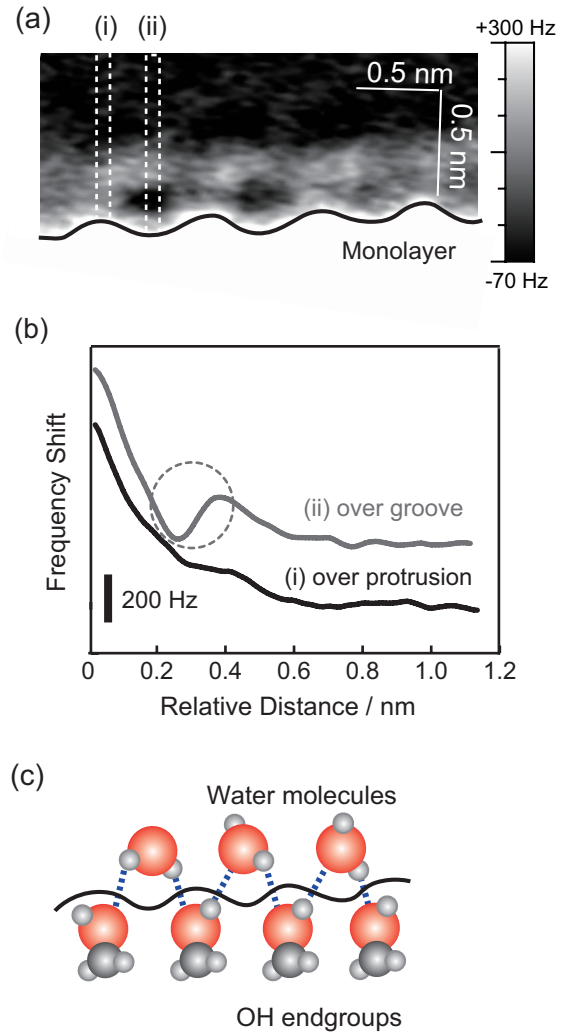

Figure 5.8. (a) The Δf distribution cross-sectional to the OH-terminated monolayer in the KCl solution. Amplitude of cantilever oscillation: 0.2 nm. (b) Averaged Δf-distance curves over a topographic protrusion or groove. Each curve was obtained with averaging 5 curves observed in area (i) or (ii). The two curves are vertically shifted so as not to overlap. The Δf-modulated region is marked with a dotted circle. (c) A possible picture of interfacial water. The solid and dotted lines represent the monolayer topography and hydrogen bonds respectively.

Here the author notes that the lateral force distribution is directly linked to the lateral density distribution. In an ideal FM-AFM measurement, the force is depicted along the direction of tip oscillation, in the present case, vertical direction to the surface (F_z). The suggested equation (3.23) indicating the relation of force and density distribution when the tips are small enough to achieve subnanometer resolution in Δf distribution, is represented as:

$$F_z(x,y,z) = -\alpha \frac{\partial \rho(x,y,z)}{\partial z} \qquad (5.1)$$

Hence the major conclusions about the lateral relation between the force and density distribution do not depend on the interpretation of force distribution as far as the vertical force modulations does not have a cross-talk relation to density distribution in lateral dimension. This is a simple but highly possible assumption. The monotonic reduction of tip-surface force on the protrusion can be ascribed to the electric double layer force. 50 mM KCl electrolyte was added to the solution to reduce the decay length of possible double layers, but a finite contribution still remained. The structured water created force modulations over the grooves superposing on the monotonic double layer force.

5.5.2 Water structure over COO^--terminated SAM

The structure of interfacial water was determined over another hydrophilic monolayers to discuss the contribution of end-groups for structuring. Figure 5.9(a) presents a Δf distribution over the COO^--terminated monolayer shown in Fig. 5.5(c), obtained in the 50 mM KCl aqueous solution. The bottom trace represents the physical topography, with the protrusions assignable to individual COO^- end-groups. At this interface, Δf-modulated regions appeared on top of the topographic protrusions, as demonstrated by the averaged Δf-distance curves in panel (b). The modulations on the protrusions suggest that water molecules sit on top of the deprotonated end-groups. It is stressed here that water molecules are not located on the topographic grooves, although the grooves are wide enough for a water molecule to sit in. If a water molecule were a hard sphere having lost its chemical nature, it would surely occupy the hollow site in the groove to reduce the vacant volume. This was not found to be the case, however.

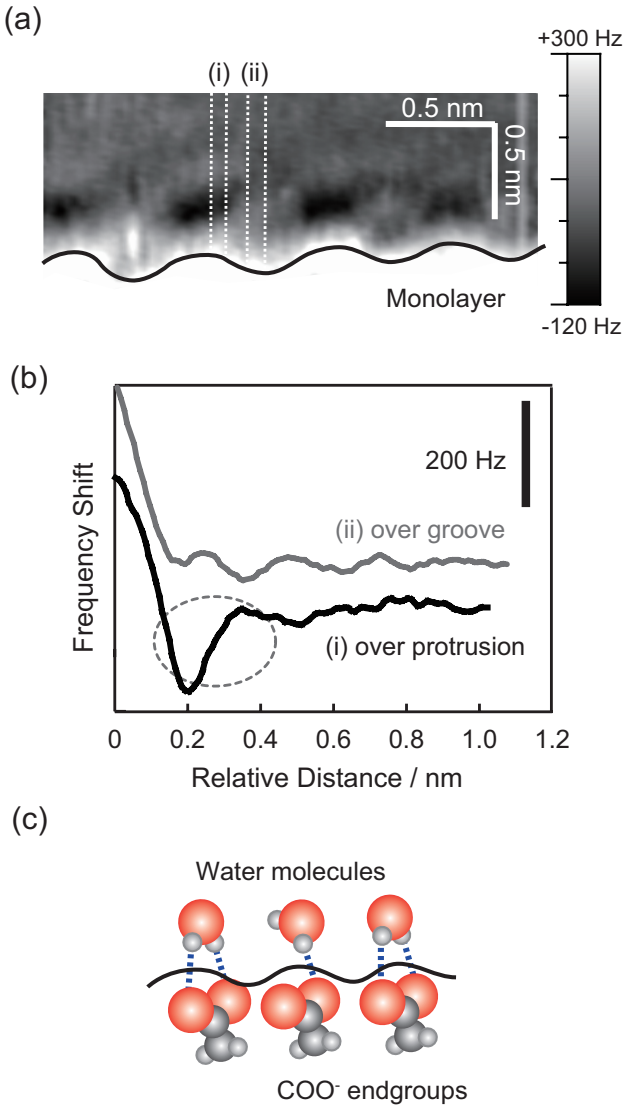

Figure 5.9. (a) The Δf distribution cross-sectional to the COO^--terminated monolayer in the KCl solution. Oscillation amplitude: 0.1 nm. (b) Averaged Δf-distance curves over a topographic protrusion or groove. Each curve was obtained with averaging 5 curves observed in area (i) or (ii). The two curves are vertically shifted so as not to overlap. The Δf-modulated region is marked with a dotted circle. (c) A possible model of local water structure. The solid and dotted lines represent the monolayer topography and hydrogen bonds.

The result suggested the dominant contribution of interaction between water and the COO^- end-group. The energetic advantage of forming hydrogen bonds toward the end-groups should be superior in on-top water coordination to that between them as over the OH-terminated SAM. Robertson et al. [16] conducted the IR absorption and ab initio calculation study of hydrated complex of triatomic anions (SO_2^-, CH_3COO^-, $CH_3NO_2^-$, NO_2^- and so on.), and pointed out that the separation of two hydrogen-bond donor site to water had an effect on the hydrogen-bond coordination of water. Acetate anion was possible to have a configuration where both the OH groups of water are attached to both oxygen atoms of acetate anion.

The interaction between water and the COO^- end-group was evidenced to be strong by ab initio calculation of hydrated clusters of acetate anions. [17] In that study, first layer of water molecules adjacent to carboxylate group was found to form two hydrogen bonds with a COO^- group in a bidentate fashion where the number of clustered water molecules is 1-3. The association of the water of monohydrated anion is strong (-19.6 kcal/mol, that is larger than that of water dimer, -5 to -7 kcal/mol [18]), and the binding energy remains to be strong even when the number of hydrated water molecules increases.

Owing to such a strong interaction between carboxylate and water, the hydrated molecules were predicted to localize the on top of COO^- groups. One of possible coordination of the structured water is illustrated in panel (c) of Fig. 5.9. Note that two of the hydrogen bond of hydrated water was not necessarily directly to the two oxygen atoms of COO^- end-groups. The simulation [17] also expected that hydrated water is possible to make one of the hydrogen bonds to another hydrated one, resulting in a ring like structure consisting of several waters and a carboxylate. Possible configurations of water being bridge or single hydrogen bond to the COO^- end-groups described in the illustration (c).

5.5.3 Water structure over COOH-terminated SAM interface in acidic solution

In the neutral solution, the end-groups of mercaptoundecanoic acid are deprotonated to be COO^-. The on-top structure of interfacial water may be caused by the negative charge on the deprotonated end-groups. To examine this possibility, the author observed Δf distributions for the phthalate buffer solution facing a mercaptoundecanoic acid monolayer. The COOH end-groups could not be deprotonated in the acidic buffer solution (pH = 4). The author checked the topography of the monolayer in the acidic buffer solution. The COOH-terminated thiolate monolayer again presented hexagonally ordered topographic protrusions as shown in Fig. 5.10(a). The structure of the SAM was independent to the charge state of the end-group. The Δf distribution recorded over the neutral COOH end-groups is shown in panel (b) together with averaged Δf-distance curves in panel (c). Δf-modulated regions appeared on top of the topographic protrusions as in the KCl aqueous solution. This shows that the enhanced water presence on top of the COO^- or COOH end-group was insensitive to their charge, be it negative or neutral. The two coordination sites per COO^- or COOH end-group may be the key behind the on-top coordination of the interfacial water.

In the neutral acetate hydrated cluster, the simulation study [17] suggested that the water molecules are stable between the COO and CH_3 group with a chain linking C-H...O-H bond, as well as on top of the COO group with bridge hydrogen bond to the COO group. However water coordination to CH_2 group of the thiolate was not observed in this study. This may be due to stacking moiety of the alkyl chains. Water molecules cannot access to the buried CH_2 group. As a result, the on-top coordination of water was only observed.

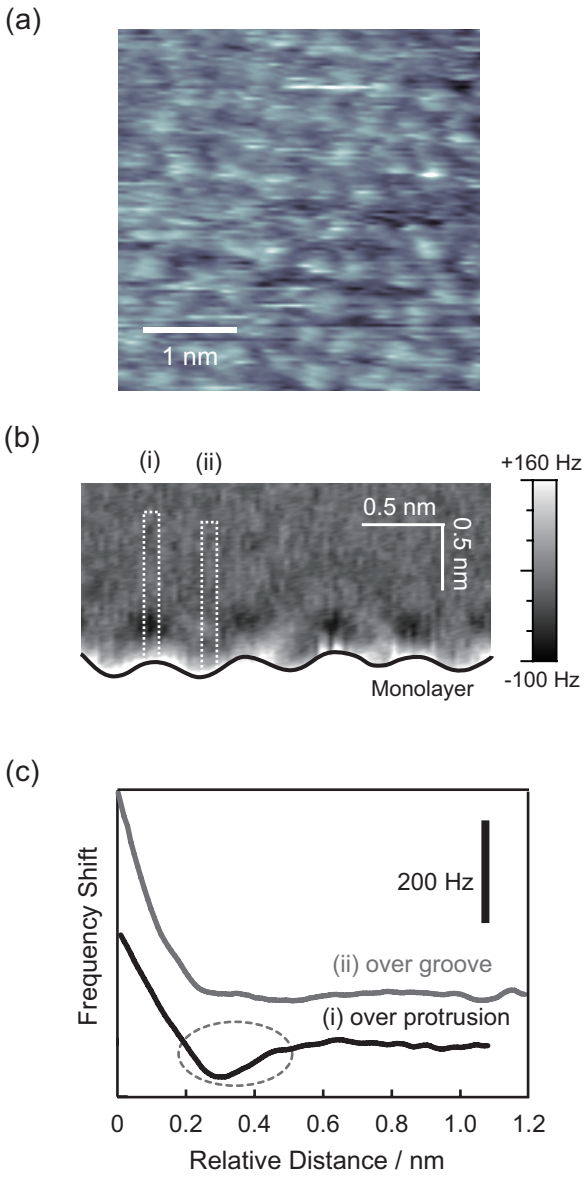

Figure 5.10 The mercaptoundecanic acid monolayer immersed in the phthalate buffer solution. (a) Topography of the monolayer. Cantilever oscillation amplitude: 0.2 nm. Frequency-shift set point: +200 Hz. (b) Δf distribution cross-sectional to the monolayer. Cantilever oscillation amplitude: 0.2 nm. (c) Averaged Δf-distance curves over a topographic protrusion or groove. Each curve was obtained by averaging 5 curves in each area (i) or (ii). The two curves are vertically shifted so as not to overlap. The Δf-modulated region is marked with a dotted circle.

5.5.4 Water structure insensitive to electrolytes

Here the author checked and excluded a possible contribution by electrolytes to the cross-sectional Δf distribution. The mercaptoundecanoic acid monolayer was immersed in the NaCl solution. The COOH end-groups should have been deprotonated, and the resultant COO^- end-groups exhibited hexagonally ordered protrusions as seen in Fig. 5.11(a). The insensitive topography to the solute cations indicates that the solute cations were less possible to adsorb on the deprotonated end-group. In the cross-sectional Δf distribution of panel (b) and averaged force curves in panel (c), Δf-modulated regions appeared on top of the COO^- end-groups, as seen in the KCl solution.

The OH-terminated monolayer was further examined in the phthalate buffer solution. Hexagonally ordered topography was observed, as shown in Fig. 5.12(a). Panel (b) shows a Δf distribution for the phthalate buffer solution cross-sectional to the OH-terminated monolayer, together with the Δf-distance curves in panel (c). Δf-modulated regions were present over the topographic grooves, as observed in the KCl solution facing the OH-terminated monolayer. The acidity of the solution and different solute composition resulted in no qualitative modification of the Δf distributions. These results, shown in Figs. 5.11 and 5.12, suggest that the structure of interfacial water is qualitatively insensitive to the composition of electrolytes.

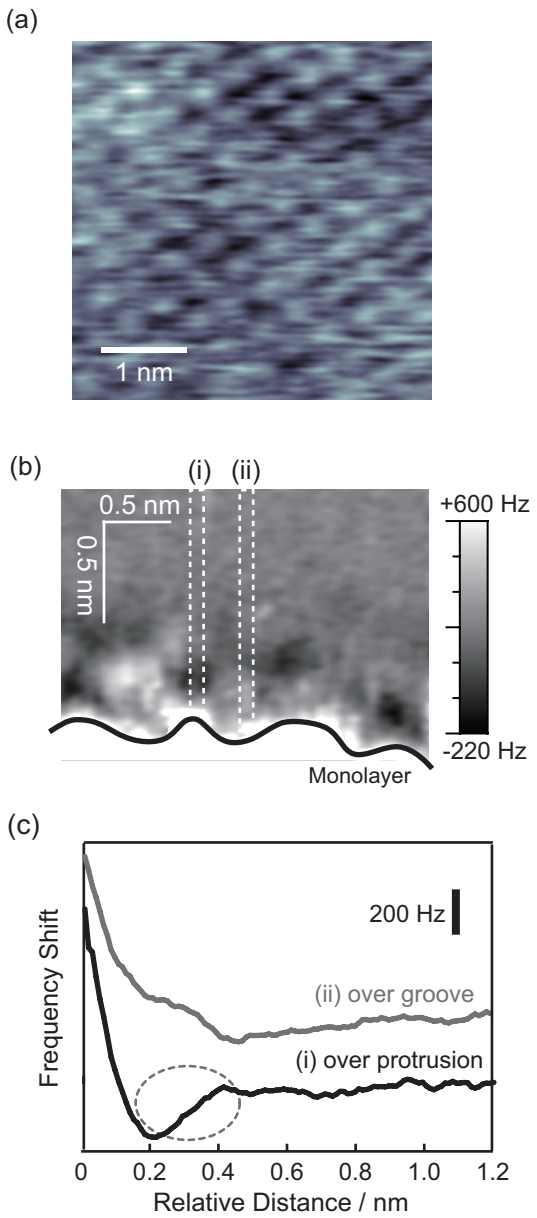

Figure 5.11 The mercaptoundecanic acid monolayer immersed in the NaCl solution. (a) Topography of the monolayer. Cantilever oscillation amplitude: 0.1 nm. Frequency-shift set point: +500 Hz. (b) Δf distribution cross-sectional to the monolayer. Cantilever oscillation amplitude: 0.1 nm. (c) Averaged Δf-distance curves over a topographic protrusion or groove. Each curve was obtained by averaging 5 curves in each area (i) or (ii). The two curves are vertically shifted so as not to overlap. The Δf-modulated region is marked with a dotted circle.

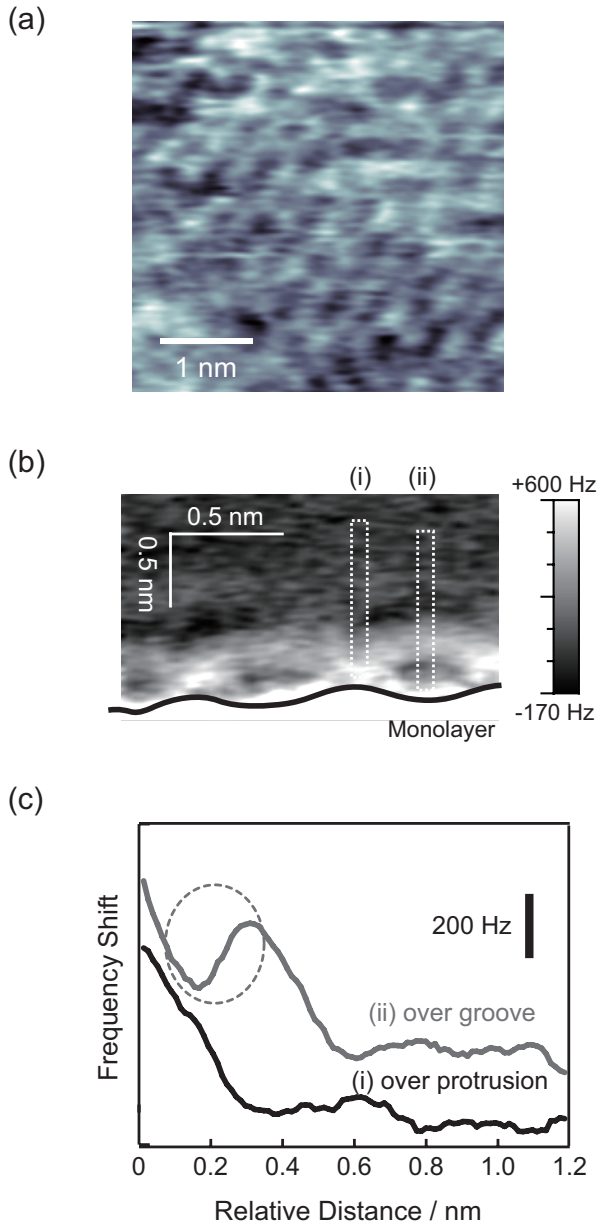

Figure 5.12 The mercaptoundecanol monolayer immersed in the phthalate buffer solution. (a) Topography of the monolayer. Cantilever oscillation amplitude: 0.2 nm. Frequency-shift set point: +600 Hz. (b) Δf distribution cross-sectional to the monolayer. Cantilever oscillation amplitude: 0.2 nm. (c) Averaged Δf-distance curves over a topographic protrusion or groove. Each curve was obtained by averaging 5 curves in each area (i) or (ii). The two curves are vertically shifted so as not to overlap. The Δf-modulated region is marked with a dotted circle.

5.5.5 Water structure insensitive to AFM tips

In Chapter 3, the author suggested the ideal model that an infinitely small tip apex probes a force distribution projected the density distribution of an *open* water-solid interface. This model works well to interpret the force distribution as first approximation. However, the author found that small fluctuation of the force caused by the specificity of individual small tip apex, could not be negligible. In addition, the tip apex could affect the force distribution as suggested in theoretical studies. [19,20] Here the author considers variations of the force distribution from specificity of individual tip apex.

Figures 5.8-5.12 showed representative results of cross-sectional Δf distributions on OH-terminated, COO^--terminated and COOH-terminated monolayers. Those indicated that the current tip apex was small enough to resolve the individual end-groups of the thiolate monolayers. The reproducibility of those distributions was checked and confirmed using separate cantilevers and separate monolayers. The Δf distributions were reproduced in a separate series of measurements. This suggests that the interfacial water structure is qualitatively insensitive to tip-induced confinement, as the atomic structure of the apex can vary from tip to tip. Hence the observed qualitative differences in the cross-sectional force distribution over different hydrophilic end-groups are due to the different water structure formed at the interfaces. Another measurement of the state-of-art FM-AFM [22] also supported this suggestion, which found that the oscillatory force modulation occurs solely as a result of structured water to the substrate, independent to the chemical composition of the tip.

5.6 Interfacial structures of alcohols over hydrophilic SAMs

In the previous section, interfacial structures of water are found to be sensitive to the end-groups of the monolayer, which suggested that intermolecular hydrogen bond between water and the monolayer has a key role in the structuring. Interfacial structure of liquid should be sensitive to not only solid substrates, but also chemical properties of liquids themselves, even of hydrogen bonding capable compounds. In this section, the structures of liquid alcohols were investigated with sub-nanometer scale, in order to discuss the contribution of chemical nature of liquid for constructing the interfacial structure.

5.6.1 Interfacial structures of primary alcohols over COOH-terminated SAM

The author started to investigate 1-octanol interface of the COOH-terminated SAM. Two-dimensional Δf distributions over the COOH-terminated SAM shown in Fig. 5.6 were determined as a function of the vertical and lateral coordinates to elucidate the interfacial liquid structures. Figure 5.13 shows a Δf distribution in 1-octanol. In the bottom of the distribution (a), protrusions and grooves of the brightest region appeared representing the physical topography of the SAM, that is traced by the black solid line for visualization. Five Δf-distance curves were averaged in each of the areas (i) to (v) and are depicted in the panel (b). Δf modulation with one maximum and two minima appeared in curves (ii) and (iv) as indicated by the dotted circles. On the curves (i), (iii) and (v), Δf decayed monotonically without the modulations. The alternate presence and absence of the modulation resulted from periodic heterogeneity in the layered octanol along the lateral coordinate, being epitaxial to the surface of the monolayer. Some site-specific interaction is needed to make the interfacial liquid epitaxial. The most probable origin of the interaction is the hydrogen bonds between OH of 1-octanol liquid and COOH on the SAM because a similar epitaxial relationship was found in the aqueous solution-COOH-SAM interface and the presence of water localization on top of the end-groups was proposed in 5.5. These results with 1-octanol and water suggest a dominant role for the terminal OH in liquid compounds in constructing interfacial structure of liquids epitaxial to the COOH-SAM.

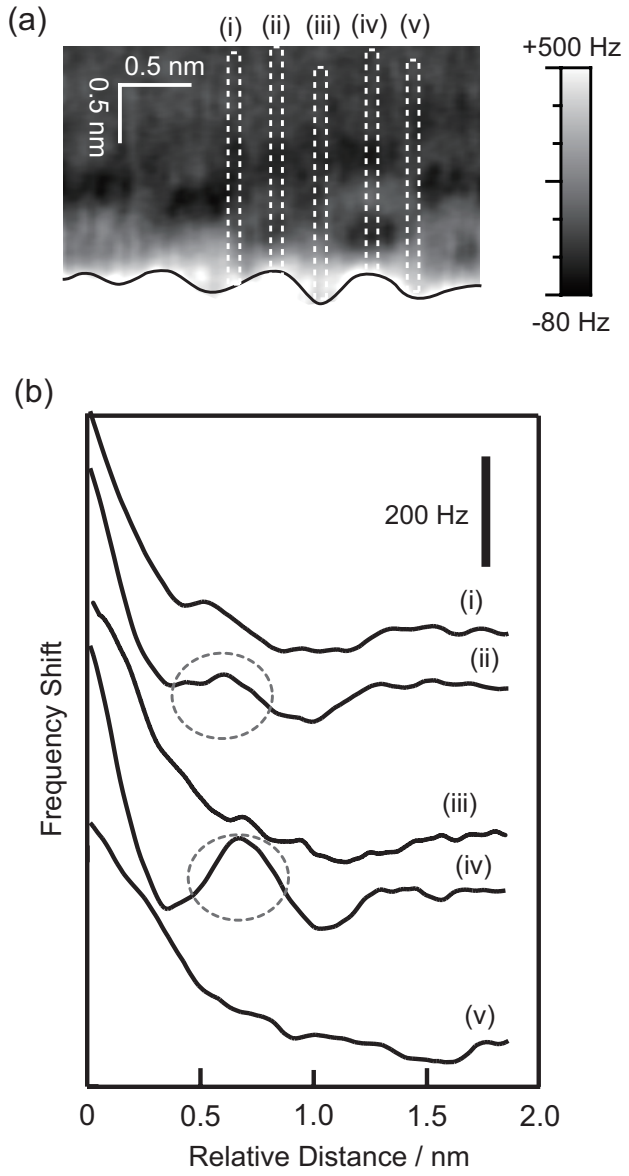

Figure 5.13 The mercaptoundecanoic acid SAM immersed in 1-octanol. (a) Δf distribution cross-sectional to the monolayer. Cantilever oscillation amplitude: 0.1 nm. (b) Averaged Δf-distance curves. Each curve was obtained by averaging 5 curves in each area (i) to (v). The two curves are vertically shifted so as not to overlap. The Δf-modulated region is marked with a dotted circle.

Unlike water, a primary alcohol contains an alkyl chain that is free from hydrogen bonding with the COOH end-group. The alkyl tail of alcohol, which consists most of the molecular volume in case of 1-octanol, should provide another contribution for the interfacial structure. In order to assess the contribution of the chain length for structuring primary alcohols, cross-sectional Δf distributions were further determined in shorter 1-butanol, as shown in Fig. 5.14(a). The averaged Δf-distance curves were extracted from the distributions as shown in panel (b). The Δf distributions in 1-octanol, 1-butanol, and water were qualitatively identical on the criterion of site-specific modulations. Insensitive distributions to the alkyl tail length suggest that the hydrogen bond between alcohols' OH and the COOH end-group dominantly contributed to construct epitaxial structures of the primary alcohols to lateral site of the surface.

In addition to this result, the separation between first and second minimums indicates the thickness of a liquid layer. The observed separation of Δf modulations was found to be 0.55 - 0.62 nm in 1-butanol and 0.60 - 0.66 nm in 1-octanol from the Δf-distance curves on the protrusion. The observed separations were comparable to that of at the interfaces of CH_3-terminated SAM and *n*-alkanes, 0.56 - 0.58 nm, as mentioned in Chapter 4. The insensitivity of the separation to the chain length suggested parallel orientation of *n*-alkanes with the molecular axis to the surface. This was also in the case of stacking of alcohol molecules. The number of atoms in contact with the solid is maximized per molecule in the first liquid layer in parallel orientation. Since van der Waals force is dominant interaction between the alkyl chains, the total energy was accordingly optimized. This can be applied to between the first and second layer as well. Franz and Butt found oscillatory modulations on force-distance curves over mica immersed in short-chain primary alcohols. [22] The separation of the modulation was increasing with longer length of the alkyl chain length, from 1.05 nm with 1-butanol to 1.65 nm with 1-octanol. The oscillation periods larger than 1 nm and sensitive to chain lengths suggested an upright orientation of the alcohols. Mica is composed of a sheet-like silicates with a rigid hexagonal arrangement of cations and anions. Surface OH groups should also be rigid and perpendicular to mica surface. The restricted orientation can explain the upright alcohols hydrogen-bonded to mica. The shorter separation over the COOH-SAM, suggesting the parallel orientation to the surface, is probably because the COOH end-groups on the thiolate monolayer are expected to be less rigid than the surface OH on mica. The fluctuating topography shown in Fig. 5.6(b)

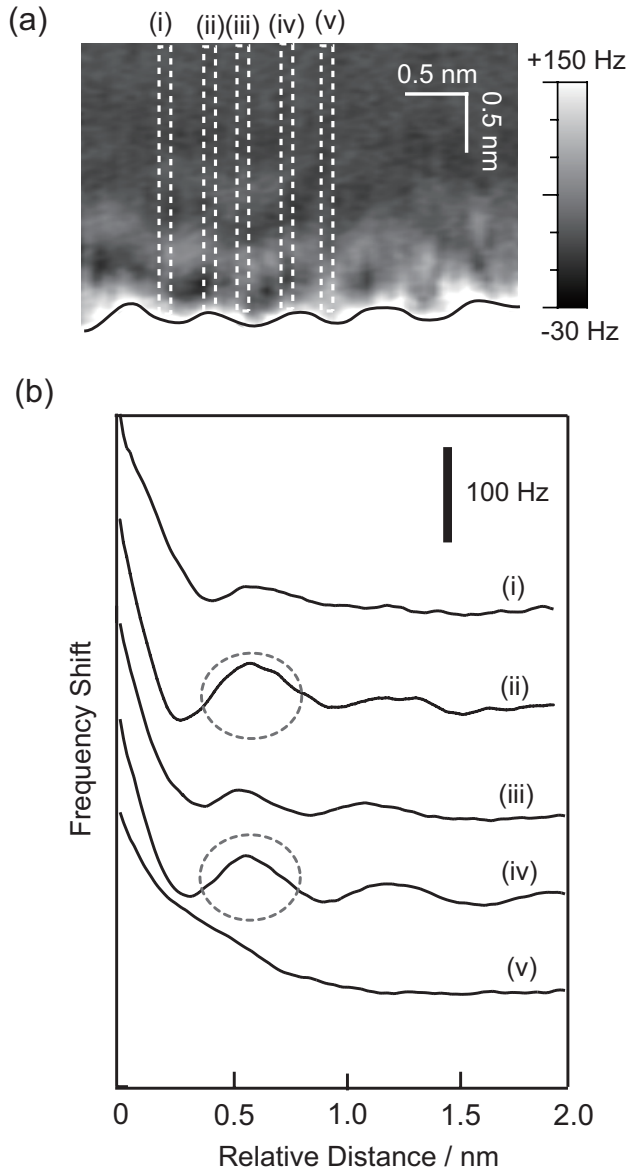

Figure 5.14 The mercaptoundecanoic acid SAM immersed in 1-butanol. (a) Δf distribution cross-sectional to the monolayer. Cantilever oscillation amplitude: 0.1 nm. (b) Averaged Δf-distance curves. Each curve was obtained by averaging 5 curves in each area of (i) to (v). The curves are vertically shifted so as not to overlap. The Δf-modulated region is marked with a dotted circle.

was interpreted as the creation and rupture of hydrogen bonds of neighboring end-groups. This interpretation is consistent with the flexible structure of the surface. Even on the COOH-SAM, the observed separation in 1-octanol was slightly longer than that in 1-butanol. A somewhat larger separation for 1-octanol compared with 1-butanol does suggest slightly tilted orientations. This may be due to the anisotropic hydrogen bond between the hydrophilic end-groups.

To sum up the discussion in this subsection, the site-specific interaction between OH of primary alcohols and COOH of the SAM attributed lateral structure of the interfacial liquid alcohols and the alkyl tails did the vertical structure. The hydrogen bond pins the molecule, whereas the alkyl tail is allowed to rotate around the pinned OH.

5.6.2 Interfacial structures of tertiary alcohols over COOH-terminated SAM

The primary alcohols showed the epitaxial structures on the COOH end-groups, suggesting that the hydrogen bonds between the end-groups of solid and liquid molecules attributed the structuring of interfacial liquid alcohol. The ability for hydrogen bonding is known to be sensitive to steric environments of hydrophilic groups. In this subsection, the interfacial liquid structure of tertiary alcohols was observed and compared with those of the primary alcohols. Different protection by adjacent alkyl chains is expected to affect the strength of hydrogen bond to COOH end-groups. The author carried out more in-depth discussions on the interaction between solid and liquid for structuring interfacial liquids.

Figure 5.15(a) shows a cross-sectional Δf distribution of 2-methyl-2-heptanol, a tertiary alcohol, over the COOH-SAM. The five Δf-distance curves were averaged in each of the areas (i) to (v) and depicted in Fig. 5.15(b). The averaged Δf-distance curves were uniform along the lateral coordinate, in spite of the corrugated topography of the monolayer as appears at the bottom of the distribution. As discussed in Chapter 4, laterally uniform Δf distributions were found in hydrocarbons interfaced with a CH_3-terminated SAM. The uniform layers observed in this study evidenced a limited contribution of the tertiary OH group in producing a site-specific, hydrogen-bond interaction. The laterally uniform liquid layers were also found in a shorter tertiary

alcohol. Figure 5.16 shows a cross-sectional *Δf* distribution and the averaged *Δf*-distance curves of 2-methyl-2-butanol over the COOH-SAM. The qualitatively identical *Δf* distributions of the two tertiary alcohols are in contrast to the epitaxial relation observed in the primary alcohols. A dominant role of the alkyl moieties was hence suggested in structuring the tertiary alcohols at the interfaces.

An early IR absorption study of liquid alcohols [23] showed that tertiary compounds presented smaller red shifts in the O-H stretching frequency than corresponding primary compounds. The extent of the red shift is regarded as a measure of the hydrogen bond strength of liquid alcohols. The smaller red shifts are interpreted with weaker strengths of tertiary alcohols due to the steric restriction around the OH group. A more detailed analysis of the red shift was conducted with alcohol dimers in a jet spectroscopy study. [24] A molecular dynamics simulation [25] predicted in an aqueous solution of *tert*-butanol that each butanol accepts at most one hydrogen bond from water, though an alcohol potentially receives two hydrogen bonds. The bulky *tert*-butyl group is thought to reduce the accessibility of the OH group.

On the basis of these early findings, it is natural to assume that the dimethylhexyl moiety of 2-methyl-2-heptanol and dimethylpropyl moiety of 2-methyl-2-butanol negatively affects the hydrogen bonding ability of the tertiary OH groups. The hydrogen bond strength was too small to form an epitaxial distribution of the tertiary alcohols, and the laterally uniform liquid layers appeared as a result.

The distance of the first and second *Δf* minima was 0.64 - 0.71 nm in 2-methyl-2-heptanol and 0.61 - 0.70 nm in 2-methyl-2-butanol. The large distances of the tertiary alcohols are reasonable as compared with those of the primary alcohols mentioned in 5.6.1. A positive relationship between the liquid layer separations and the branching extent has frequently been reported [26,27] as discussed in 4.4.

The strength of site-specific interactions to the COOH-SAM showed a positive relationship with the esterization capability of primary and tertiary alcohols, which is acknowledged in organic chemistry as a steric effect. It is reasonable because the accessibility to alcoholic OH provides a common origin of the two properties, the hydrogen bonding and esterization reactivity.

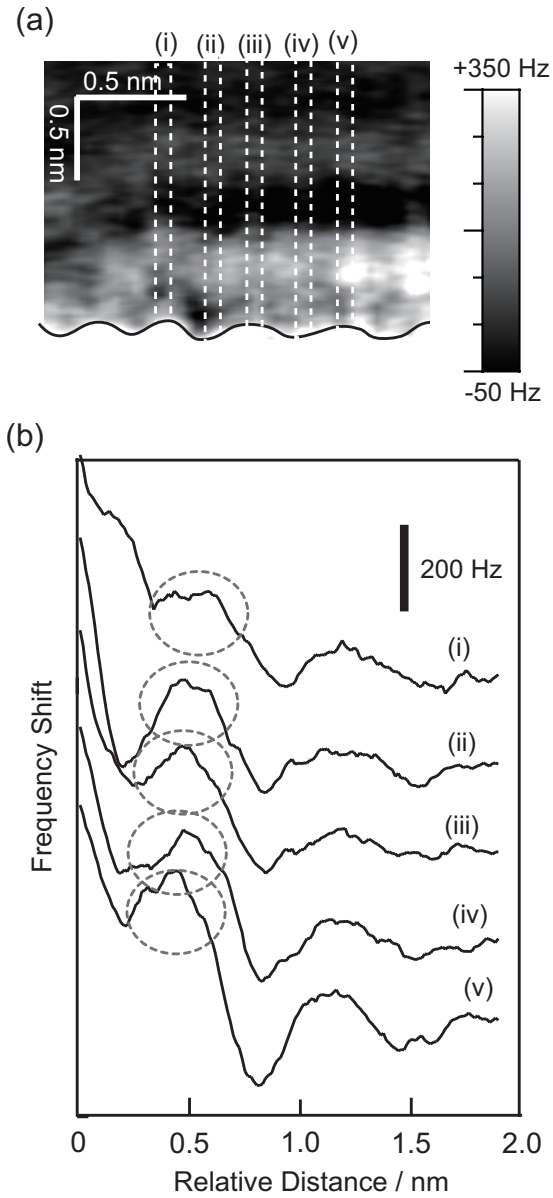

Figure 5.15 (a) A Δf distribution cross-sectional to the mercaptoundecanoic acid SAM immersed in 2-methyl-2-heptanol. Cantilever oscillation amplitude: 0.1 nm. (b) Averaged Δf-distance curves. Each curve was obtained by averaging 4 curves in each area (i) or (ii). The curves are vertically shifted so as to not overlap. The Δf-modulated region is marked with a dotted circle.

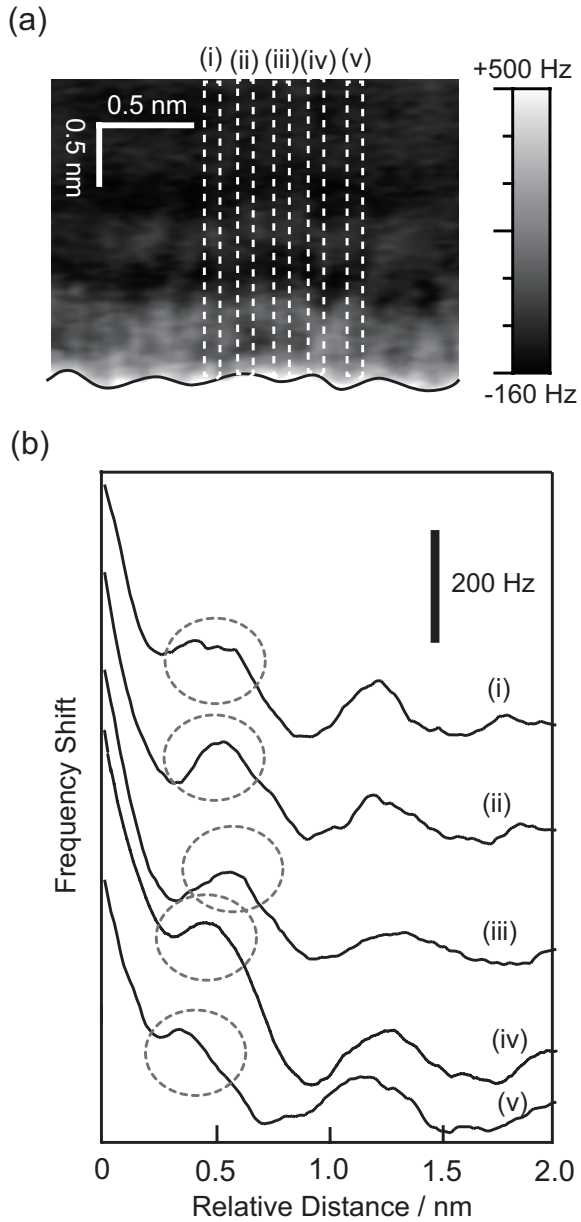

Figure 5.16 (a) A Δf distribution cross-sectional to the mercaptoundecanoic acid SAM immersed in 2-methyl-2-butanol. Cantilever oscillation amplitude: 0.1 nm. (b) Averaged Δf-distance curves. Each curve was obtained by averaging 4 curves in each area of (i) to (v). The curves are vertically shifted so as to not overlap. The Δf-modulated region is marked with a dotted circle.

5.6.3 Interfacial structures of secondary alcohol over COOH-terminated SAM

The author further determined the cross-sectional distributions over secondary alcohol, 2-octanol. Interfacial structure of 2-octanol showed mid-localized structure between the primary and tertiary ones as shown in Fig. 5.17. The mixture of modulations was quite less possible to be due to the artifact of measurement, because the layered and site-specific modulations appeared along the same sequence of one vertical scan. The distribution seems to contain the mixture of the laterally uniform layered modulations and site-specific ones. Here the author focused on the qualitative tendency of the lateral locality of the cross-sectional distribution. The limited coordination of the OH group may inhibit the site-specific structuring of the surrounding molecules, and in this case, the inhibitory effect should be greater than 1-octanol but smaller than 2-methyl-2-pentanol. This result supports the current suggestion that the interfacial structure of alcohol is sensitive to steric hinderance around the alcoholic OH.

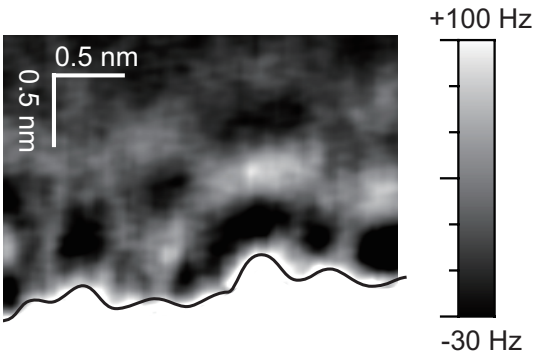

Figure 5.17 A Δf distribution cross-sectional to the mercaptoundecanoic acid SAM immersed in 2-octanol. Cantilever oscillation amplitude: 0.1 nm.

5.6.4 Interfacial structures of 1-octanol over OH-terminated SAM

In this subsection, interfacial structure of a alcohol was determined over OH terminated-SAM in order to examine the hydrogen bonding ability of OH end-group embedded on the SAM. Figure 5.18(a) shows the cross-sectional Δf distributions in 1-octanol over the OH-SAM. Δf was modulated from the negative to positive at 0.3-0.4 nm over the topographic windings as depicted in Fig. 5.18(b). Though the modulations are quite weak compared to the COOH-terminated SAM interface, it can be clear to see the Δf modulations as uniform layers along the lateral coordinate. In contrast of the COOH-terminated SAM interface, even primary 1-octanol was not localized at a certain lateral site of hydrophilic OH-terminated SAM. The uniform layer demonstrated the absence of an epitaxial relation across the interface, which suggested that even the terminal OH of 1-octanol only interacted weakly with the OH end-groups of the SAM.

As mentioned in 5.5, Δf distribution of interfacial water showed the site-specific relationship to the terminal OH group of the SAM. A molecular dynamics simulation [15] predicted hydrogen-bonded ethanol on an OH-terminated SAM. The author ascribes the laterally uniform distribution observed in this study to van der Waals interaction of the octyl chain and monolayer. The bridge bonded of 1-octanol to adjacent OH end-groups should be unfavorable in this case, probably because the large separation of the end-group, 0.5 nm, relative to the size of the alcoholic OH group. The interaction of stacking the octyl chain was thus superior to that between terminal OH of 1-octanol and the OH end-groups of the SAM. The thickness of the first octanol layer was estimated to be 0.6 nm with the distance from first minimum to second minimum. This length was comparable to those of the tertiary alcohols over COOH-SAM as well as *n*-alkanes over the CH_3-terminated monolayer. The alkyl chain is thus expected to be parallel to the SAM surface. The parallel orientations are driven by van der Waals energy gain, as described in Chapter 4. Flexibility of the hydrogen bond capable end-groups should be needed to make a strong interaction enough to pin the liquid molecules on a certain site of the SAM.

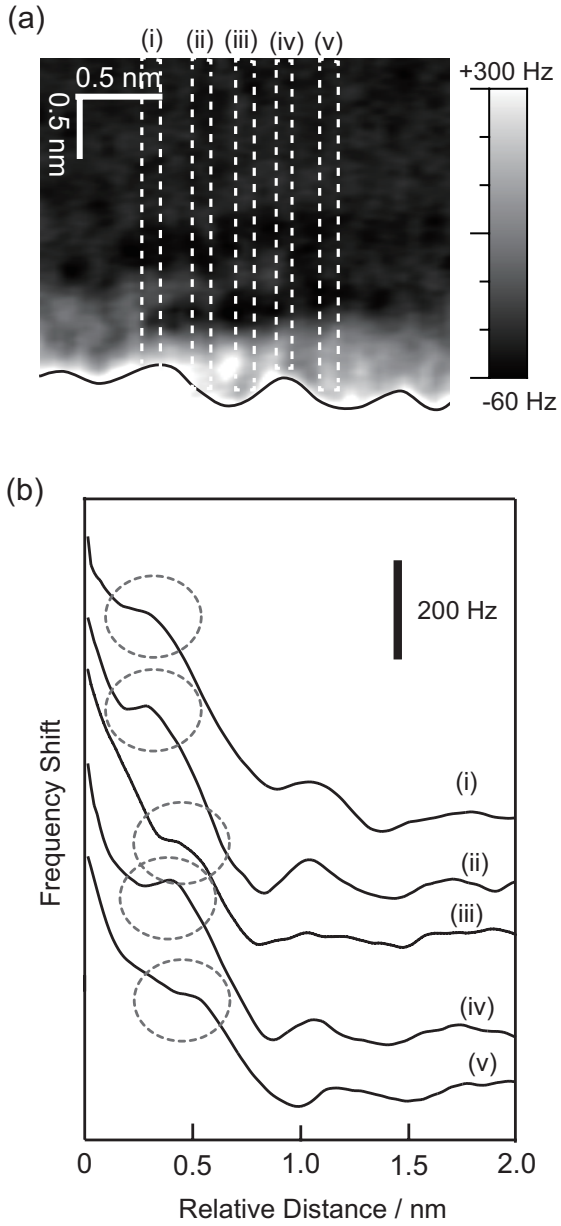

Figure 5.18 The mercaptoundecanol SAM immersed in 1-octanol. (a) Δf distribution cross-sectional to the monolayer. Cantilever oscillation amplitude: 0.1 nm. (b) Averaged Δf-distance curves over a topographic protrusion or groove. Each curve was obtained by averaging 5 curves in each area of (i) to (v). The curves are vertically shifted so as to not overlap. The Δf-modulated region is marked with a dotted circle.

5.6.5 Interfacial structures of carboxylic acid over OH-terminated SAM

The site-specific modulations were found at COOH-terminated SAM and a primary alcohol containing OH end-group. To investigate the possibility that the site-specific distributions depended on interaction between the OH and COOH, the cross-sectional Δf distrubution was further determined at the interface of octanic acid and the OH-terminated SAM as shown in Fig. 5.19. As 1-octanol interface of the OH-terminated SAM, the modulations independent to lateral topographic windings were found on the distribution. This suggested that the reduced accessibility of the buried OH end-group caused to weaken the interaction between the OH end-group and the interfacial liquid carboxylic acid.

Another remarkable finding is that the separation in octanoic acid was significantly smaller than the other organic compounds. Carboxylic acid can easily make a hydrogen-bonded dimer. When the dimers stack on the SAM, their alkyl chains may be laminated alternatively even though the dimers could freely rotate in the layer. The alternative stacking gives the peaks in the density distribution split into double with position of one dimer's center of mass, which would present the separation of 0.3 nm, that is half of the size of turnback ethylene units.

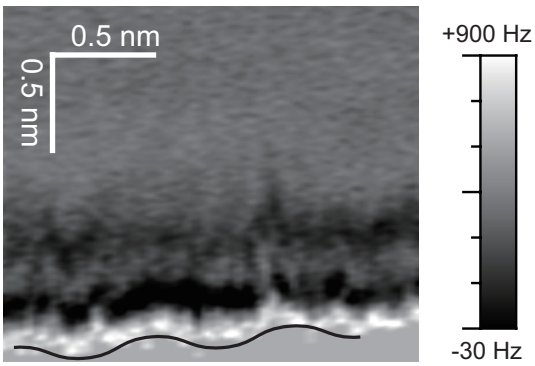

Figure 5.19. Δf distribution cross-sectional to the mercaptoundecanol SAM immersed in octanoic acid. Cantilever oscillation amplitude: 0.1 nm.

5.7 HOPG/decanol interface

As discussed in 5.6, the observed presence and absence of the epitaxial relationship were interpreted with the competition of hydrogen bond and van der Waals interactions. Decanol/HOPG interface which mentioned in 3.5 is another example appropriate to provide a further insight of such contributing factors in structuring interfacial liquids. Especially in the case of adsorbed decanols on HOPG, both inert alkyl and hydrogen-bond capable OH groups are exposed to liquid decanol. Such surface chemical heterogeneity should emphasize the competing of two interactions in structuring interfacial liquids.

In the beginning, the author defines those adlayers as the two types in this section. The adlayer solidly fixed to the HOPG surface was called as "adsorbed lamella," which cannot be excluded by the tip even when the force applied to the tip, in this case, exceeded +300 Hz, where the clear topography of the molecular adlayer was obtained as shown in Fig. 3.12. On the other hand, the weak structured layer which can be excluded by the tip, but can be distinguished with bulk liquids in an AFM observation, defines as "solvation layer." Here the author focused on the structure of solvation layers.

In order to determine the structure of solvation layer, two-dimensional Δf distributions were obtained cross-sectional to the HOPG surface. Figure 5.20 presents the Δf distributions obtained over the decanol adlayers as soon as after obtaining the normal topography of Fig. 3.12(b) in Chapter 3. The distributions of Figs. 5.20(a) and (b) are cross-sections normal to each other. In the bottom of the distributions, the protrusions of the brightest region periodically appeared along the trace. The protrusions were appeared in crossing protruded rows on topography of the adsorbed lamellae. The relationship of the bottom trace to the topographic image is described in Fig. 3.14(a) and (b). Based on the separation of the grooves, which was 1 nm in Fig. 5.20(a) and 5 nm in Fig. 5.20(b), the two cross-sectional images can be fitted in the topography as shown in the illustration of Fig. 5.20(c); Fig. 5.20(a) was obtained perpendicular to the molecular lamella, whereas Fig. 5.20(b) was along the lamella, but a bit oblique.

A narrow-area Δf distribution of the same cross-section in Fig. 5.20(a) was further determined as shown in Fig. 5.20(d). Figure 5.20(e) presents Δf-distance curves

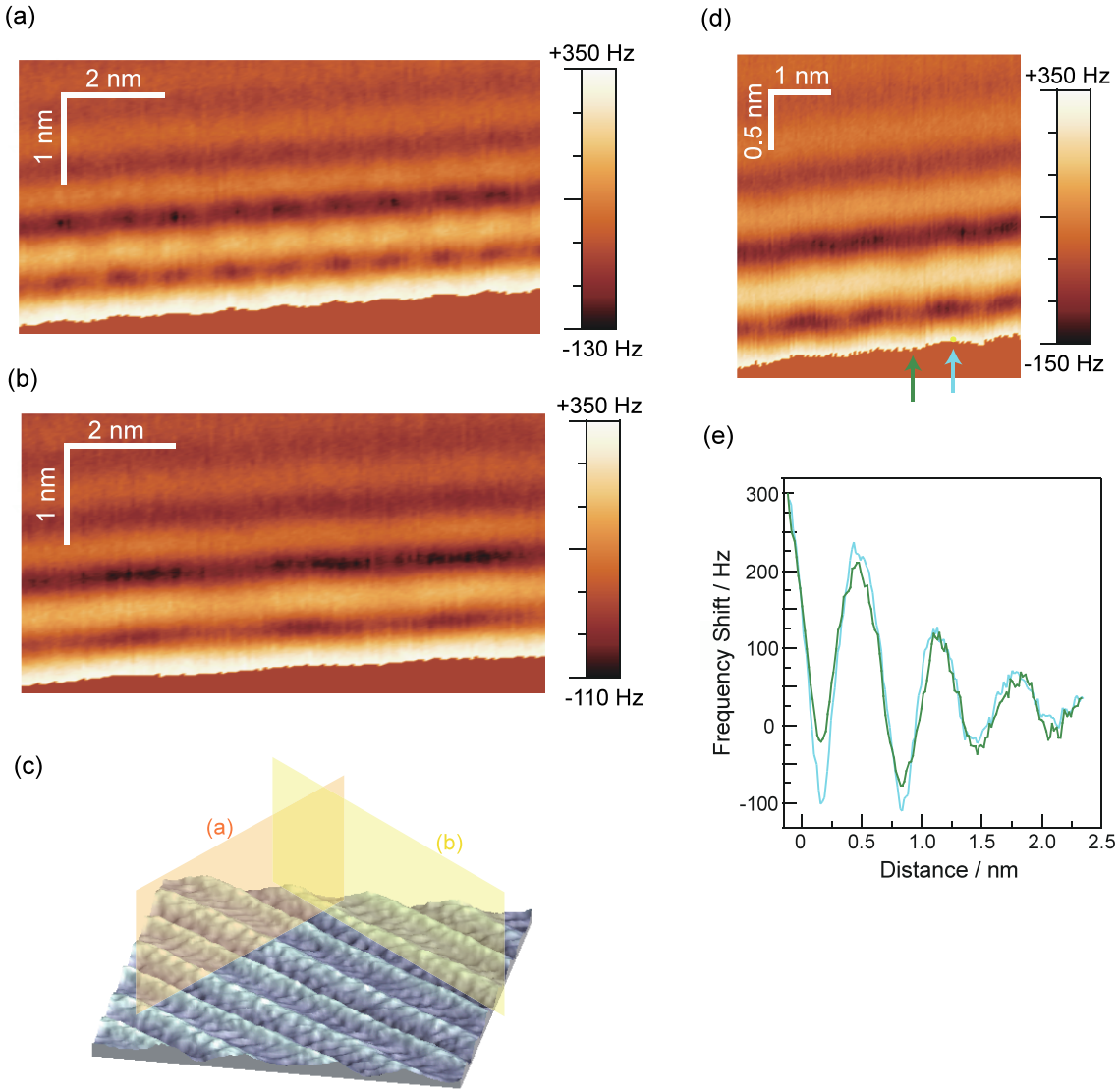

Figure 5.20. (a,b) Two-dimensional Δf distributions over adsorbed decanol lamellae on HOPG. Images (a) and (b) were acquired cross-sectional to each other. Amplitude 0.1 nm. (c) Schematic illustration of the acquired planes (a) and (b) superscripted on topography of the adsorbed lamellae. (d) A zoomed image of (a). (e) Δf-distance curves over a topographic groove (green) or protrusion (blue) extracted along the line indicated by arrows in (d).

depicted the topographic protrusion or groove indicated by the arrows in Fig. 5.20(d).

First, the author discusses the vertical distribution. The frequency shift was oscillated in both curves, and local maxima appeared at 0.5, 1.2 and 1.8 nm of the distance. The zero of the vertical distance defines here as the Δf was exceeded +300 Hz. The oscillations of Δf appeared as dark-to-bright changes along the vertical coordinate in the Δf distributions. As discussed in previous sections, the Δf oscillation is related to the enhancement or depression of the density of decanol molecules. Stimulated localization of the molecules attributed the enhanced oscillation of Δf (force.) As described in Chapter 4, the separation of 0.6 nm was common in *n*-alkanes that lay with their molecular axis parallel to the surface, which indicated that the parallel orientation was preferable in this system. Since the number of atoms in contact with the neighbor molecules is maximized per molecule in parallel orientation, the total energy should be accordingly minimized when van der Waals force is dominant interaction in a case of between the alkyl chains of alcohols. Stacking of alkyl chains attributed to construct the vertical structure of solvation layers.

Second, the author discusses the lateral distribution. The Δf-distance curves of Fig. 3.14(e) showed that the Δf contrast of the first and second oscillations was enhanced over a topographic protrusion (blue) relative to a groove (green), and the first oscillation was strongly enhanced than the second one. The enhancement of oscillation can be found in the Δf distribution as contrast changes along the lateral coordinate. The dark-bright-dark changes in the vertical coordinate enhances over the topographic protrusion whereas depressed over the topographic grooves. Such contrast changes are seen in the Δf distribution as if dark rods lay along the surface. The topographic protrusions were corresponding to the terminal methyl groups of the adsorbed molecules. This indicates that the decanol molecules prefer to pile over the adsorbed lamellae rather than the grooves between the lamellae.

The lateral localization was subjected to the interaction to adsorbed lamellae. When the liquid decanol locates on top of the adsorbed molecule, the decanol liquid can form hydrogen bond to the OH of the adsorbed molecule, in addition to the maximized van der Waals gain between the alkyl chains. This scheme is illustrated in Fig. 5.21. Such hydrogen bond should attribute to the stability of on-top localization of solvation layer. This is consistent with the interfacial structures of polar liquid over the hydrophilic SAMs as discussed in previous sections.

On the other hand, the cross-sectional distribution of (b), which was acquired orthogonally to (a), presented no contrast changes across an adsorbed lamella. This suggests the uniform density distribution over the lamellae. Even when the solvating molecule is on the hollow site of the adsorbed molecules intra lamellae, hydrogen bond toward the OH residue of adsorbed lamellae should remain, which contributed to stability on the lamellae. The van der Walls gain is also expected to remain near that on top of the molecules, due to the closer distance of the neighbor molecules. On the other hand, in crossing the lamellae, the molecules translate via an unstable state on the grooves between the lamellae as suggested in Fig. 5.21.

In addition, dissipation of the lateral localized contrast was found to be different from that of vertical one. The lateral localization was scarcely acknowledged even in the third solvation layer, whereas forth or more solvation layers were appeared along the vertical coordination. The different constraint of the molecule in vertical and lateral dimension supports the suggestion of different contribution of interaction for vertical and lateral structures of interfacial decanols. The author assumes that the vertical structure mainly attributed to the stacking of alkyl chains and lateral constraint mainly attributed to specific hydrogen bonds between decanol molecules. Anisotropic hydrogen bond should be sensitive to geometry of the OH end-group. Increasing mobility of the solvated decanol molecules with distance from the surface can cause rapid attenuation of hydrogen-bond strength. On the other hand, since van der Waals interaction is isotropic, molecular stacking along the vertical coordinate should remain at long distance.

The result was a reasonable example which showed that the total structure of the interfacial alcohols were determined with the competition of these two interactions.

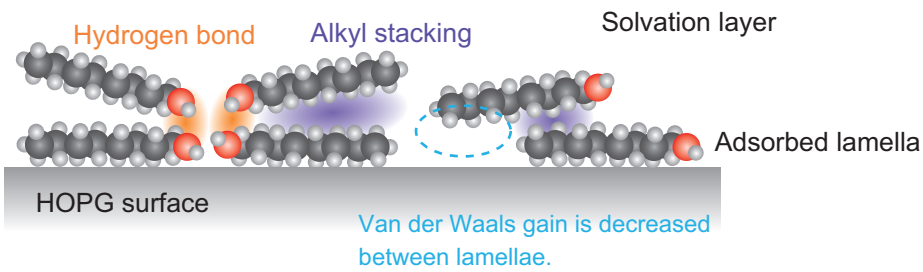

Figure 5.21. Schematic illustration of decanol/HOPG interface.

5.8 Conclusions

In this chapter, the topography and interfacial structure of liquids were determined for OH-terminated mercaptoundecanol SAM and COOH-terminated mercaptoundecanoic acid SAM.

In an aqueous solution, both the SAMs presented the intrinsic ($\sqrt{3}\times\sqrt{3}$) structure of the adsorbed thiolate monolayers. On the other hand, in an alcohol, the COOH-terminated SAM made the hydrogen-bond pairs between adjacent COOH groups, whereas the OH-terminated SAM showed the intrinsic superstructure. Hydrogen bonds of the end-group have a key role in stability of the end-group. Creation and rapture of hydrogen bonds among the COOH end-groups resulted in the poor resolved topography.

The cross-sectional structure of interfacial water was sensitive to the composition of hydrophilic end-groups at the interface. Water density distribution was modulated between adjacent OH end-groups of a mercaptoundecanol monolayer, as opposed to on top of the COOH and COO^- end-groups of a mercaptoundecanoic acid monolayer. The density distributions were insensitive to the presence of electrolytes KCl and NaCl, and to potassium monohydrogen phthalate. There was no qualitative sign of tip-induced confinement of water.

The cross-sectional structure of interfacial liquid is also sensitive to the hydrogen bonding ability of the liquid molecules. The primary alcohols presented epitaxial relationship to a COOH-terminated SAM surface via the hydrogen bond between terminal OH and COOH end-group. On the other hand, laterally uniform liquid layers were present in the obtained with the tertiary alcohols. Over an OH-terminated SAM even primary octanol showed a laterally uniform liquid layer. The observed presence and absence of the site-specific relationship were interpreted with the competition of two interactions; hydrogen bond and van der Waals interaction. The former interaction is site-specific to make a laterally heterogeneous structure of interfacial liquids, while the latter favors laterally uniform liquid layers. The primary alcohols provided hydrogen-bond dominant examples when interfaced with COOH end-groups. The hydrogen-bond should be weakened in the bulky alcohols because the bulky end-group reduced accessibility to the hydrogen bond active end-group. As a result, van der Waals term is dominant with the tertiary alcohols. Steric relationship between the hydrogen

bonding capable groups of liquid and solid surface was important consequences to build the liquid structure at the interface.

The competition of the two different interactions clearly observed in the interfacial structure at HOPG/decanol interface. Lateral localization was scarcely acknowledged even in the third solvation layer, whereas forth or more solvation layers were appeared along the vertical coordination. Lateral constraint due to hydrogen bond is weaker than alkyl stacking along the vertical coordinate in this system.

Such intermolecular interaction is also a key factor in chemical or biological reaction occurred at solid-liquid interfaces. It is hoped in future that such an analysis of competitive solvent-substrate interaction through the sub-nanometer scale visualization of heterogeneous interface, provide milestones for molecular designs improving efficiency and selectivity of catalysts or medicines.

References in Chapter 5

[1] T. Fukuma, M. Kimura, K. Kobayashi, K. Matsushige and H. Yamada, *Rev. Sci. Instrum.* 76 (2005) 053704.

[2] J. C. Love, L. A.Estroff, J. K. Kriebel, R.G. Nuzzo, and G.M. Whitesides, *Chem. Rev.* 105 (2005) 1103.

[3] L. H. Dunois and R. G. Nuzzo, *Rev. Phys. Chem.* 43 (1992) 437.

[4] A. Ulman, *Chem. Rev.* 96 (1996) 1533.

[5] G. M. Whitesides and P. E. Laibinis, *Langmuir* 6 (1990) 87.

[6] O. Gershevitz and C.N. Sukenik, *J. Am. Chem. Soc.* 126 (2004) 482.

[7] E. L. Smith, C. A. Alves, J. W. Anderegg, and M.D. Porter, *Langmuir* 8 (1992) 2707.

[8] A. L. Morales-Cruza, R. Tremonta, R. Martíneza, R. Romañachb, and C. R. Cabrera, *Appl. Surf. Sci.* 241 (2005) 371.

[9] P. Maksymovych, O. Voznyy, D. B. Dougherty, D. C. Sorescu and J. T. Yates Jr., *Prog. Surf. Sci.* 85 (2010) 206.

[10] L. Strong and G. M. Whitesides, *Langmuir* 4 (1988) 546.

[11] C. E. D. Chidsey and D. N. Loiacono, *Langmuir* 6 (1990) 682.

[12] C. A. Alves, E. L. Smith and M. D. Porter *J. Am. Chem. Soc.* 114 (1992) 1222.

[13] S. M. Mendoza, I. Arfaoui, S. Zanarini, F. Paolucci and P. Rudolf, *Langmuir*, 23 (2007) 582.

[14] R. G. Nuzzo, L. H. Dubois, and D. L. Allara, *J. Am. Chem. Soc.* 112 (1990) 558.

[15] M. Sprik, E. Delamarche, B. Michel, U. Roethlisberger, M. L. Klein, H. Wolf and H. Ringsdorf, *Langmuir* 10 (1994) 4116.

[16] W. H. Robertson, E. A. Price, J. M. Weber, J.-W. Shin, G. H. Weddle, and M. A. Johnson, *J. Phys. Chem. A* 107 (2003) 6527.

[17] X.-B. Wang, B. J.-Cwiklik, C. Chi, X.-P. Xing, M. Zhou, P. Jungwirth, and L. S. Wang, *Chem. Phys. Lett.* 477 (2009) 41.

[18] M. W. Feyereisen, D. Feller, and D. A. Dixon, *J. Phys. Chem.* 100 (1996) 2993.

[19] M. Harada and M. Tsukada, *Phys. Rev. B* 82 (2010) 035414.

[20] M. Watkins, M. L. Berkowitz and A. L. Shluger, *Phys. Chem. Chem. Phys.* 13 (2011) 12584.

[21] G. B. Kaggwa, P. C. Nalam, J. I. Kilpatrick, N. D. Spencer, and S. P. Jarvis, *Langmuir* 28 (2012) 6589.

[22] V. Franz and H.-J. Butt, *J. Phys. Chem. B* 106 (2002) 1703.

[23] L. P. Kuhn, *J. Am. Chem. Soc.* 74 (1951) 2492.

[24] C. C. Corey, A. Rice, and M. A. Suhm, *J. Phys. Chem. A* 110 (2006) 9839.

[25] P. G. Kusalik, A. P. Lyubartsev, D. L. Bergman, and A. Laaksonen, *J. Phys. Chem. B* 104 (2000) 9533.

[26] Y. T. Wang, K. Hill, and J. G. Harris, *J. Chem. Phys.* 100 (1994) 3276.

[27] R. Lim and S. J. O'Shea, *Phys. Rev. Lett.* 88 (2002) 246101.

Chapter 6: Interfacial Structure of Water Related to Wettability on Metal Oxide surfaces

6.1 Introduction

6.1.1 Wettability on surface

In the previous chapters, the structures of liquids at solid-liquid interface are discussed in terms of their formative factors such as chemical properties of solids and liquids. The structure of interfacial liquids is thought to determine their wetting properties and underlies various phenomena known as hydrophilicity and hydrophobicity. Such properties often describe the interaction of liquids to surfaces. The study of interfacial liquid structure continues to be a subject of great interest and numerous studies are devoted to it. [1,2] In this chapter, surface wettability for water is discussed with microscopic approach. Molecular-scale understanding of interfacial water, which probably determined most of the interfacial wetting properties, is important for the discussion. As discussed in Chapters 4 and 5, structures of interfacial liquids are sensitive to surface functional groups. Wetting properties are also modified by the surface chemical reforming. The microscopic interfacial liquid structure thus should relate to the macroscopic wetting, and analysis of them should be essential for understanding the wetting mechanisms. Here, cross-sectional Δf distributions to the metal oxide surfaces, such as mica, alumina, titania, on which different wetting properties are exhibited for water, are compared to discuss the relationship of microscopic interfacial water structure to macroscopic wetting properties on the surface.

6.1.2 Superhydrophilicity on TiO_2

One of the applications in controlling wetting property is achieved using superhydrophilicity of titanium dioxide, TiO_2. TiO_2 has been widely used in photofunctional applications including photoelectrodes, photocatalysts, and hydrophilic coatings, since the pioneering work of Honda and Fujishima. [3] The contact angle of a water droplet is sensitive to ultraviolet (UV) light irradiation on TiO_2 surfaces. The hydrophilic character of a TiO_2 surface is enhanced by irradiation and the contact angle is reduced to zero. [4,5] Two possible mechanisms of the photoinduced enhancement have been proposed. One involves organic contaminants, which make the surface hydrophobic, being decomposed in photocatalytic reactions driven by UV light. The other mechanism is based on the UV-induced formation of hydroxyl (OH) species on TiO_2 surfaces. [6] As mentioned in subsection 6.1.1, microscopic structure of interfacial water can also become a clue to the mechanism of superhydrophilicity. In this chapter, the structure of the aqueous solution-TiO_2 interface was investigated before and after UV irradiation, aiming to discuss the molecular mechanism of the characteristic superhydrophilicity of TiO_2.

6.2 Experiment

Substrates were prepared in the same manner described in section 3.2. An α-Al_2O_3(01-12) wafer ($10\times10\times0.5mm^3$, Shinko-Sha) was washed with concentrated nitric acid, ultrasonically rinsed with pure water, dried in a N_2 flow, and calcined in air at 1273 K for 12 hours. A rutile TiO_2(110) wafer ($10 \times 10 \times 0.3$ mm^3, Shinko-Sha) was calcined in air at 1273 K for 12 hours. The calcined wafer was fully oxidized and transparent for visible light. The wafers were cooled in air, immediately placed in a homemade liquid AFM cell as illustrated in Fig. 2.8. Imaging solutions were prepared by Millipore water.

6.3 Cross-sectional force distribution over metal oxides at aqueous interface

In this section, cross-sectional structures of interfacial water were discussed in terms of its relationship to macroscopic wettability of surface. The cross-sectional Δf distribution was determined to compare on three metal oxide surfaces: mica, Al_2O_3, and TiO_2. The substrates showed different contact angle of water droplet as shown in Fig. 6.1(a)-(c). Mica was the most hydrophilic and TiO_2 was the most hydrophobic of the three. The cross-sectional Δf distributions over the three metal oxide surfaces are presented in Fig. 6.1(d)-(f). As observed over hydrophilic OH- and COOH-terminated SAM, site-specific modulations were found on most hydrophilic mica. On the other hand, organized water layers were less observed on Al_2O_3, and TiO_2 surface, exhibited less hydrophilic. The author considers that the organized water layers relate to hydrophilic character of the metal oxide surfaces.

Hydrophilicity is thought to be determined by mainly two factors: chemical affinity to water and structure (or roughness) of the surface. Since all the three oxide surfaces are ionic crystals though the chemical composition is different, chemical affinity is expected to be similar. The author thus supposes that the different wetting behavior should come from the different surface structures.

Wettablity on hubbly surface has been analyzed by Wenzel [7] or Cassie-Baxter theory. [8] The former supposed that the roughness of the surface causes to increase the effective surface area facing to the liquids. Then the contact angle (θ) is given by,

$$\cos\theta = \frac{R(\gamma_{SA} - \gamma_{SL})}{\gamma_{LA}} \quad (6.1)$$

where γ is surface tension (subscripts are represent the interface; S: solid, L: liquid, A: air) and R is the enhanced ratio of the effective surface area to the apparent. The equation indicates that the hydrophilic or hydrophobic chemical affinity is enhanced by the roughness. On the other hand, Cassie-Baxter theory supposed that the roughness of the surface can be interpreted as the superposition of the small area where different wetting properties exhibit. In this way, the contact angle (θ) is given by,

$$\cos\theta = \sum_k f_k \cos\theta_k \quad (6.2).$$

Here f_k is a ratio of the area k that presents contact angle given by $\cos\theta_k$.

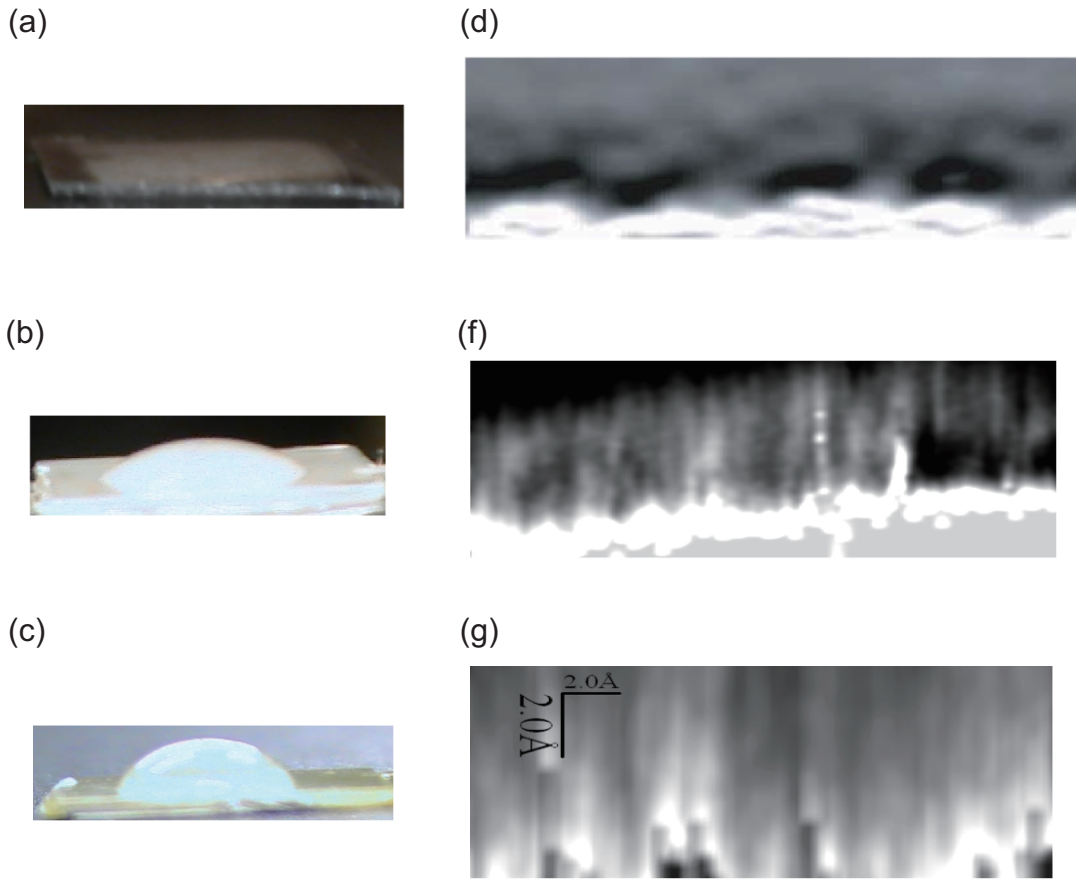

Figure 6.1: (a-c) Water droplet on the metal oxide surfaces. (d-f) Cross-sectional *Δf* distributions at aqueous interfaces of the metal oxide surfaces. Each surfaces were immersed in KCl solution. Cantilever oscillation amplitude: (d) 0.1 nm, (e) 0.2 nm, (f) 0.7 nm. Scale is adjusted in the three distribution images.

The current AFM results suggested that nanostructure of the surface can also be caused to the stability of adsorbed water. Mica presents an extremely flat surface owing to the planer layer of $AlSi_3O_{10}(OH)_2$ where the cations and anions are arranged in a hexagonal lattice, whereas Al_2O_3, and TiO_2 present atomically hubbly surface due to protruded oxide terminations as mentioned in the diffraction [9] and simulation study. [10] This is clearly seen in the schematic illustration of the surfaces in Fig. 6.2. As

discussed in the previous chapter, hydrogen bond is an important contribution for structuring interfacial water and steric environment around the bond affects the site-specific adsorption due to its anisotropic aspect. Solvent water molecules are expected to have no impediments to access to the flat mica surface. Thus the water can be hydrogen-bonded toward hydrophilic end-groups on the surface to form ordered layers. On the other hand, atomically hubbly Al_2O_3, or TiO_2 surface restricts solvent water to access to the hydrophilic end-groups, which causes to the less organized water layers observed in this study. Note that another factor can attribute to the significant hydrophobic property of TiO_2 surface, which is discussed in the following section.

What is stressed here is that the even atomic roughness is contributed to the stability of the adsorbed water layer. This is beyond the scope of the conventional approaches to analyze wettability as mentioned above. The quantitative relationship between the stability of adsorbed water and atomistic structure are important issue for future studies, which would require the simulation analysis. These results suggested that the structure of interfacial water may directly link to surface wettability. Hence these represent the promising ability of the FM-AFM for the future realization of deducing to molecular scale adsorption behavior for guidelines controlling the wettability.

(a) Mica

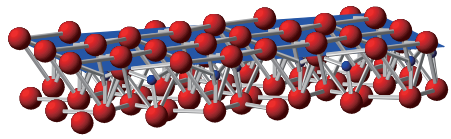

(b) TiO_2(110)

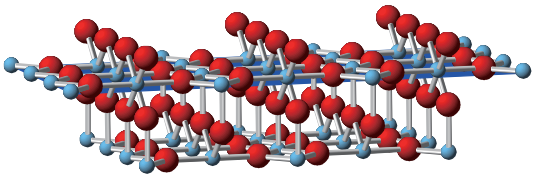

Figure 6.2: Schematic illustration of (a) mica and (b) TiO_2 surface.

6.4 Topography of TiO_2 in aqueous solution under dark and UV irradiated condition

In this section, another example of wettability analysis is presented: TiO_2 surface related with its superhydrophilicity. To trace the origin of significant hydrophobic property of TiO_2 surface as shown in Fig. 6.1, topography and Δf-distance curves were determined in dark (hydrophobic) and after UV irradiation (hydrophilic). Figure 6.3 shows the constant Δf topography of the prepared TiO_2 (110) in the 1 M KCl aqueous solution, with a cross-sectional height profile. An intrinsic step of TiO_2(110), which is

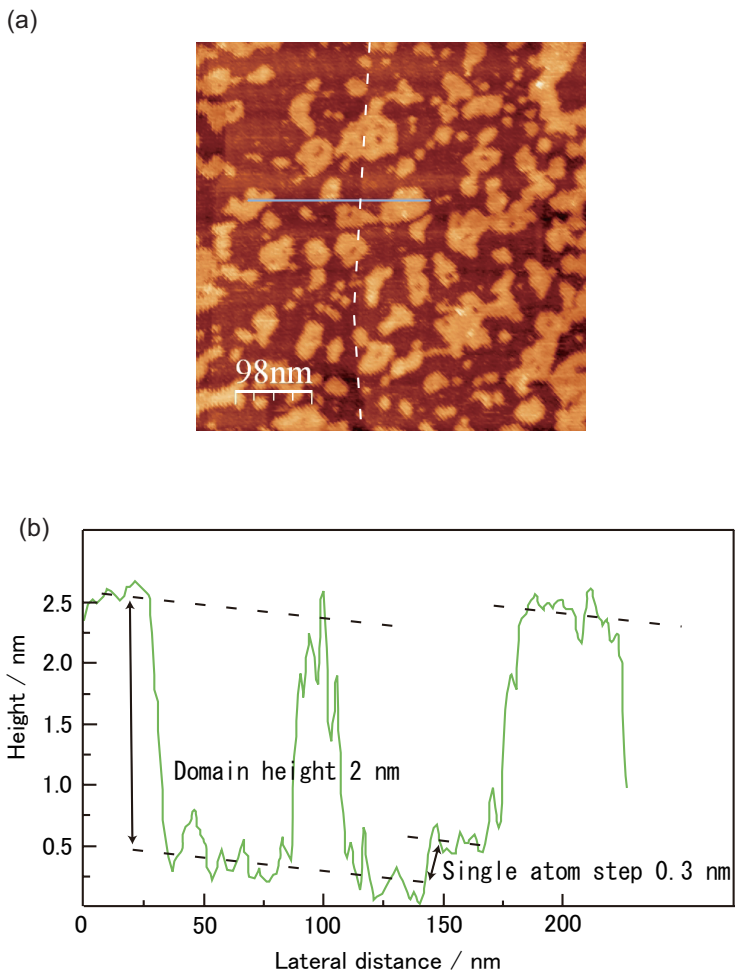

Figure 6.3. (a) Constant frequency-shift topography of a TiO_2 (110) surface immersed in 1M KCl solution. Δf setpoint: 300 Hz. Cantilever oscillation amplitude: 6 nm. (b) A cross-sectional height profile along the green line on the image (a).

0.33 nm in height [11], was observed in the middle of the image, marked with a broken line. The characteristic domains were found on the terrace whose height was uniform at 2 nm. The domains were also found to be extended on the terrace. Figure 6.4 shows a series of the topographic images. Domains appeared in Fig. 6.4(a), extended Fig. 6.4(b) to (c), and almost covered the TiO_2 surface in Fig. 6.4(d). From these consecutive images, the rate of domain extension was estimated as 10 nm min^{-1}. The nucleation and extension of the domains were insensitive to the TiO_2 step underneath.

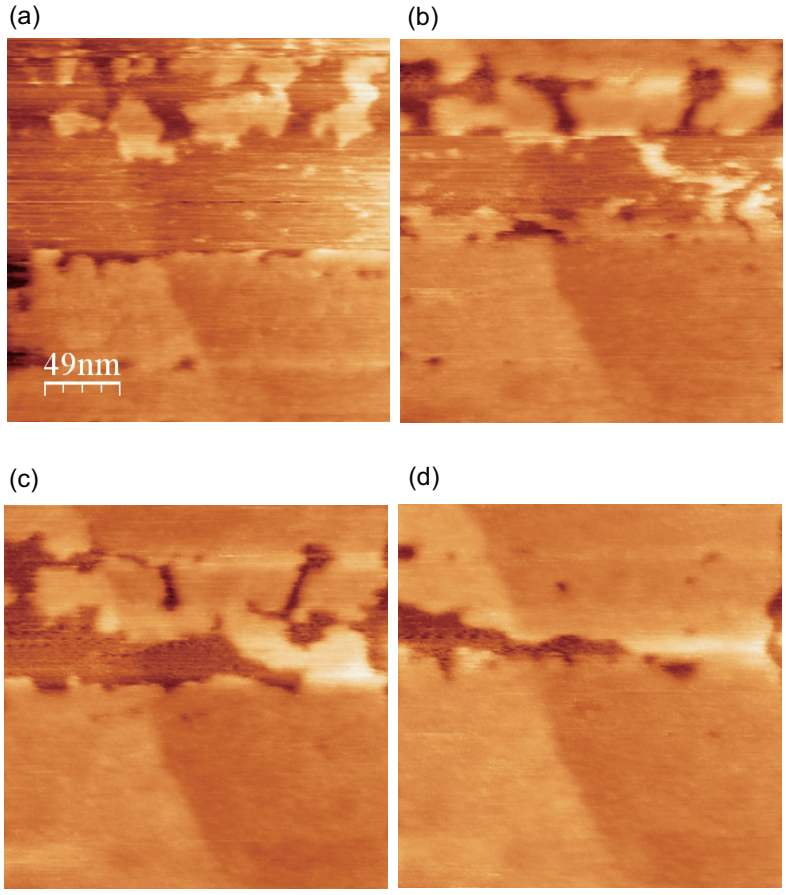

Figure 6.4. Constant frequency-shift topography of a TiO_2 (110) surface immersed in KCl solution. Four images shown in (a) to (d) were observed in intervals of 3 min. Δf setpoint: 300 Hz. Cantilever oscillation amplitude: 6 nm.

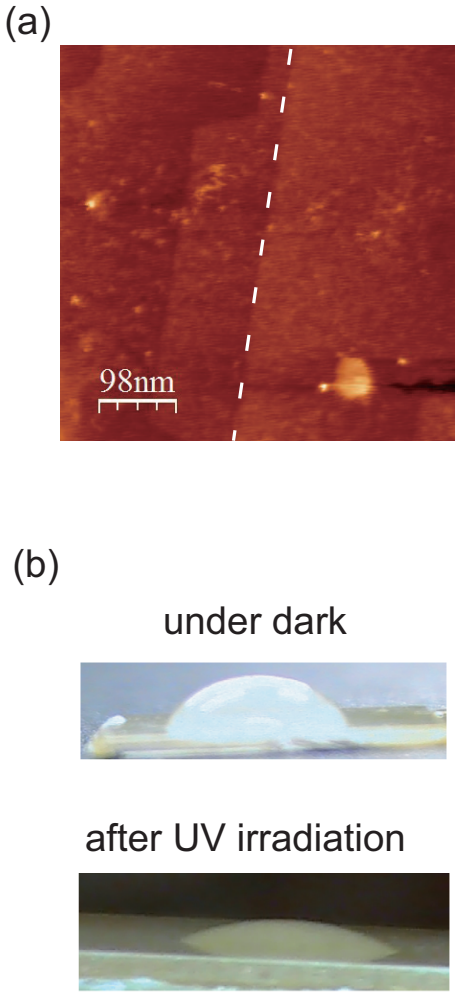

Figure 6.5. (a) Constant frequency-shift topography of a TiO_2 (110) surface after UV irradiation Imaging scan was demonstrated in the KCl solution. Some of the steps are marked with a dotted line. Frequency shift (Δf) = 300 Hz. Cantilever oscillation amplitude: 3 nm. (b) A snapshot of a water droplet on TiO_2 (110) surface under dark and after UV irradiation.

However, the domains disappeared after UV irradiation (360 nm, 7.5 mW/cm^2, 7 h) and the step-terrace structure was clearly observed as seen in the topography of Fig. 6.5. With the UV irradiation, water contact angle was significantly decreased as shown in Fig. 6.5(b).

The chemical composition of the domains is unclear, but two possible interpretations are proposed. Organic contaminants or accumulated ionic solutes are most probable candidates. In the former interpretation, hydrophobic surface in dark condition is due to the adsorption of organic contaminants, which is a component of the domains. Disappearance of the domain after UV irradiation makes the surface hydrophilic. This is reasonable because organic contaminants covered on the surface should be decomposed by photo catalytic reaction on TiO_2. Even though the imaging solution was prepared by purified water, the organic molecules could be dissolved in the solution because the measurement was demonstrated in an ambient condition. Adsorption of dichloroethane (DCE) on TiO_2 powder from water was investigated as a model of organic contaminants. [12] This study indicated 70 % of the surface covered with DCE monolayer. Considering the previous result, organic contaminants in imaging solution could well form the observed domains.

Another possibility of origin of the domains is precipitates of electrolyte solution. The solubility of KCl is 3.4 mol l^{-1} in water at room temperature, which is higher than the bulk concentration of the solution. Electrolyte precipitates can be produced at the interface when the local concentration of KCl exceeds the solubility. The ionic solute may be concentrated in the electric double layer of the solution facing the TiO_2 surface. Charge state and electric double layer on the surface could be affected by UV irradiation, which cause to eradicate the domains.

Such domains characteristically observed on TiO_2 surface. Figure 6.6 presents the constant frequency-shift topography of the calcined α-Al_2O_3(01-12) wafer observed in the 1M KCl aqueous solution. Steps appear from the top right to bottom left of the image. The height of the steps was 0.3 nm reproducing the minimum repetition length of the Al_2O_3 crystal along the (01-12) direction. The steps and terraces were stable under repeated scans with no sign of corrosion or domain nucleation.

Atom-scale features were not resolved on the terraces. A periodic, hexagonal lattice arrangement was observe on an α-Al_2O_3(0001) wafer in water using a contact-mode AFM. [13] There were bumps over the terraces. The topographic height of the bumps

was less than 0.1 nm. This number is too small to assign the bumps into some chemical species at the surface. Instead, the authors assume that the bumps appeared from some errors in the constant frequency-shift feedback. The uniform height domains which were found on the TiO_2 surface, did not appear even in the consecutive scans. Clear topography without the domains was also observed on mica surface in an aqueous solution. These suggest that the domains are originated from nature of TiO_2 surface. High adsorption activity of ionic or organic solutes should attribute to the hydrophobic property on the TiO_2 surface. Identifying the chemical composition of the domains is an important issue for future studies.

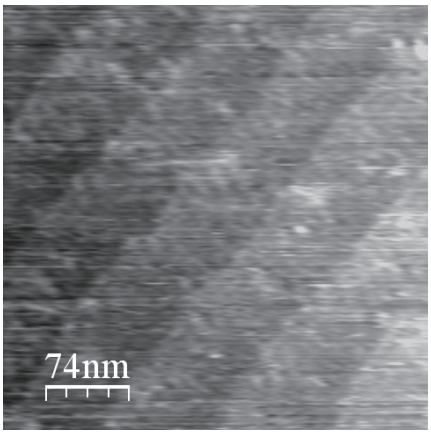

Figure 6.6. Constant frequency-shift topography of an α-Al_2O_3 (01-12) surface immersed in 1 M KCl aqueous solution. Δf setpoint: +800 Hz. Cantilever oscillation amplitude: 0.8 nm.

6.5 Δf-distance curves on at aqueous interface of TiO_2 under UV irradiation

UV irradiation should affect not only the topography but also interfacial structure of water. The structural changes of interfacial water are to be considered when hydrophilic property was induced on the surface by UV irradiation. For such purpose, *Δf*-distance curves at an aqueous-TiO_2 interface were acquired under dark and UV irradiated condition as shown in Fig. 6.7. Oscillatory modulations were appeared at 0.4 and 0.7 nm after irradiation, whereas only single modulation was found before irradiation. This was consistent with the trend of water structure on metal oxide surfaces discussed in section 6.3. Also here hydrophilic property projected the multilayer formation of interfacial water. The density distribution of water by molecular dynamics simulation [10] presented double peaks on the hydroxylated (110) surface and single peak on the non-hydroxylated surface as shown in Fig. 6.8. Note that the peak at 0.2 nm above the non-hydroxylated is in consequence of the bridged oxygen of the surface, not of water. In terms of the curve feature, the *Δf*-distance curves before and after the irradiation are corresponded to the density distribution of non-hydroxylated and hydroxylated surface, respectively. After irradiation, hydroxyl groups are thus induced on the surface, which promotes the water structuring, as a result. This was consistent to the previous spectroscopic study [6] where hydroxyl groups on the surface were found to be increased after UV irradiation. The hydrophobic HOPG surface where no hydrophilic end-groups are expected to exist, also presented the single peak on the *Δf*-distance curve [14] as the surface in dark did. This suggests that increase of hydroxyl groups by UV-induced chemical reaction to the TiO_2 surface, possibly resulted in the multi-layer formation of interfacial water. However the contribution of disposal the domains covered on the native TiO_2 surface still cannot be precluded thoroughly. Identifying the chemical composition of the domains is just as a key to understand the whole mechanism of the hydrophilic transition of the surface.

The background decay of the *Δf*-distance curve also reflected the hydrophilic conversion by UV irradiation. As mentioned in Chapter 3, the background decay can be interpreted by the interaction of electric double layers [15], and the repulsive, double layer force exponentially decays with the distance from the surface as the equation (3.18). The best fit was achieved for the force curve before irradiation as,

$$F_z(z) = 0.583 \cdot \exp(-1.12 \cdot z / \mathrm{nm})\ [\mathrm{nN}] \quad (6.3)$$

The decay length is thus 0.9 nm, that is much longer than double layer decay length of concentrated electrolyte solution, typically less than 0.1 nm. Such long-range decay was common at interfaces between aqueous solution and hydrophobic surfaces such as hydrophobic trimethylsiloxane covered Si wafer. [16] The full-nature of the long-range decay has not yet revealed and still has been debated much. Some theoretical study suggested that the structured liquids could also provide the monotonic repulsive forces, which are possibly added to an oscillatory force modulation. [17-21] Still others suggested that the forces due to the structured liquid intimately connected to the double layer interaction and cannot be separated from each other, even though van der Waals and other interaction were additive on condition of DLVO theory. [22,23] The monotonic repulsive force also found between colloidal sillica surfaces in SFA [24] and colloidal probe AFM measurement. [25] It is largely insensitive to ionic conditions of aqueous electrolyte solutions and appeared in addition to the DLVO force. In these cases, hubbly surface of silica was possible to cause to sterically perturb the liquid layers, resulting in the monotonic repulsive force. In this case, the adsorbates on TiO_2 surface make the surface hubbly. The monotonic density distribution of interfacial water due to the steric perturbations may cause the additional repulsive force on the DLVO background, though the current AFM measurement is almost free from the confinement of the tip, in different condition that the confinement effect is significant in these early studies.

On the other hand, after UV irradiation, the double layer interaction was screened within less than 0.1 nm above the surface, and only van der Waals component may remain in the background terms. This is an ordinary behavior followed by DLVO theory, and is commonly found at the interfaces of aqueous solution and hydrophilic surfaces such as alumina or hydrophilic SAMs discussed in Chapters 3-5. Though it is easily supposed that structure of the aqueous interface is determined by various complicated factors, the domains covered on the native TiO_2 surface as appeared in Fig. 6.3 seemed to be a critical role also in the background term. Identifying the chemical composition of the domains is, here describes again, a key to understand the mechanism of the hydrophilic transition of the surface.

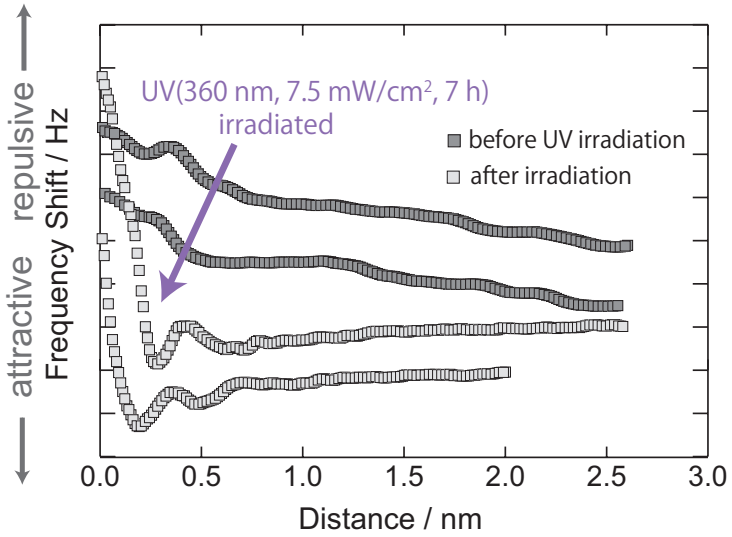

Figure 6.7. *Δf*-distance curves over rutile-TiO_2 in KCl aqueous solution of 1 M before (black) and after (gray) UV irradiation. Oscillation Amplitude: 0.2 nm

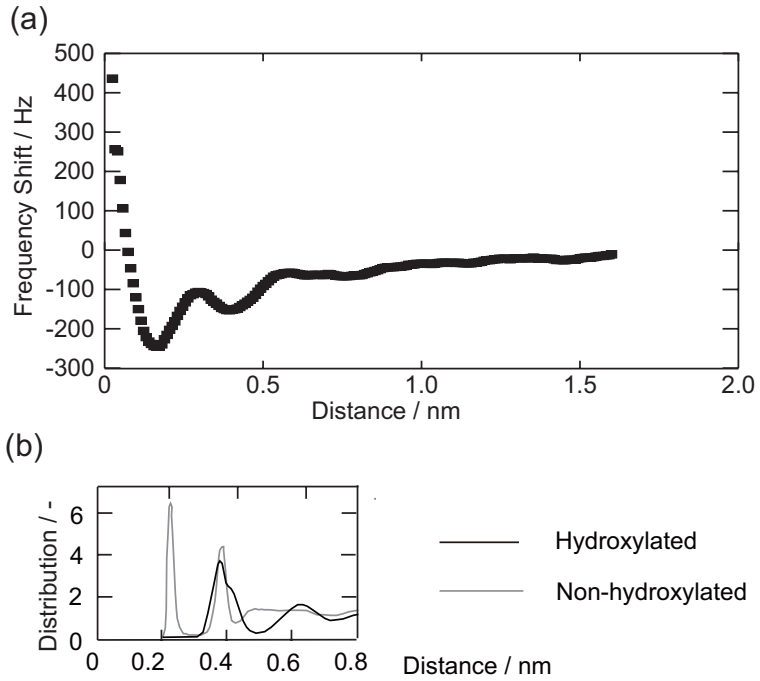

Figure 6.8. (a) The *Δf*-distance curve after UV irradiation of Fig. 6.7 to aid for comparision. (b) Normalized density distribution functions on hydroxylated and non-hydroxylated rutile-TiO_2(110) obtained by the MD simulation study of ref. 9.

6.6 Conclusions

In this chapter, metal oxide surfaces, such as mica, Al_2O_3, TiO_2, were immersed in a KCl solution, and observed with state-of-the-art FM-AFM.

In the cross-sectional Δf distributions, site-specific modulations due to the interfacial water layers were found on most hydrophilic mica, whereas the modulations were less observed on Al_2O_3, and TiO_2 surface, exhibited less hydrophilic. These results suggested that the even atomic scale roughness is contributed to the stability of the adsorbed water layer; solvent water molecules are expected to be easy to access to the flat mica surface, whereas to be restricted to access to the hydrophilic end-groups on atomically hubbly Al_2O_3, or TiO_2 surface. This is beyond the scope of the conventional approaches to analyze wettability. The author considers that these different organized water layers relate to different hydrophilic character of the metal oxide surfaces, which suggests that the importance of considering the nanostructure in the wettability analysis.

The tendency that well organized water layer exists on the hydrophilic surface was found on the TiO_2 interface where the wettability is transmuted by UV irradiation. In addition, the author found another contribution of the wettablity on TiO_2 surface: the aggregated domains whose height is uniform at 2 nm. Considered the time-lapse images at the TiO_2 interface, the author envisages that the domains should be originated from precipitation of the ionic solute or organic contaminants. Identifying the chemical composition of the domains is just as a key to understand the whole mechanism of the hydrophilic transition of the surface, which is important issue for future studies.

References in Chapter 6

[1] P. A. Thiel, and T. E. Madey, *Surf. Sci. Rep.* 7 (1987) 211.

[2] M. A. Henderson, *Surf. Sci. Rep.* 46 (2002) 1.

[3] K. Honda and A. Fujishima, *Nature* 238 (1972) 37.

[4] R. Wang, K.Hashimoto, A. Fujishima, M. Chikuni, E. Kojima, A. Kitamura, M. Shimohigoshi, and T. Watanabe, *Nature* 388 (1997) 431.

[5] T. Watanabe, A. Nakajima, R. Wang, M. Minabe, S. Koizumi, A. Fujishima, and K. Hashimoto, *Thin Solid Films* 351 (1999) 260.

[6] N. Sakai, A. Fujishima, T. Watanabe, and K. Hashimoto, *J. Phys. Chem. B* 105 (2001) 3023.

[7] R. N. Wenzel, *J. Phys. Colloid Chem.* 53 (1949) 1466.

[8] A. B. D. Cassie, *Discuss Faraday Soc.* 3 (1948) 11.

[9] J. G. Catalano, C. Park, Z. Zhang, and P. Fenter, *Langmuir* 22 (2006) 4668.

[10] M. Předota, A. V. Bandura, P. T. Cummings, J. D. Kubicki, D. J. Wesolowski, A. A. Chialvo, and M. L. Machesky, *J. Phys. Chem. B* 108 (2004) 12049.

[11] U. Diebold, *Surf. Sci. Rep.* 48 (2003) 53.

[12] H. Y. Chen, O. Zahraa, M. Bouchy, F. Thomas, and J. Y. Bottero, *J. Photochem. Photobiol. A* 85 (1995) 179.

[13] Y. Gan and G. V. Franks *J. Phys. Chem. B*, *109* (2005) 12474.

[14] K. Suzuki, N. Oyabu, K. Kobayashi, K. Matsushige, and H. Yamada, *Appl. Phys. Express* 4 (2011) 125102.

[15] J. N. Israelachivili, *Intermolecular and Surface Forces 3rd Ed.*, Academic Press,

London, 2010.

[16] G. B. Kaggwa, P. C. Nalam, J. I. Kilpatrick, N. D. Spencer, and S. P. Jarvis, *Langmuir* 28 (2012) 6589.

[17] S. Marčelja, *Nature* 241 (1973) 451.

[18] B. Jönsson and H. Wennerström, *J. Chem. Soc. Faraday Trans.* 79 (1983) 19.

[19] D. Schiby and E. Ruckenstein, *Chem. Phys. Lett.* 95 (1983) 435.

[20] A. Luzar, D. Bratko, and L. Blum, *J. Chem. Phys.* 86 (1987) 2955.

[21] P. Attard and M. T. Batchelor, *Chem. Phys. Lett.* 149 (1988) 206.

[22] A. Delville, *J. Phys. Chem.* 97 (1993) 9703.

[23] S. Marčelja, *Colloid Surf. A* 130 (1997) 321.

[24] R. G. Horn, D. T. Smith and W. Haller, *Chem. Phys. Lett.* 162 (1989) 404.

[25] W. A. Ducker, T. J. Senden, and R. M. Pashley, *Langmuir* 8 (1992) 1831.

Chapter 7: FM-AFM Application for Practical Polymer Surface

7.1 Introduction

In this chapter, in order to demonstrate and discuss an ability and application of state-of-the-art FM-AFM, the surface of a synthetic polymer was investigated as another example of practical interface. Its surface facing organic solvents is an important interface in industrial applications and manufacturing processes. Most polymers contain crystallized and amorphous domains to be heterogeneous. The stability and chemical resistibility, that is significantly affected by manufacturing processes such as solvent cast or extrusion, is related to the shape of domains and domain boundaries, as well as intra-domain structures. Physical and chemical properties of polymer products are also sensitive to the structure of their surface facing environments. It is thus demanded to observe the topography of synthetic polymers immersed in organic solvents with a single-nanometer or subnanometer resolution. Such information provides helpful suggestion to improve its functionality in practical usage.

In this study, surface of a commercial polyethylene film was observed in dodecane. In order to acheive subnanometer spatial resolution, extremely clean and flat surface of the film was prepared with originally developed procedure.

7.2 Experiment

A mica wafer was heated in air at 600 K, on which a commercial polyethylene film (Mitsui Chemicals Fabro, Inc.) was put and cooling down to room temperature in seconds. The film was securely fixed on the wafer and present a flat surface.

Here the author chose *n*-dodecane (>99%, Wako) as the imaging liquid. This liquid alkane presents a low vapor pressure at room temperature. Since the liquid droplet on the mount was open to the environment, evaporation of the imaging liquid limited the time to spend to stabilize the microscope with an object interface installed. The low rate

of evaporation allowed a long time for stabilization to reduce the thermally induced drift of the tip in the order of 0.1 nm per min relative to the object film.

7.3 Topography of polyethylene film

Figure 7.1 presents constant frequency-shift topography of the polyethylene film observed in dodecane. Vertical tip position was feedback-regulated to keep the frequency shift (Δf) constant at +300 Hz. In the wide-area image of (a), linear ridges of 20 nm width and 1 μm length are laid in one direction. These ridges are possibly related to nanofibrils found in previous AFM studies [1,2]. Polymer films contain micrometer-scale fibrils composed of nanofibrils, especially when manufactured by extrusion [2]. It is reasonable to assume that the commercial film studied here was manufactured by tubular film extrusion. On some ridges, grooves appeared in the perpendicular direction to the ridge axis. When grooves appeared with similar intervals on a ridge, the ridge with the periodic grooves looked like a helix as shown in the zoomed-in image of (b). The subnanometer topography of individual ridges was further examined. The protrusion of the ridge bodies was much larger than corrugations to be imaged. Here the feedback gain was reduced for Δf regulation and then monitored the error signal of the Δf from the set point, +300 Hz. The positive Δf set point brought the tip close to the surface, where a repulsive force was present between the tip and surface. This is a useful scheme to observe small corrugations embedded in a rough surface, even though the absolute topographic height remains unknown. The weak feedback allowed the tip to trace the envelope of the ridge without severe contact. The tip-surface distance was uneven over subnanometer corrugations, which generated Δf error from the setpoint. Panel (a) of Fig. 7.2 shows the lateral distribution of Δf error thereby obtained.

Panel (b) presents the lateral distribution of the static vertical cantilever deflection, which was simultaneously recorded with the Δf error of panel (a). No discriminative signal appeared in the static deflection. To be quantitative, a cross section of the deflection was made along the line in (b) and shown in panel (c). The static deflection fluctuated by ±10 pm around zero. These results indicated that tip traced the surface

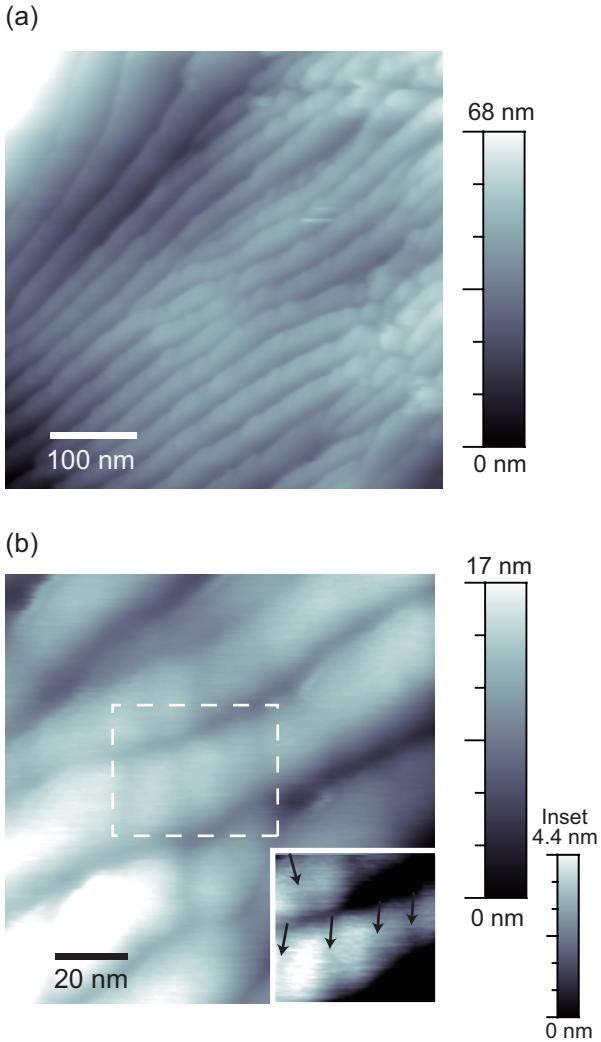

Figure 7.1. Constant frequency-shift topography of the polyethylene film immersed in *n*-dodecane. Image size: (a) 510 nm square and (b) 110 nm square. The inset shows the center of image (b) with an enhanced contrast. Arrows in the inset indicate grooves perpendicular to the ridge axis. Δf: +300 Hz. Oscillation amplitude: 0.2 nm.

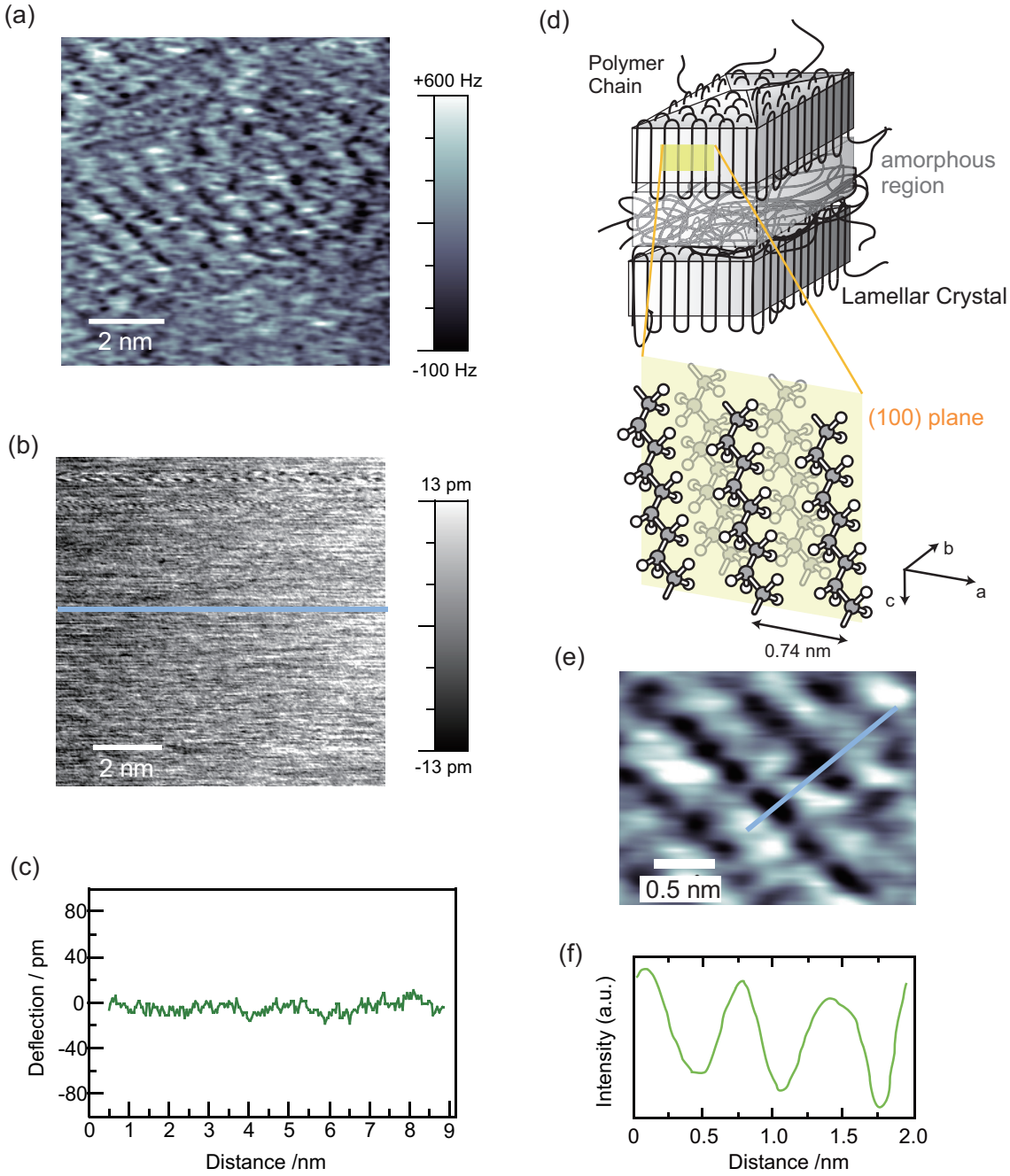

Figure 7.2. Subnanometer topography of the polyethylene film immersed in n-dodecane. The lateral distribution of Δf error is shown in (a). Setpoint of Δf feedback: +300 Hz. Oscillation amplitude: 0.1 nm. The simultaneously observed static deflection of the cantilever is in (b). The cross section determined on the line is presented in (c). Partially crystalline polyethylene is illustrated in (d). The ordered region of (a) was digitally zoomed up and shown in (e). The cross section determined on the line is in (f).

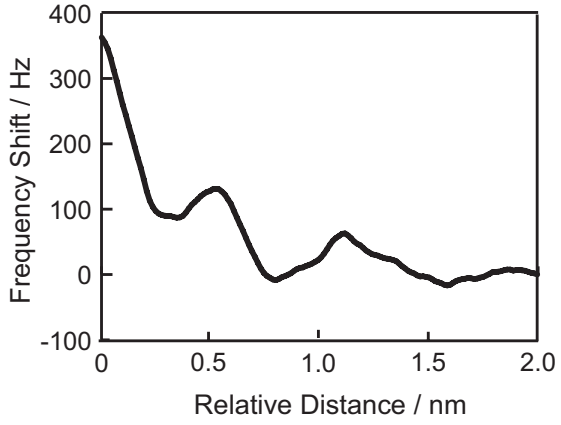

Figure 7.3. A Δf-distance curve at the dodecane-polyethylene interface.

envelope without severe contacts to the film surface. The Δf-distance curve over the dodecane-polyethylene interface is another evidence of the non-contact operation. A representative result is presented in Fig. 7.3. The frequency shift was locally modulated at distances of 1.1 and 0.5 nm. The local modulations represented dodecane liquid structured on the film surface. By reducing the distance less than 0.5 nm, Δf increased monotonically with the tip approaching the surface. The monotonic increase of Δf was assigned to the repulsion of the tip and surface, partially contact with each other. Based on this assignment, the author assumes that the first and second layer of structured dodecane presented the local Δf modulation at 0.5 nm and 1.1 nm, respectively. The Δf set point was +300 Hz in the imaging scans, which was sufficiently large relative to the amplitude of the local Δf modulation. The Δf-distance curve showed that the tip regulated at Δf = +300 Hz was present at a distance close by 0.4 nm relative to the position of the first Δf maximum of the dodecane layer. Hence the author believe the absence of dodecane between the tip and surface. According to the conversion formulated by Sader and Jarvis [3] the strength of the repulsive tip-surface force used in the imaging scan of Fig. 7.2 was estimated to be 0.1 nN. This number is much smaller than the strength of the force loaded in contact-mode AFM operations, in the order of nN.

The curve in Fig. 7.3 showed positive Δf throughout the distances examined. This suggests repulsive tip-surface force at any distances. The apparent absence of the attractive van der Waals tip-surface force should be rationalized. Electrostatic repulsion between localized charge on the tip and surface possibly engaged in the monotonous repulsive force, because the polyethylene object and the imaging liquid were complete insulators. A long-range repulsive force appears and overrides the van der Waals contribution. The nonpolar property of dodecane and the absence of electrolytes lead to inefficient screening of the electric field assumed in this scheme.

Locally ordered structures assignable to a lamella appeared in the middle of the Δf error image of Fig. 7.2(a). The size of that lamella was less than 10 nm, which was also smaller than the typical size of lamella. Smaller lamella suggested that the alkyl chain folded with frequent turns in this film. A possible origin of the small lamella is the intrinsic property of the film. The extent of structure heterogeneity of the film should depend on the molecular weight distribution and manufacture history. The cycle of heating and cooling given in mounting the film may have caused an extrinsic modification. The disordered domain surrounding the lamella was not crystallized. The illustration in panel (d) of Fig. 7.2 shows embedded lamellae.

Panel (e) shows a narrow-area Δf error image of the lamella. Five parallel rows were identified and the row-to-row distance was 0.70-0.75 nm as show in the profile (f). A contact-mode AFM study in air [4] found parallel rows on (110) facets of pyramidal polyethylene crystals and assigned them to individual alkyl chains. The observed row-to-row distance in that crystal was 0.89 nm consistent to the crystallographic structure determined by X-ray diffraction [5]. The row-to-row distance found in Fig. 7.2 was smaller than that of the (110) facet and acceptable for a (100) facet, on which row-to-row distance should be 0.74 nm [5]. The author thus assign the ordered domain in Fig. 3(e) to a (100)-truncated lamella. The packing of polyethylene chains has been visualized using FM-AFM. Some intra-row structures were also seen in the image.

7.4 Conclusion

Using a low-noise FM-AFM, the topography of a partially crystalline polyethylene film was successfully observed in dodecane with original sample preparation procedure. Locally ordered, parallel molecular chains were found and assigned to a (100) facet of a lamella embedded in amorphous bodies. This result showed that a promising ability of FM-AFM to observe subnanometer topography of practical soft materials as well as well-prepared surfaces such as the flat crystalline surfaces or the self-assembled monolayers.

References in Chapter 7

[1] S. N. Magonov, S. S. Sheiko, R. A. C. Deblieck and M. Moller, *Macromolecules* 26 (1993) 1380.

[2] K. M. Drummond, R. A. Shanks and F. Cser, *J. Appl. Polymer Sci.* 83 **(**2002) 777.

[3] J. E. Sader and S. P. Jarvis, *Appl. Phys. Lett.* 84 (2004) 1801.

[4] R. Patil and D. H. Reneker, *Polymer* 35 (1994) 1909.

[5] A. Müller, *Roy. Soc. Proc., A* 120 (1928) 437.

Chapter 8: Summary and Future Prospects

Throughout this study, the possibilities of FM-AFM applications to the investigation on the atomic-scale structure at solid-liquid interfaces were demonstrated. The conclusions obtained in this study, as well as suggestions for the future studies are summarized here.

The purpose and background of this study are summarized in Chapter 1. The principle, instrument and historical reviews of FM-AFM are described in Chapter 2.

A promising ability of FM-AFM to probe the local structure of interfacial liquids is discussed in Chapter 3. The observed force-distance curve contained local force oscillations accompanied with exponentially decayed, electric double layer force. The local force oscillations observed on α-Al_2O_3(01-12) and TiO_2(110) surface, are comparable to theoretical or another experimental results of water structure at the *open* interfaces. This is the experimental evidence that the tip apex is possible to probe water-induced force modulations, to detect the local structure of interfacial liquids.

In addition, the role of tip apex was experimentally demonstrated at hexadecane-thiol SAM and water-mica interfaces using sharpened and cone-shaped tips. The topography of these surfaces was acquired with subnanometer resolution regardless of the nominal radius of the tips. The amplitude and layer-to-layer distances of force modulations due to the interfacial hexadecane were also totally insensitive to the nominal tip radius. Insensitive topographies and force-distance curves revealed that a minitip which is quite smaller than the nominal radius, 10 nm in this study, is present on the tip body and functions as a force probe. Dominant role of the tip apex enables to probe the local structure of interfacial liquid in both lateral and vertical coordination in subnanometer scale. The presented experimental results convince us that AFM tip apex is possible to extract enhancement and depression of the liquid density in the *relative* scale. Determining the *absolute* value of the density distribution from the force distribution is very challenging issue. Based on the presented findings, collaborations of theoretical studies will be required in future to complete the quantitative relationships,

including quantitative estimation of contribution of an actual tip and real potential for the applied force, as mentioned in the last paragraph.

In Chapters 4 and 5, the author discussed the interfacial structures of various liquids facing different surface functional groups, and the dominant factor of structuring at the interface extracted from comparison of the interfacial structures. Employing such ability of the highly sensitive FM-AFM, interfacial liquid structure of water, alcohols, and hydrocarbons, over well-defined CH_3-, OH-, and COOH-terminated SAMs and alcohol adsorbates on HOPG.

At inert interfaces of liquid hydrocarbons over a CH_3-terminated SAM, the steric configuration of liquid molecule dominantly affects the interfacial structure. The density distribution of the hydrocarbons was even along lateral coordinates over the CH_3-terminated SAM though uneven density distribution was observed along the vertical coordinate. The even distribution of the alkanes was interpreted by the absence of any functional groups that produce specific chemical interactions with the CH_3 end-groups. The layer-to-layer separation of the force modulation was insensitive to the alkyl chain length, whereas phenyloctane exhibited a larger distance, affected by the bulky phenyl end-group.

On the other hand, the specific chemical interaction had a dominant contribution for structuring at polar interfaces. The water density was enhanced between two adjacent OH end-groups over mercaptoundecanol SAM, as opposed to on top of COOH and COO^- end-groups over mercaptoundecanoic acid SAM. The distribution was insensitive to the electrolyte composition of the aqueous solution. The results suggested the significant contribution of hydrogen bond for structuring of interfacial water. The different structures of interfacial water was due to different configurations of water coordinated sites to donate or accept hydrogen bonds.

Hydrogen bond had dominant contribution to structuring the primary liquid alcohols that presented the epitaxial structure over the COOH-terminated SAM surface as the water presented. Besides, steric environment of hydrogen bonding capable end-group affected the interfacial liquid structures. The tertiary alcohols presented laterally uniform cross-sectional distributions as the inert hydrocarbons did. This suggested that reduced accessibility of the bulky alcoholic OH to the surface COOH end-group made the hydrogen bond weak. Steric environment of hydrogen bonding

capable groups on liquid and solid was an important factor to build the lateral epitaxial structure at the interface.

The observed presence and absence of the epitaxial relationship were interpreted as the competition of two interactions; hydrogen bond and van der Waals interactions. The former interaction is site-specific to make a laterally heterogeneous structure of interfacial liquids, while the latter favors laterally uniform liquid layers. The competition of the two different interactions could be clearly observed at the interfacial structure of decanol over HOPG.

These results are significant experimental evidence which directly indicated the lateral structural relation between interfacial liquid and surface in subnanometer scale. The repeatable and physically interpretable distributions suggests that tip-probed force distribution was solely the consequence of the local structure of interfacial liquids on the solid substrate, including much less contribution of tip-induced effects. These indicate that qualitative difference in interfacial liquid structures is possible to be detected using AFM, which provides fruitful discussion of fundamental insights in interfacial chemistry.

In addition to the fundamental studies as mentioned in Chapters 3, 4 and 5, the analysis on interfacial liquid structure was applied for understanding the mechanism of practical phenomena or improvement of industrial processes. In Chapter 6, cross-sectional distributions to the metal oxide surfaces, such as mica, Al_2O_3, TiO_2, on which different wetting properties are exhibited for water, are compared to discuss the relationship between microscopic interfacial structure and wetting properties on the surface.

In the cross-sectional Δf distributions, site-specific modulations due to the interfacial water layers were found on most hydrophilic mica, whereas the modulations were less observed on less hydrophilic Al_2O_3, and TiO_2 surface. The author considers that the difference of organized water layers relates to different hydrophilic character of the metal oxide surfaces. Since the three metal oxide surfaces have quite similar chemical composition, the atomic-scale roughness was contributed to the stability of the adsorbed water layer. These results suggest that consideration of the atomic-scale surface structure is also essential in wettability analysis. This is an important start point for future considerations to complete the full picture of the interfaces and surface

wetting behavior. Quantification of intermolecular, and surface-liquid interaction contributed to structuring is an important issue, as well as quantifying the absolute density of water from the observed force distribution. This may make it possible to estimate the microscopic thermodynamic quantity such as contact angle or interfacial energy from the microscopic insight. Theory and additional analysis techniques following the current AFM study is required in future studies, and will support the current conclusion.

Another practical application of FM-AFM was demonstrated on a commercial polyethylene film in dodecane, discussed in Chapter 7. Locally ordered, parallel molecular chains were successfully observed and assigned to a (100) facet of a lamella embedded in amorphous bodies. This showed that a promising ability of FM-AFM to observe subnanometer topography of practical soft materials with an appropriate sample preparation, as well as well-prepared surfaces such as the flat crystalline surfaces or the self-assembled monolayers.

As summarized above, nanostructure of solid-liquid interfaces were successfully determined using the highly sensitive FM-AFM in this study. It is also evidenced that such FM-AFM could detect the qualitative difference of the interfacial structures which are modified by chemical nature of the molecules including steric environments of the chemical functional groups, especially with subnanometer spatial resolution. The results provide innovative and fundamental insights into the interfacial liquid structure, such as structural relation of interfacial liquids and surface, and contribution of intermolecular interaction for structuring. These will help to develop the intensive applications of new physical and chemical techniques to tailor the surface functions, and to direct control of the matter on molecular scale. The presented findings of the nanostructure of interfacial liquids have a great importance to a wide range of material sciences and provide remarkable guidelines for the future consideration of molecular interpretations of the complicated interfacial phenomena. The author envisages that the findings evolve interfacial chemistry leading to create many new materials and devices with a vast range of applications.

In order to further progress the FM-AFM analysis for *in-situ* structure at solid-liquid interface, quantifying the observed force comparable to other measurable physical quantities such as liquid density, surface charge density, and interfacial energy,

is an important but quite challenging issue. As demonstrated in this study, the observed force distribution was successfully explained with the approximation of minitip, and the qualitative difference of interfacial liquid structures was also isolated to provide significant insights of the liquid structuring. The experimental evidence of the dominant role of the tip apex leads to a better approximation to handle the contribution from an actual tip in interpreting the force. However small fluctuations of the tip apex still cannot be negligible in determining absolute value of the physical quantities accurately. Nevertheless, there still remains significant difficulty to determine the exact shape of the tip apex attributing to load the force, because it is too small to be observed experimentally and is easily changed during the measurements. Theoretical or other experimental techniques are strongly desired for the quantification to handle with uncertainty of the tip apex. A possible approach may be establishment of theory to extract the tip contribution from the force distribution or development of the tip whose structure and chemical composition is controlled. In future studies dealing with these challenging problems, the current experimental knowledge such as dominant roles of tip apex for force loading will be useful in building an initial model or approximation.

Acknowledgments

This dissertation would not have been possible without the guidance and the help of several individuals who in one way or another contributed and extended their valuable assistance in preparing and completing this study.

Foremost, the author would like to express utmost gratitude to Professor Dr. Hiroshi Onishi, Department of Chemistry, Kobe University, for his continuous guidance, kind encouragement, and fruitful discussions to accomplish this study.

The author is grateful to Associate Professor Dr. Kenjiro Kimura, Department of Chemistry, Kobe University, for his great assistance in the experiments and valuable advice throughout this work.

The author would like to thank Dr. Hirofumi Yamada, Dr. Kei Kobayashi, Dr. Noriaki Oyabu, Mr. Ryohei Kokawa, Dr. Kazuyuki Watanabe, and Dr. Masahiro Ohta, for their kind assistance and technical support on state-of-the-art FM-AFM system used in this study.

The author would like to thank Dr. Takashi Ichii for his advice on the preparation of thiolate monolayer.

The author gratefully appreciates kind help by all my colleagues and staffs in Onishi group and Kimura group, Kobe University.

The author would like to acknowledge the financial support of the Japan Society for the Promotion of Science, Research Fellowship for Young Scientist.

Lastly, the author expresses special thanks to all of those who supported in any respect during the completion of this work.

List of Publications

1. Takumi Hiasa, Kenjiro Kimura, Hiroshi Onishi, Masahiro Ohta, Kazuyuki Watanabe, Ryohei Kokawa, Noriaki Oyabu, Kei Kobayashi, Hirofumi Yamada.
   "Solution-TiO_2 Interface Probed by Frequency-Modulation Atomic Force Microscopy"
   Japanese Journal of Applied Physics, 48 (2009) 08JB19.

2. Takumi Hiasa, Kenjiro Kimura, Hiroshi Onishi, Masahiro Ohta, Kazuyuki Watanabe, Ryohei Kokawa, Noriaki Oyabu, Kei Kobayashi, Hirofumi Yamada.
   "Aqueous Solution Structure over α-Al_2O_3(01-12) Probed by Frequency-Modulation Atomic Force Microscopy"
   Journal of Physical Chemistry C, 114 (2010) 21423.

3. Takumi Hiasa, Kenjiro Kimura, Hiroshi Onishi.
   "Two-dimensional distribution of liquid hydrocarbons facing alkanethiol monolayers visualized by frequency modulation atomic force microscopy"
   Colloids and Surfaces A: Physicochemical and Engineering Aspects, 396 (2012) 203.

4. Takumi Hiasa, Tomoki Sugihara, Kenjiro Kimura, Hiroshi Onishi.
   "FM-AFM imaging of a commercial polyethylene film immersed in *n*-dodecane"
   Journal of Physics; Condensed Matter, 24 (2012) 084011.

5. Takumi Hiasa, Kenjiro Kimura, Hiroshi Onishi.
   "Minitips in Frequency-Modulation Atomic Force Microscopy at Solid-Liquid Interface"
   Japanese Journal of Applied Physics, 51 (2012) 025703.

6. Takumi Hiasa, Kenjiro Kimura, Hiroshi Onishi.
"Hydration to hydrophilic thiolate monolayer visualized by atomic force microscopy"
Physical Chemistry Chemical Physics, 14 (2012) 8419.

7. Takumi Hiasa, Kenjiro Kimura, Hiroshi Onishi.
"Interfacial Structure of Primary and Tertiary Liquid Alcohols over Hydrophilic Thiolate Monolayers" (Submitted)